Physics of the Earth and Planetary Interiors, 79 (1993) 3–74
Elsevier Science Publishers B.V., Amsterdam

Travel-time tomography of the European–Mediterranean mantle down to 1400 km

Wim Spakman *[,a], Suzan van der Lee [a,b], Rob van der Hilst [a,c]

[a] *Department of Geophysics, Institute of Earth Sciences, Utrecht University, Budapestlaan 4, 3584 CD Utrecht, Netherlands*
[b] *Department of Geological and Geophysical Sciences, Guyot Hall, Princeton University, Princeton, NJ 08544-1003, USA*
[c] *Research School of Earth Sciences (ANU), GPO Box 4, Canberra A.C.T. 2601, Australia*

(Received 22 March 1993; accepted 15 April 1993)

ABSTRACT

The 3-D P-wave velocity structure of the mantle below Europe, the Mediterranean region and a part of Asia Minor is investigated. This study is a considerable extension of an earlier tomographic experiment that was limited to imaging upper-mantle structure only. Here, the Earth's volume under study encompasses the mantle to a depth of 1400 km, and we increase the number of International Seismological Centre (ISC) data for inversion by a factor of four by taking more years of observation, and by including data from teleseismic events. The most important departure from the earlier study is that we do not use the Jeffreys–Bullen model as a reference model, but an improved radially symmetric velocity model, the PM2 model, which is appropriate for the European–Mediterranean mantle.

Our inversion procedure consists of two steps. First, the radial model PM2 is determined from the ISC delay times by a nonlinear trial-and-error inversion of the data. As opposed to the Jeffreys–Bullen model, the new reference model has a high-velocity lithosphere, a low-velocity zone, and seismic discontinuities at depths of 400 and 670 km. Next, the ISC data are corrected for effects related to the change in reference model and inverted for 3-D heterogeneity relative to the PM2 model. We follow this two-step approach to attain a better linearizable tomographic problem in which ray paths computed in the PM2 model provide a better approximation of the actual ray paths than those computed from the Jeffreys–Bullen model. Hence, the two-step scheme leads to a more credible application of Fermat's Principle in linearizing the tomographic equations.

Inversion results for the 3-D heterogeneity are computed for both the uncorrected ISC data and for the PM2 data. The data fit obtained in the two-step approach is slightly better than in the inversion of ISC data (using the Jeffreys–Bullen reference model). A comparison of the tomographic results demonstrates that the PM2 data inversion is to be preferred. To assess the spatial resolution an analysis is given of hit count patterns (sampling of the mantle by ray paths) and results of sensitivity tests with 3-D synthetic velocity models. The spatial resolution obtained varies with position in the mantle and is studied both in map view and in cross-section. In the well-sampled regions of the mantle the spatial resolution for larger-scale structure can (qualitatively) be denoted as reasonable to good, and at least sufficient to allow interpretation of larger-scale anomalies.

A comparison is made of the results of this study with independent models of S-velocity heterogeneity obtained in a number of investigations, and with a prediction of the seismic velocity structure of the mantle computed from tectonic reconstructions of the Mediterranean region. In the context of this comparison, interpretations of large-scale positive anomalies found in the Mediterranean upper mantle in terms of subducted lithosphere are given. Specifically addressed are subduction below southern Spain, below the Western Mediterranean and Italy, and below the Aegean. In the last region a slab anomaly is mapped down to depths of 800 km.

1. Introduction

Our purpose of this paper is to present new results on the structure of the lithosphere and mantle below Europe, the Mediterranean and a part of Asia Minor. This investigation is a considerable extension of that by Spakman (1988, 1991). Some characteristics of the scope of this earlier study are as follows:

(1) the Earth's volume for mapping was the

* Corresponding author.

upper mantle below Europe, the Mediterranean and Asia Minor.

(2) About 500 000 delay times from 18 years of observation (1964–1982) were used. Most of the data originated from regional earthquake–station combinations. No data from teleseismic events were used.

(3) The reference model employed for calculating ray path geometries and linearization of the model equation was the Jeffreys–Bullen (JB) P-wave velocity model (e.g. Jeffreys, 1970).

The following considerations motivated the present study, in which we basically want to focus on a larger mantle volume, increase the number of data for inversion and depart from the use of the JB model as a reference model.

First, there is a potential problem with using the JB reference model. Spakman (1988, 1991) argued that this model is not the most appropriate model to use as a reference for the 3-D imaging of the European mantle. The ISC delay-time data display clear variation as a function of epicentral distance, indicating that the average P-wave velocity as a function of depth departs systematically from the JB model. These differences were reflected in the 3-D results obtained:

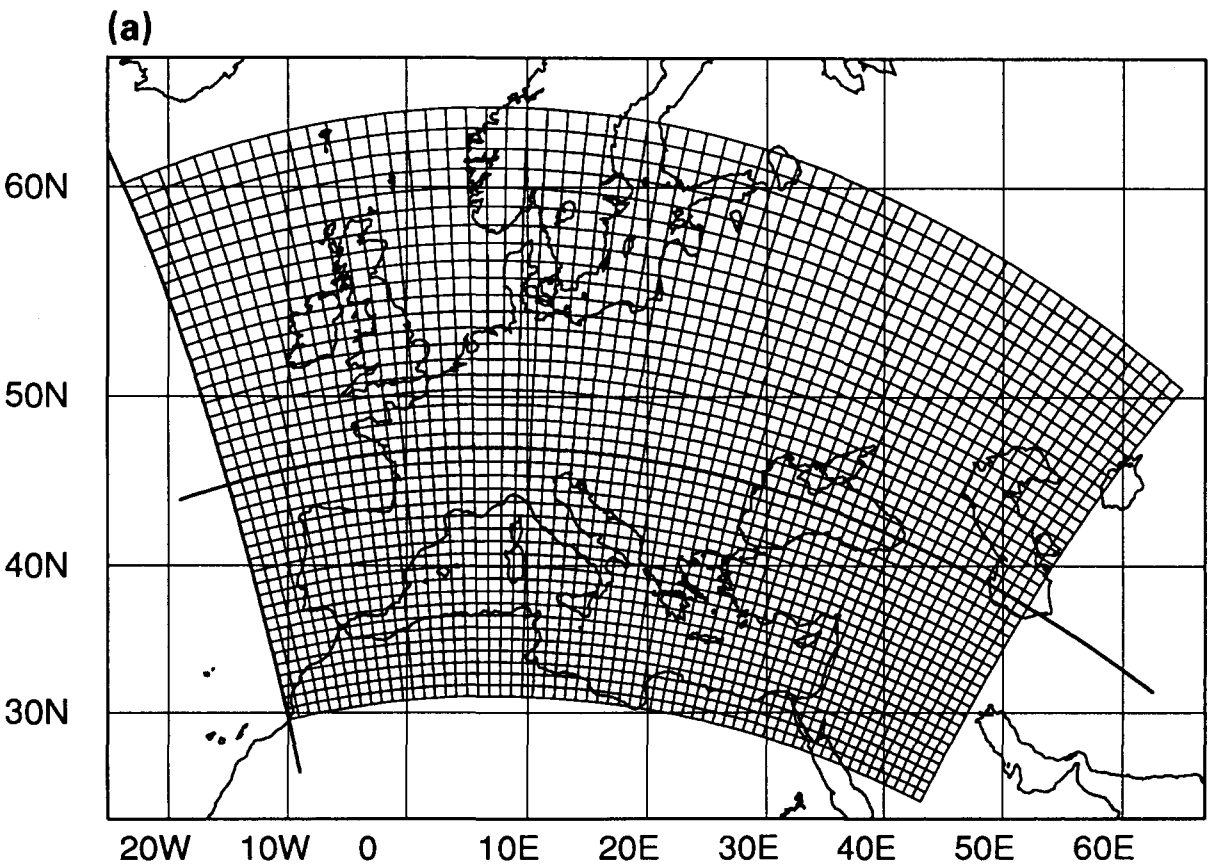

Fig. 1. (a) The European–Mediterranean region (normal Mercator projection). The grid denotes the cell division of area below which the mantle is investigated. The two heavy lines represent the rotated coordinate axis in which the cell model is defined. The new longitude axis is defined as the great circle with azimuth 74° and running through 45°N, 16°W, i.e. the point at which the axes intersect. (b) Mantle volume investigated and cell division. The rotated frame is specifically taken to give cells with nearly the same lateral dimensions in kilometers. In degrees the cell size is 0.8°. The span of the cell model is 62 cells in longitude, 40 cells in latitude and 20 cells in depth. Cell thickness increases with depth from 33 km at the surface to 100 km at 1400 km (see also Table 1). Approximate dimensions of the model: 5500 km × 3500 km × 1400 km.

on average, higher velocities were found in the lithosphere, a low-velocity zone was imaged, and directly above 670 km depth primarily low-velocity heterogeneity was imaged, reflecting the presence of the 670 km discontinuity. The JB model is smooth and velocities increase monotonically with depth, and thus the model lacks all of the features noted above. Van der Hilst and Spakman (1989) and Zielhuis et al. (1989) demonstrated that the difference between the JB model and the laterally averaged Earth structure below a particular geographical region may give rise to large deviations of JB rays from actual rays sharing the same end-points. This is specifically important for tomographic studies in which rays bottoming in the first 1000 km of the mantle are used. Travel-time tomography is based on the assumption that reference rays are a good approximation of actual rays. Van der Hilst and Spakman (1989) proposed to invert first the delay-time data for an improved (regional) reference model and to invert next the reference model corrected data for 3-D heterogeneity. Van der Hilst (1990) applied this two-step inversion scheme successfully to map mantle structure below Central America and the Caribbean region. In the present study we will use the reference model correction technique to image the European mantle.

Second, we can improve on the earlier study by using many more data, not only because we have 5.5 years more of observation (until mid-1987), but also by including arrivals from teleseismic events in regional (i.e. European–Mediterranean) stations. Third, we decided to investigate a larger mantle volume down to 1400 km. The reason for this choice is that, in the earlier re-

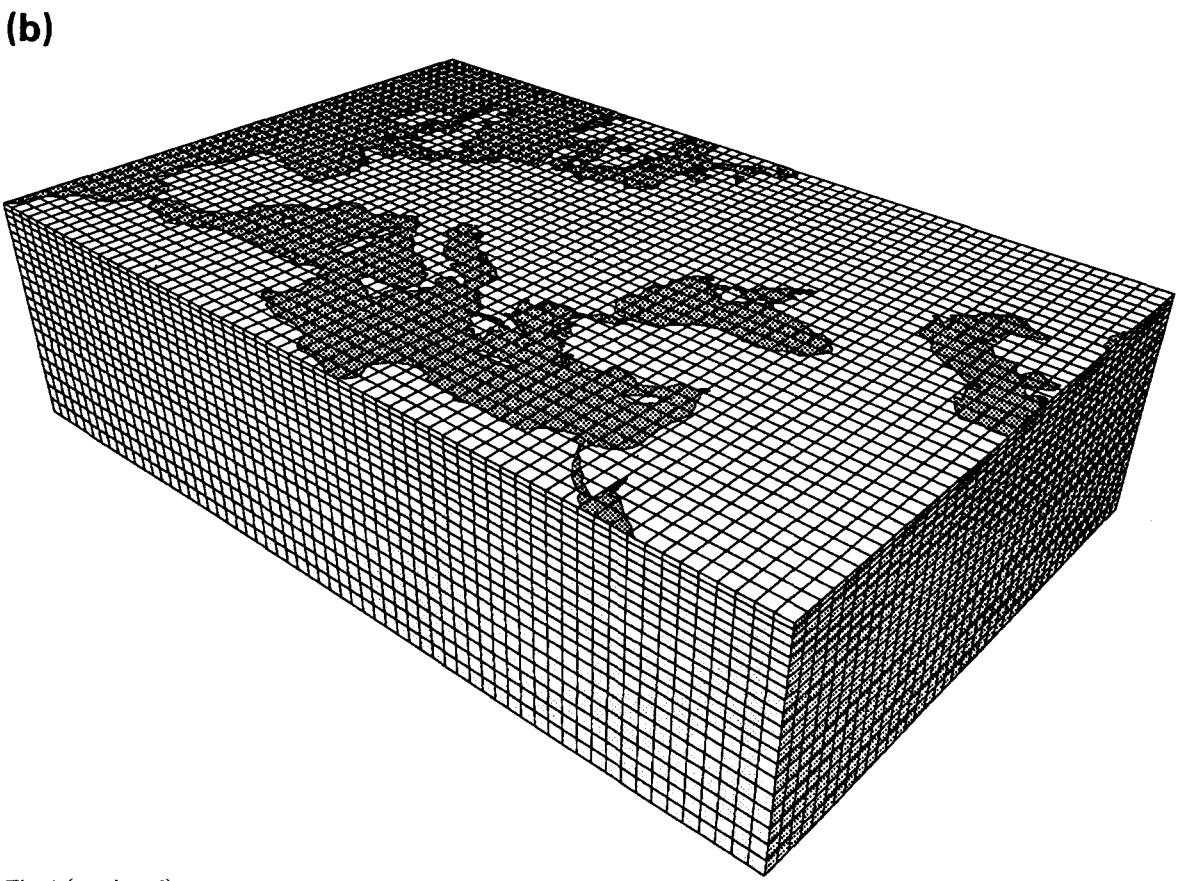

Fig. 1 (continued).

sults, anomalies associated with slab subduction (for instance, in the Aegean region (Spakman et al., 1988)) have significant amplitudes even in the lowermost layers of the upper-mantle model used. Therefore, our present interest is also to investigate whether heterogeneities in the lower mantle below the region could have contributed to anomalies mapped in the upper mantle.

In summary, we want to improve on the earlier results by tackling nonlinear effects associated with an inadequate reference model, use many more data (specifically from teleseismic events), and extend the target volume for imaging to include part of the lower mantle. With these improvements we hope, of course, to obtain more reliable images of the 3-D structure suitable for interpretation in a geodynamical context.

2. Data selection

P delay-time data are selected for the imaging of mantle structure below the region depicted in Fig. 1. Using the following selection criteria, the International Seismological Centre (ISC) Bulletin tapes for the period January 1964–July 1987 are scanned for delays and event locations: (1) absolute delay time less than 10 s (before inversion this limit is made smaller); (2) epicentral distance less than 90° to avoid the influence of the D″ layer; (3) earthquakes with epicenters between 10°W and 75°E, and 10°S and 75°N must be reported by at least 10 stations, to ensure some accuracy of the event location; (4) events located outside this region must be recorded by at least 50 stations globally and have magnitudes larger

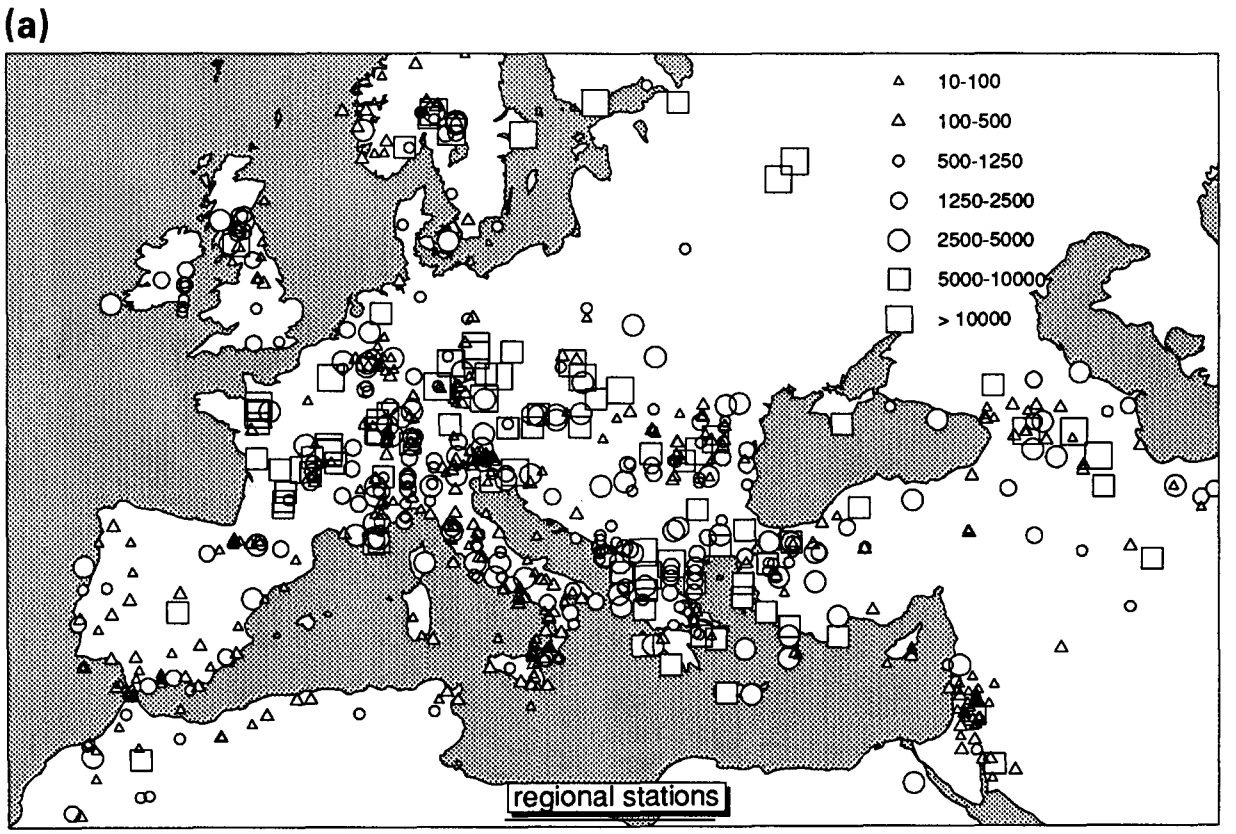

Fig. 2. Stations and earthquakes used. (a) Stations in study region (1456), i.e. located on top of the cell model. Symbols (and size) denote the number of observations (see key). (b) Stations globally (2259) within 90° from events in study region. (c) Events in study region with magnitude zero or larger and at least 10 observations. (d) Global distribution of events that are within at most 90° from a regional station. Magnitude greater than 4.5, number of observations greater than 50.

than 4.5; (5) either the recording station or the earthquake, or both, are located in the region displayed in Fig. 1. This selection yielded nearly 1.7 million data associated with about 60 000 events and 2259 stations. Figures 2(a–d) display the earthquake epicenter and station locations. Within the region studied, most of the stations and epicenters selected are located in central and SE Europe. On a global scale, large gaps in station coverage exist. However, most of the earthquakes within Europe are still recorded at distant stations found in three distinct directions: E–ENE, W–WNW and S. The locations of teleseismic events are predominated by earthquakes

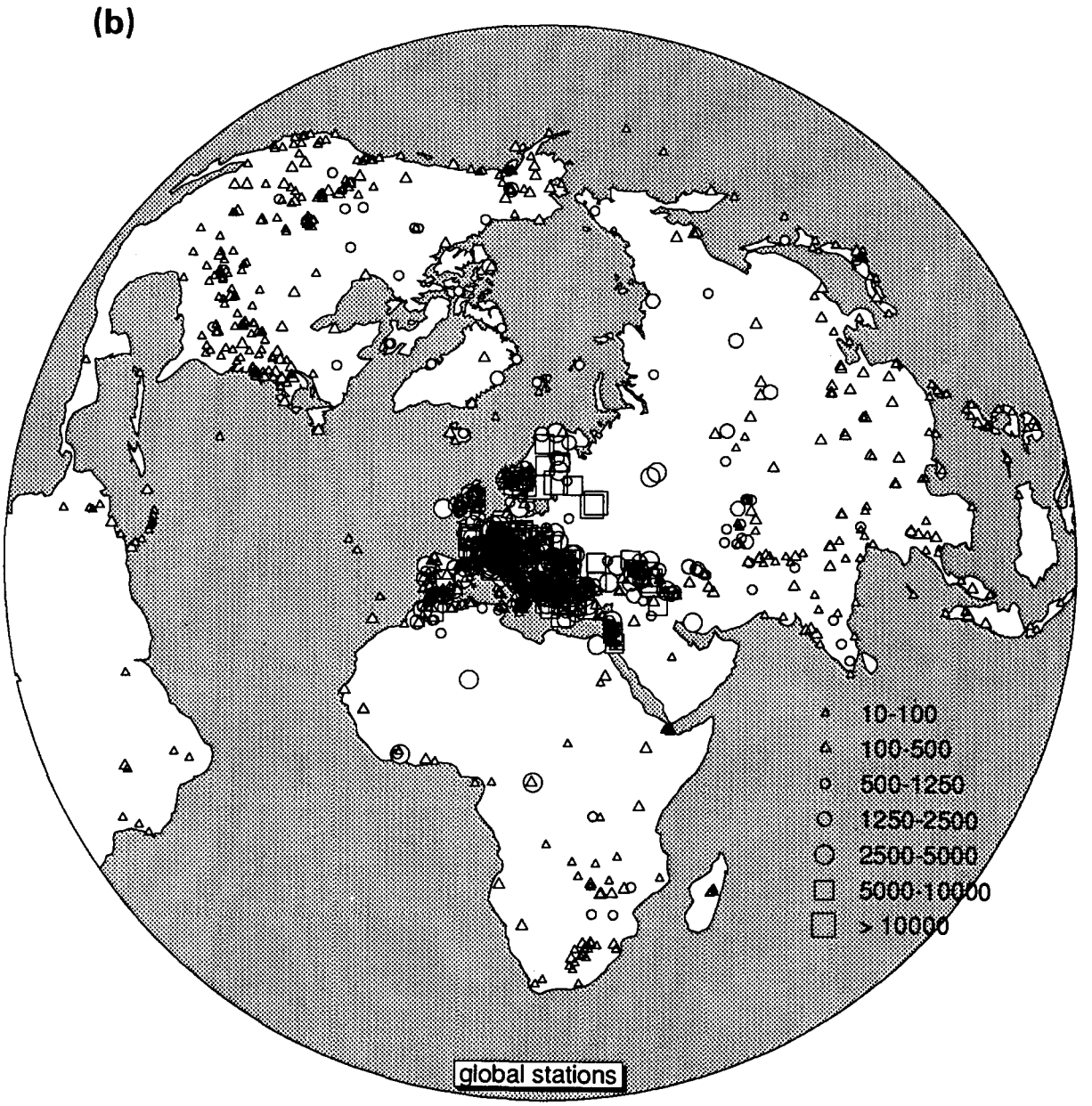

Fig. 2 (continued).

in the Circumpacific seismic belt and earthquakes in SE Asia. The restricted spread in incident angle for ray paths emerging below Europe and the Mediterranean is counterbalanced by a large variation in ray azimuth.

The distribution of the 1.7 million data as a function of delay-time value is given in Fig. 3. Three Gaussian curves with increasing standard deviation are displayed to illustrate the well-known fact that delay times are not distributed according to a Gaussian probability density function. The asymmetry of the distribution can partly be explained by reference model influences combined with misidentification of later arrivals as P arrivals between 15° and 25° (see section 4).

It is more instructive to investigate the variation of delay times with epicentral distance by means of a density plot (Fig. 4). The density plot is a 2-D histogram constructed by counting the number of delays in $0.1'' \times 0.5°$ intervals. The dashed line of zero delay corresponds to the JB travel-time prediction. Any departure from this line is caused by data errors, velocity heterogeneity relative to the JB model, effects of source mislocation and station statics. Of particular interest are the smooth trends as a function of epicentral distance. These trends can hardly be attributed to 3-D heterogeneity alone, but can be explained by variations in the 1-D velocity relative to the JB model (Van der Hilst and Spakman, 1989; Zielhuis et al., 1989). The data at short epicentral distance belong to regional source–event combinations and associated ray paths that bottom in the lithosphere and upper mantle (see Fig. 9 below). As the distance increases, the delays originate either from regional events observed at stations at teleseismic distances or teleseismic events recorded at regional

(c)

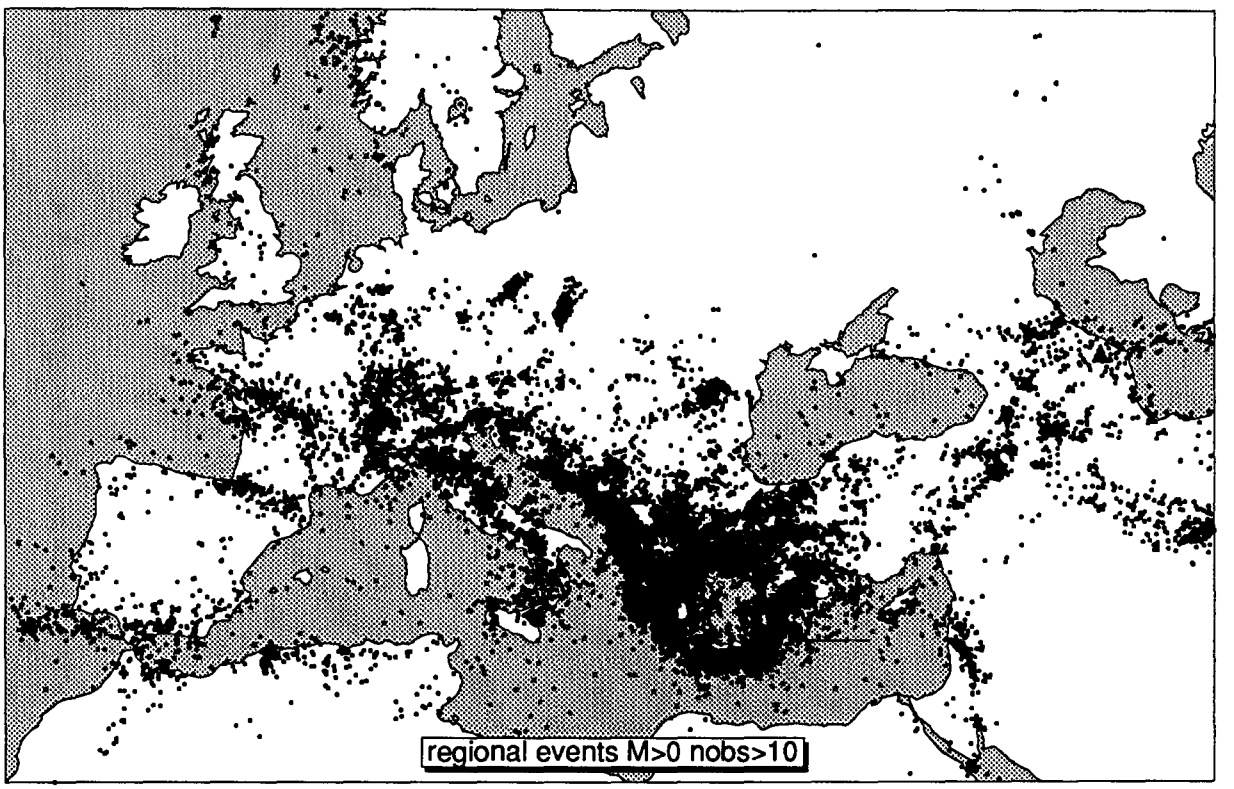

Fig. 2 (continued).

stations, and the associated rays bottom in the lower mantle. Hence, the delays at shorter distances give information on the regional mantle structure only, whereas the data for larger distances contain information on both the upper mantle and the lower mantle.

The white circles in Fig. 4 denote travel-time delays with respect to JB travel times (line of zero delay) of a source located at 33 km in our improved reference model (derived in section 4). Specifically, these reference model delays (depending on source depth) are used to correct the ISC data for a change in reference model from the JB model to the improved model. In the

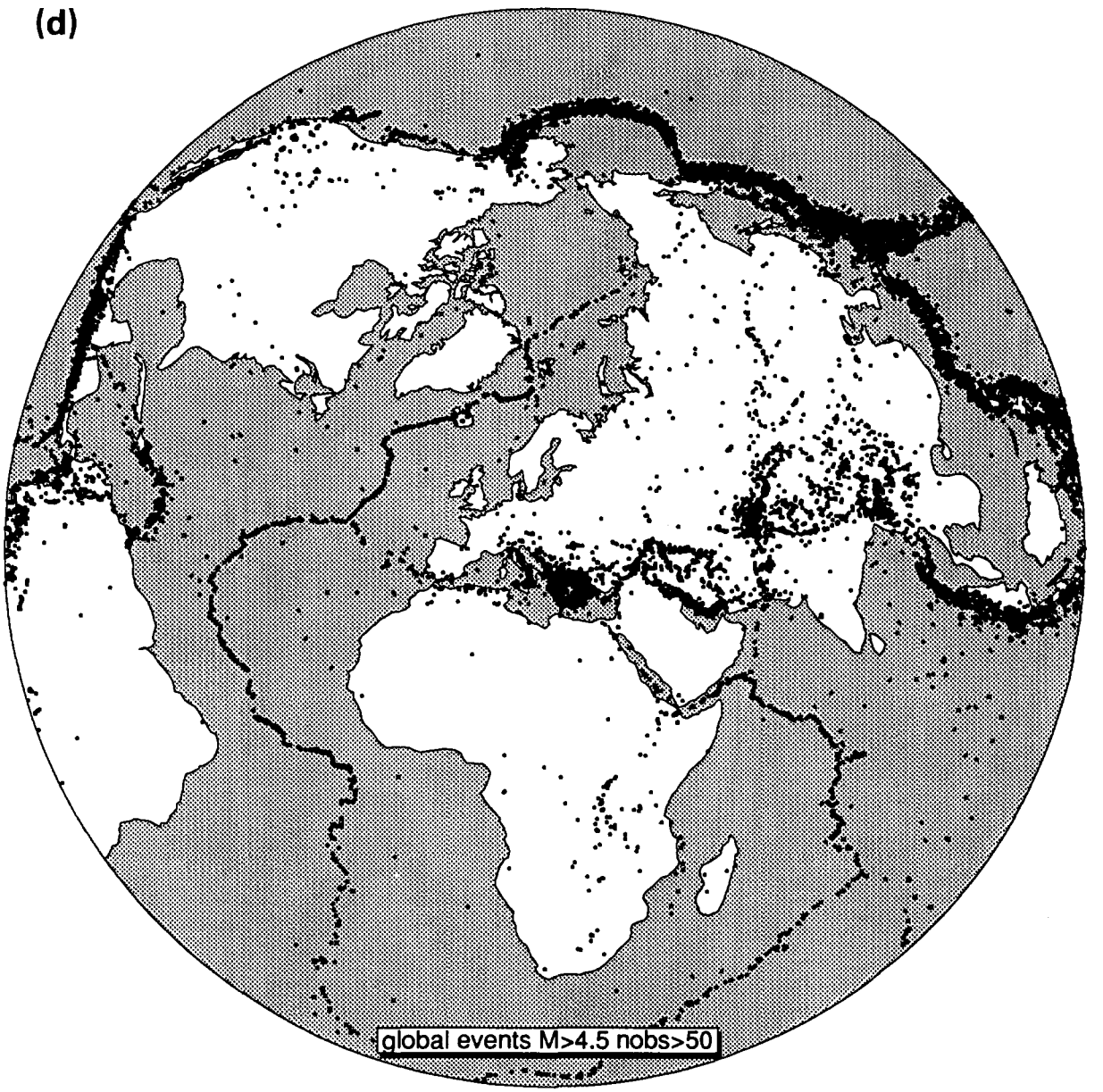

Fig. 2 (continued).

inversion we will only allow delays between −3 and +3 s to avoid a strong influence of outlying data on the solution of the inverse problem. Now that we have described some bulk features of the 1.7 million data let us focus on the interpretation of delay times.

3. Tomographic method

Our method for the interpretation of delay times essentially consists of two steps. First, we determine an improved reference model from the (ISC) data by nonlinear inversion; this will be discussed in section 4. Next, we use the reference model corrected data to solve for the P-wave velocity heterogeneity and for event- and station-related parameters. Details of the theory of the reference model adjustment have been given by Van der Hilst and Spakman (1989) and Van der Hilst (1990). For details of the theory of linearized travel-time tomography and our method of inversion, the reader is referred to Spakman and Nolet (1988) and Spakman (1991). A more extensive and generalized treatment, including the basics of nonlinear travel-time tomography, has been given by Spakman (1993). Below we give a summary derived from these papers.

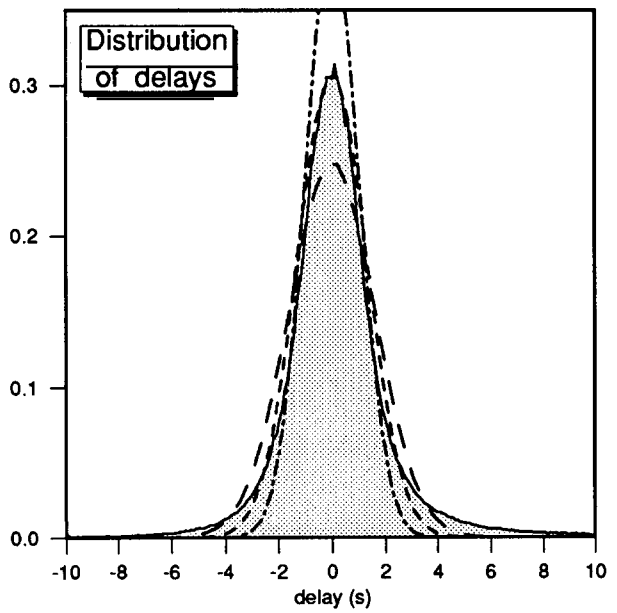

Fig. 3. Histogram of the 1.7 million ISC delays (solid line). Counts in 0.1 s intervals, scaled to unit surface (mean 0.12 s, r.m.s. value 1.9 s). For comparison, three Gaussian distributions are shown with standard deviations of 1 s, 1.3 s and 1.6 s, respectively. The curve with a standard deviation of 1.3 s attains the same maximum as the histogram of the data, but has greater width and falls off more rapidly.

3.1. Definitions

To arrive at a shorthand for notation, we define the following quantities (Fig. 5):

$s(\boldsymbol{r})$, $s^0(\boldsymbol{r})$ and $s^1(\boldsymbol{r})$: the Earth's true slowness field, the JB reference model and the improved reference model, respectively. By improved we mean that s^1 is a better approximation to the laterally averaged Earth structure than s^0.

$T_x(s)$, $\boldsymbol{x}$, $\boldsymbol{p}$ and $L(\boldsymbol{x};\ s;\ \boldsymbol{p})$: the true travel time, true source location, true station location and the true ray path connecting $\boldsymbol{x}$ and $\boldsymbol{p}$, respectively.

$T^0_x(s^0)$, $\boldsymbol{x}^0$ and $L^0(\boldsymbol{x}^0;\ s^0;\ \boldsymbol{p})$: the travel time, source location and the ray path connecting $\boldsymbol{x}^0$ and $\boldsymbol{p}$, respectively, defined in the JB model.

$T^1_x(s^1)$, $\boldsymbol{x}^1$ and $L^1(\boldsymbol{x}^1;\ s^1;\ \boldsymbol{p})$: the travel time, source location, and the ray path connecting $\boldsymbol{x}^1$ and $\boldsymbol{p}$, respectively, defined in the improved reference model $s^1(\boldsymbol{r})$.

Using the ray integral representation, we define the following functionals for travel times in an arbitrary slowness field $q(\mathbf{r})$:

$$T_x(q) = \int_{L(\boldsymbol{x};s;\boldsymbol{p})} q(\boldsymbol{r})\ \mathrm{d}l \tag{1a}$$

For $q(\boldsymbol{r}) = s(\boldsymbol{r})$ the true travel time $T_x(s)$ is obtained, which is stationary in accordance with Fermat's Principle (i.e. the ray path L is such that it renders the travel time $T_x(s)$ stationary). It should be noted that $T_x(q)$ is linear in its argument $q(\boldsymbol{r})$. We will use this characteristic in our derivation. The second functional is defined as

$$T^k_h(q) = \int_{L^k(\boldsymbol{h};s^k;\boldsymbol{p})} q(\boldsymbol{r})\ \mathrm{d}l^k \tag{1b}$$

where $k = 0$ or $k = 1$, denoting quantities in the JB reference model and in the improved reference model, respectively. The subscript h is used for our later need to substitute for the source location. For $\boldsymbol{h}$ we can substitute the hypocenters $\boldsymbol{x}$, $\boldsymbol{x}^0$ or $\boldsymbol{x}^1$, whichever is needed in the derivation below. For fixed $\boldsymbol{h}$ the travel time $T_h^k(q)$ is linear in its argument. In accordance with Fermat's Principle, the following travel times are stationary (minimum for P waves): $T_h^k(s^k)$, for all source locations $\boldsymbol{h}$, and for $k = 0$, 1. A travel time such as $T_x^1(s)$ must be interpreted as the travel time acquired in the true slowness field s, along the ray path $L^1(\boldsymbol{x}; s^1; \boldsymbol{p})$, i.e. the ray geometry in the slowness field s^1 using the source location $\boldsymbol{x}$. In general, this will not give a stationary travel time because L^1 need not coincide with L, hence for P waves $T_x^1(s) > T_x(s)$.

3.2. *Summary of the theory*

By definition, an ISC P-wave delay time d is expressed as

$$d = T_x(s) - T_{x^0}^0(s^0) + \Delta t + \Delta t^p + \epsilon \qquad (2)$$

where Δt is the origin time error, Δt^p is a station correction and ϵ is an error term incorporating all effects that are not explained by the other terms. It is assumed that a correction for the Earth's ellipticity has already been applied (e.g. Dziewonski and Gilbert, 1976). We want to rewrite this equation relative to some other known reference model $s^1(\boldsymbol{r})$ and apply linearization to the quantities proper. We define the slowness heterogeneity relative to reference model s^1 as $\Delta s = s - s^1$. To separate different contributions to the delay it is convenient to add the equation

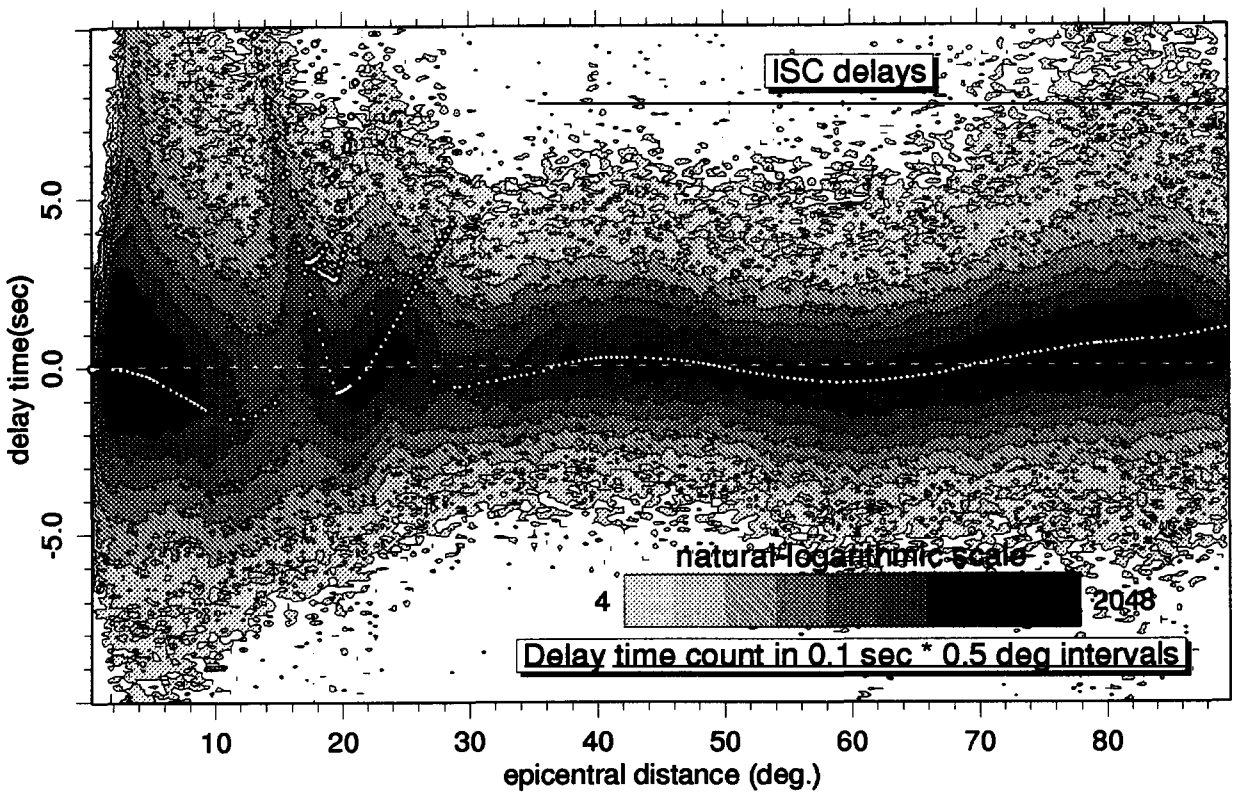

Fig. 4. Density plot (2-D histogram) of the ISC delays, showing the number of delays, counted in 0.1″ × 0.5° intervals; the contouring is logarithmic. White circles represent travel-time delays for a source at 33 km in the improved reference model (see section 4).

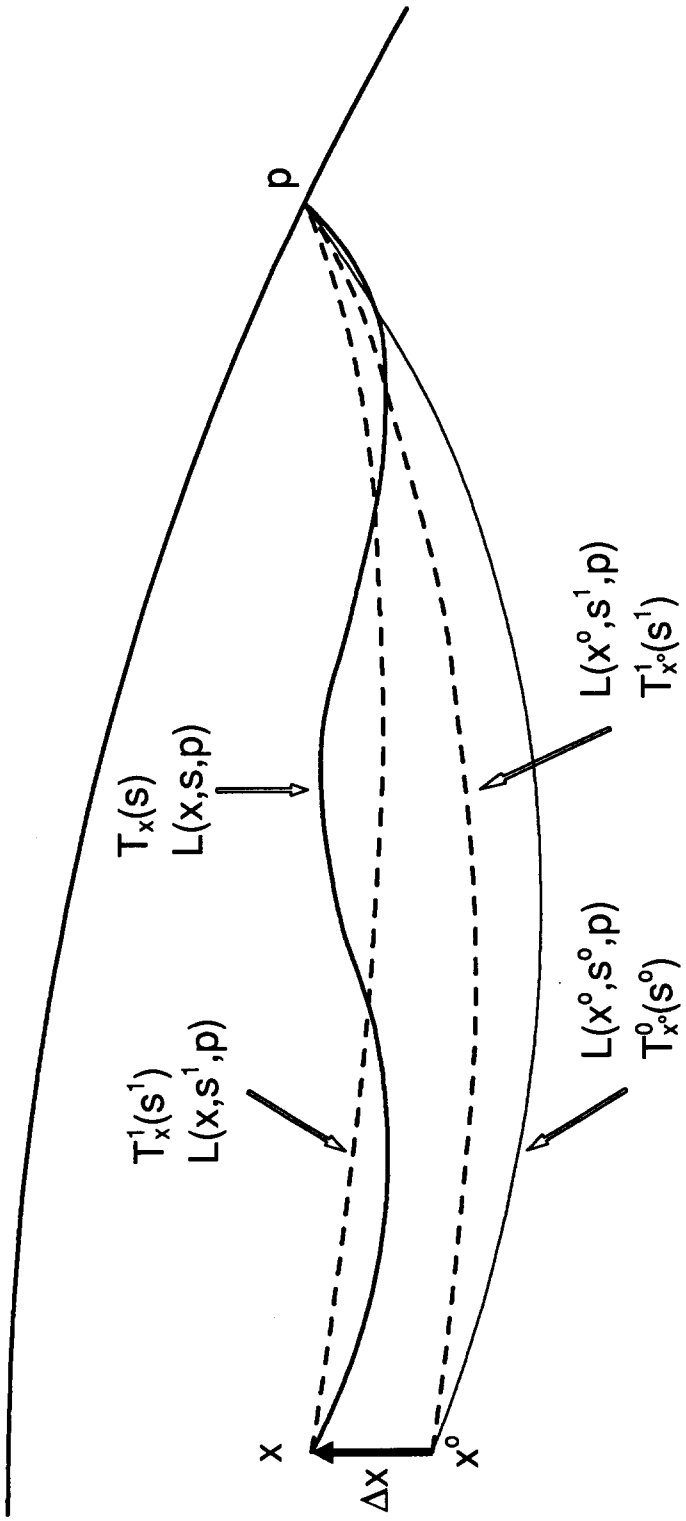

Fig. 5. Schematic depiction of ray paths and travel times defined in section 3.1.

$T_x^1(s) - T_x^1(s) = 0$ to the right-hand side of (2), and use the linearity of (1b) to write $T_x^1(s) = T_x^1(s^1) + T_x^1(\Delta s)$ (irrespective of the amplitude of $\Delta s(\boldsymbol{r})$), to arrive at

$$d = T_x^1(s^1) - T_{x^0}^0(s^0) + T_x^1(\Delta s) + \left[T_x(s) - T_x^1(s)\right] + \Delta t + \Delta t^p + \epsilon \qquad (3a)$$

In linearized tomography the term in brackets is always assumed to be negligible. The ray paths involved share the same end-points, and the difference in travel time is only due to the deviation of ray L^1 from L. If the ray path deviation is small, such that we can sensibly apply Fermat's Principle, the terms cancel in a first-order approximation. We have derived (3a) to invoke Fermat's Principle for the correct ray paths. Ray path L^1 is computed in s^1, the improved reference model, and it therefore provides a better guess of L than L^0. By applying Fermat's Principle we effectively replace L by L^1 and we replace the term in brackets by the approximation error ϵ_{Fermat} that remains. For direct P waves this error is always negative.

Adding, again for the convenience of separating different contributions, $\cdot T_{x^0}^1(s^1) - T_{x^0}^1(s^1) = 0$ to (3a), we find the equation we need to apply for a change in reference model to the data:

$$d = \left[T_{x^0}^1(s^1) - T_{x^0}^0(s^0)\right] + \left[T_x^1(s^1) - T_{x^0}^1(s^1)\right] + T_x^1(\Delta s) + \Delta t + \Delta t^p + \epsilon + \epsilon_{\text{Fermat}} \qquad (3b)$$

The first term in brackets describes the travel-time difference acquired between two rays that originate from the same source $\boldsymbol{x}^0$, the known ISC location, but travel through different slowness models, the new (improved) reference model and the JB model, respectively. Assuming that we know s^1, we can compute the difference and apply it as a correction to the ISC delay time. For a source at 33 km, this reference model delay is represented by the delay-time curve plotted with white circles in Fig. 4. The second term in brackets is essentially a mislocation term, in which the true source location $\boldsymbol{x}$ is unknown. It describes the difference in travel time in model s^1 between a ray originating from the ISC location $\boldsymbol{x}^0$ and a ray starting from the true source location $\boldsymbol{x}$. This term can be approximated by a Taylor expansion about $\boldsymbol{x}^0$, yielding

$$\left[T_x^1(s^1) - T_{x^0}^1(s^1)\right] = \Delta \boldsymbol{x} \cdot \nabla_{x^0}\left[T_{x^0}^1(s^1)\right] + \epsilon_{\text{source}-1} \qquad (3c)$$

where $\Delta \boldsymbol{x} = \boldsymbol{x} - \boldsymbol{x}^0$ is the mislocation vector we will invert for, ∇_{x^0} is the gradient operator in source coordinates evaluated at $\boldsymbol{x}^0$, and $\epsilon_{\text{source}-1}$ is the approximation error. The third term in (3b) describes the contribution to the delay of the lateral heterogeneity relative to model s^1. As $\boldsymbol{x}$ is unknown, we also make a Taylor expansion about $\boldsymbol{x}^0$ for this term:

$$T_x(\Delta s) \approx T_{x^0}(\Delta s) + \Delta \boldsymbol{x} \cdot \nabla_{x^0}\left[T_{x^0}^1(\Delta s)\right] = T_{x^0}^1(\Delta s) + \epsilon_{\text{source}-2} \qquad (3d)$$

where we incorporated the nonlinear inner-product term in the approximation error $\epsilon_{\text{source}-2}$.

Finally, to obtain a discrete parameter set we project the slowness anomaly Δs on a set of N orthonormal slowness functions $f_j(\boldsymbol{r})$, $j = 1, \ldots, N$ (in our case non-overlapping cells), which leads to

$$\Delta s(\boldsymbol{r}) = \sum_{j=1}^{N} s_j f_j(\boldsymbol{r}) + \delta s_{\text{projection}} \qquad (3e)$$

where the s_j are the projection parameters to be determined in the 3-D inversion. The expansion (3e) can only be approximate, as we do not expect the structure of the real Earth to be close to a block structure; therefore we have a projection error $\delta s_{\text{projection}}$. Applying the operator $T_{x^0}^1$ to both sides of (3e) yields

$$T_{x^0}^1(\Delta s) = \sum_{j=1}^{N} s_j T_{x^0}^1\left(f_j(\boldsymbol{r})\right) + \epsilon_{\text{projection}} \qquad (3f)$$

where $\epsilon_{\text{projection}} = T_{x^0}^1(\delta s_{\text{projection}})$ is the travel-time error associated with the slowness projection error. The projection coefficient $T_{x^0}^1(f_j(\boldsymbol{r}))$ for the jth cell can be set equal to the length of the ray segment in this cell, in which case the projection parameter s_j is the volume average of the slowness heterogeneity in cell j.

Substituting Eqs. (3c), (3d) and (3f) in (3b) we finally obtain the equation we will use for model-

ing an ISC delay time relative to an improved reference model s^1:

$$d - \left[T_{x^0}^1(s^1) - T_{x^0}^0(s^0)\right] = \sum_{j=1}^{N} s_j T_{x^0}^1\left[f_j(\boldsymbol{r})\right] + \Delta \boldsymbol{x} \cdot \nabla_{x^0}\left[T_{x^0}^1(s^1)\right] + \Delta t + \Delta t^p + \epsilon_{\approx} \quad (4)$$

where

$$\epsilon_{\approx} = \epsilon + \epsilon_{\text{Fermat}} + \epsilon_{\text{source}-1} + \epsilon_{\text{source}-2} + \epsilon_{\text{projection}}$$

where $\epsilon_{\approx}$ stands for the sum of all error terms. Equation (4) is the same linear equation as used by Van der Hilst and Spakman (1989) and Van der Hilst (1990). It leads to a matrix equation of simultaneous constraints on the model parameters if applied to many data.

The statistics of $\epsilon_{\approx}$ are unknown. It constitutes the formal error made in any tomographic investigation using travel times. The least we know is that the implicit error introduced by the application of Fermat's Principle ϵ_{Fermat} leads to only negative contributions to $\epsilon_{\approx}$ which may give $\epsilon_{\approx}$ a biased statistical distribution. The size of the source errors depends on how close s^0 is to s^1 and how close s^1 is to s. The relationship between delays and event location is strongly nonlinear. The linearized effect of event mislocation on the delay time in the model Eq. (4) only attempts to account for the mislocation caused by a change in reference model. As the first-order Taylor expansion is exact only in the direct vicinity of the reference source (Lee and Stewart, 1981) the approximation errors may still be large, i.e. of the order of the delay, when the mislocation is related to a change in reference model (Van der Hilst et al., 1993), and even for the nonlinear term related to the combined effect of heterogeneity and mislocation (see Eq. (3d)) (Spakman, 1988; Van der Hilst and Engdahl, 1992). The error $\epsilon_{\text{projection}}$ may only be small and randomly distributed if the adopted basis functions are suitable to give an adequate description of the real Earth structure. This may be more the case if the parametrization is detailed and local, for instance if many small cells are used.

3.3. *Implementation of the theory for large-scale problems*

Basically, we explain a delay time by contributions from four sets of quantities—the slowness heterogeneity s_j, $j = 1, \ldots, N$ of the target mantle volume, station statics Δt^p for all stations, mislocation vectors $\Delta \boldsymbol{x}$ and origin time errors Δt. The data are inverted for simultaneous estimates of model parameters associated with these quantities. As we include station statics and event parameters, there is no need to use the so-called relative residuals that originated from the theory in the pioneering study of Aki et al. (1977). Instead of correcting the delays for event and station averages we try to invert for these effects. This implies that our results for the slowness heterogeneity can be directly related to the average velocity at depth to obtain percentage deviations relative to ambient mantle velocities. To model the mantle heterogeneity field below the European–Mediterranean region we have projected the Earth's slowness field on a cell (block) structure to a depth of 1400 km (Fig. 1). Details on cell sizes and cell model orientation are presented in the caption of Fig. 1. Cell layering and the volume average of cell reference velocities can be found in Table 1.

The total number of model parameters is 77 507: $62 \times 40 \times 20 = 49\,600$ cells, 2259 station time corrections, and 25 648 event parameters, respectively. Following Spakman and Nolet (1988), we have reduced the number of event parameters to 25 648 by estimating average mislo-

TABLE 1

Cell layer division and average velocity of PM2 model

km	km	km s^{-1}	km	km	km s^{-1}
0	33	6.228	33	70	7.853
70	120	8.028	120	170	8.117
170	220	8.109	220	275	8.176
275	330	8.414	330	390	8.732
390	460	9.319	460	530	9.710
530	600	9.941	600	670	10.151
670	740	10.899	740	820	11.016
820	920	11.183	920	1020	11.360
1020	1120	11.535	1120	1220	11.686
1220	1320	11.841	1320	1420	11.988

cation vectors and origin time errors for clusters of events rather than assigning four event parameters to each event. In the latter case, we would need of the order of 250 000 parameters simply to describe event effects. For regional events an event cluster is defined by all earthquakes in a block of dimensions $0.5° \times 0.5° \times 35$ km. With the event cluster approach we attempt to account for the averaged effect of the slowness heterogeneity (including reference model bias) on event mislocation. For teleseismic events we used larger clusters defined by blocks with dimensions $2.5° \times 2.5° \times 100$ km. For a teleseismic event cluster we only estimate one average time correction for the delays originating from the events in the cluster instead of four source parameters. This time correction is used to account for the combined effects of near-cluster heterogeneity and for the average delay acquired in the lower mantle between source (cluster) region and the cell model.

We reduce the number of data for inversion and attempt to suppress random error in the data by using the composite ray approach of Spakman and Nolet (1988). In the matrix equation one row may be composed of at most five ray paths. For the row computation we do not replace these rays by one average ray (usually called the summary ray) but retain the individual contributions of each ray in the matrix row (for details, see Spakman and Nolet (1988) and Spakman (1991)). In the averaging process, delays associated with an impulse arrival (denoted by 'i' in the ISC Bulletins) obtained the weight two, rays with an emergent ('e') onset obtained a weight 0.5, and if the onset is not reported the weight is unity. The composite ray approach leads to 615 123 matrix equations from which the values of 77 507 model parameters will be estimated.

The matrix equation constructed from (4) using composite rays and delays has the following structure:

$$(\boldsymbol{R} \mid \boldsymbol{H} \mid \boldsymbol{P})\boldsymbol{m} = \boldsymbol{d} \text{ with } \boldsymbol{m} = \begin{bmatrix} \Delta s \\ \Delta h \\ \Delta p \end{bmatrix} \tag{5}$$

where $\boldsymbol{R}$ is the matrix of ray projection coefficients, $\boldsymbol{H}$ is the matrix of event-cluster mislocation coefficients (including origin time error coefficients) and $\boldsymbol{P}$ is the matrix of station correction coefficients. The corresponding vector of model parameters is $\boldsymbol{m} = (\Delta s\ \Delta h\ \Delta p)^T$, and $\boldsymbol{d}$ is the delay time vector of reference-model corrected delays, i.e. the vector generalization of the left-hand side of Eq. (4). The reader is referred to Spakman and Nolet (1988), and Spakman (1991) for details of how the solution of (5) can be estimated using the damped least-squares algorithm LSQR (Paige and Saunders, 1982) and a special smoothing strategy. Spakman (1993) gave a brief comparison of our approach with those of others.

4. Determination of a regional reference model for tomography

Using the method proposed by Van der Hilst and Spakman (1989), we inverted the variation in the delay-time data as a function of distance (see Fig. 4) into velocity anomalies as a function of depth only relative to the JB model. This inversion problem is strongly nonlinear and is tackled by an interactive trial-and-error approach. We started changing the JB model from crustal levels downward. After each change a travel-time curve is computed from which we subtract the JB travel times. The resulting delay-time curve is compared with the observations and the model change is rejected if the fit is poor. All models generated in this way and which give a reasonable fit to the data are characterized by the presence of a high-velocity lithosphere, a low-velocity layer with a small negative velocity gradient, and by strong velocity gradients or seismic discontinuities at about 400 and 670 km depth. These features are at least required by the data. A number of trade-offs between model features proved to be unresolvable, for instance, the trade-offs between the amplitude and width of the low-velocity zone and between the depth of a discontinuity and the velocity jump across the discontinuity. We fixed the discontinuities at 405 km and 670 km, respectively. Of the possible models we took the PM2 model (Fig. 6). Paulssen (1987) derived a number of P-velocity models for the European mantle for different source–receiver combinations. The vari-

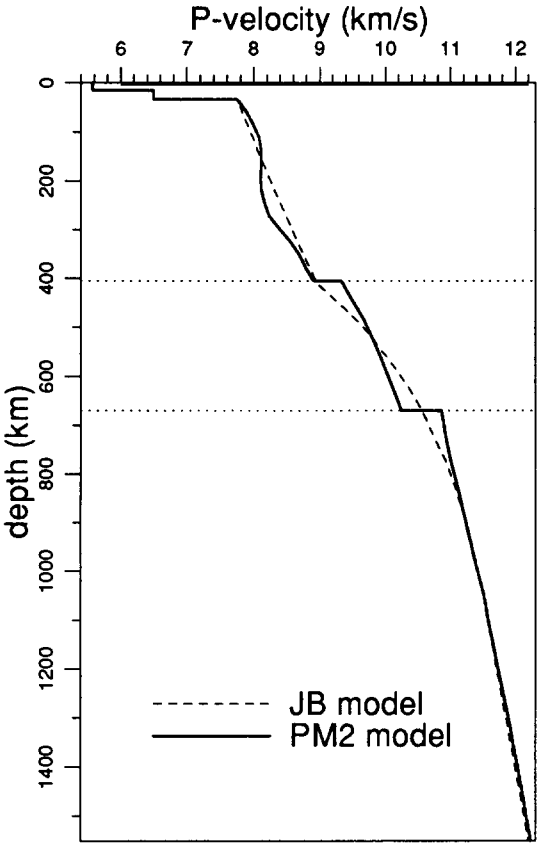

Fig. 6. The JB model and the improved reference model PM2.

ation in models she obtained demonstrates the strong velocity heterogeneity present in the European mantle. Above 400 km our PM2 model can be viewed as an average of Paulssen's models, and between 400 and 670 km PM2 is slightly faster.

The density plot of all reference model corrected data (and then averaged into composite delays) is displayed in Fig. 7(b). These are the data which we will use for the 3-D mapping of mantle structure. The delay-time correction calculated from the improved reference model removes most of the major trends in the ISC data. However, the correction is not perfect. The PM2 model explains 53% of the variation of the mean with distance in the ISC delays. This r.m.s. reduction is calculated from the variation of the mean in Fig. 7(a) with respect to that in Fig. 7(b). Specifically, at teleseismic distances the delays are on average slightly negative. If we compute the data fit from the change in all delay times then we obtain an r.m.s. reduction of only 3%, much less than the 10% obtained by Van der Hilst and Spakman (1989). The reference model bias in ISC delays is a systematic error that is independent of the delay-time value. Large delays for fixed source depth and distance obtain the same correction as small delays for the same source depth and distance. Therefore, removing the reference model bias need not affect the r.m.s. value of the entire delay-time set in the same proportion as it affects the r.m.s. reduction in the mean as a function of distance. Moreover, our correction does not include the effect of event relocation, which may be large (Van der Hilst et al., 1991; Van der Hilst and Engdahl, 1992) and which we try to estimate in the inversion. Despite the small overall improvement in the data, we expect that model PM2 accounts for the effects of nonlinearity associated with the major features by which the average Earth departs from the JB model below Europe: a high-velocity lithosphere, a low-velocity zone below most of the European–Mediterranean region, and the presence of seismic discontinuities.

Although the effect of a reference model change on the entire data set is small, the ray geometry changes drastically (Van der Hilst and Spakman, 1989; Zielhuis et al., 1989). This is illustrated in Figs. 8(a) and 8(b) for a source at 0 km depth and stations at regular distances from the source. The geometry of teleseismic rays is hardly affected; however large differences can be observed for rays bottoming in the upper 800 km. Any model which possesses the above-mentioned features and which gives a reasonable fit to the average trend in the data (see Fig. 7(a)) would largely resolve the nonlinear effects on the ray geometry. Further, differences between such models would, on average, lead to differences in ray geometry which are only one order of magnitude smaller than the differences between PM2 and JB ray paths (Fig. 8(b)). For these (and other) reasons, Van der Hilst et al. (1991, 1993) have taken the global iasp91 model (Kennett and Engdahl, 1991) as a reference model from the

start instead of determining a regional reference model.

5. Inversion for the 3-D P-wave velocity heterogeneity

Before presenting inversion results we will first consider some preliminaries which will enable us to display the results in an economical way combined with results from reliability tests.

5.1. *Data inversions*

To study the effect of the change in reference model we perform inversions of the ISC data relative to the JB model and of PM2 data relative to the PM2 model (the equations for the ISC inversion are easily derived by identifying $s^1 = s^0$ and superscripts accordingly in (4)). The r.m.s. data fit obtained in the inversions of the ISC data and of the PM2 data is about the same: 28% within 30 iterations of the LSQR algorithm. In the last iterations the data fit changes by only 0.1%, indicating that little improvement of the data fit is to be expected in subsequent iterations. The data fit obtained only ensures convergence to some model that can explain the data better than either of the two reference models can. The r.m.s. fit is a complex measure of convergence that depends on the smoothing, scaling and damping applied, on the degree of dependence between the model parameters, and on the signal-to-noise ratio of the data. The last, of course, includes the effects of all modeling and approximation errors. After 30 iterations the r.m.s. value of the residues is about 1 s, which is comparable with the anticipated upper bound of the standard error in delay times and at least not significantly smaller than the standard error. How much the modeling and approximation errors gathered in $\epsilon_{\approx}$ (Eq. (4)) contribute to the error in delays is unknown. Furthermore, inconsistencies in the data as a result of heterogeneity outside the cell model that is not explained by event or station parameters nor by the cells in the model may also be a source of error in the data that limits the data fit. Finally, the convergence to the least-squares solution is determined by the scaling of the matrix equation (Spakman and Nolet, 1988). Our scaling is such that the LSQR algorithm provides the largest convergence in well-sampled areas in the model. Cells in poorly sampled regions are to a lesser extent allowed to fit the data. This also limits the data fit. Both the effects on the data fit of lateral heterogeneity outside the model and the scaling of the equations are of course dependent on the resolution of model parameters. To the data fit obtained in the inversion of PM2 delays we have to add the 3% improvement attained by the change in reference model only. This renders a slightly better data fit for the two-step inversion with PM2 delays.

5.2. *Assessing the spatial resolution*

For inversions involving many ($O10^5$) model parameters, formal estimates of resolution can only be obtained at the expense of a tremendous amount of computing time. To estimate the formal resolution for one cell we have to perform computations comparable in size with one inversion of the data (Nolet, 1985, Trampert and Leveque, 1990). Therefore, we resort to sensitivity analysis using synthetic test models (Humphreys and Clayton, 1988; Spakman and Nolet, 1988). If the data matrix equation to be solved is given by $\boldsymbol{Am} = \boldsymbol{d}$ then in sensitivity analysis $\boldsymbol{m}$ is replaced by some synthetic model $\boldsymbol{m}_e$. By forward calculation, synthetic data are computed as $\boldsymbol{d}_e$ ($= \boldsymbol{Am}_e$). To the synthetic data a noise vector $\boldsymbol{\epsilon}$ may be added to mimic the presence of noise in the actual (ISC or PM2) delays and to study the effect of noise on the solution. The next step is to solve $\boldsymbol{Am} = \boldsymbol{d}_e + \boldsymbol{\epsilon}$ for the response model $\boldsymbol{m}_r$. An impression of the spatial resolution can now be obtained by comparing the exact synthetic model $\boldsymbol{m}_e$ with the response model $\boldsymbol{m}_r$. The usefulness of such 'resolution' tests is limited, as the best they can provide is insight into how well the sampling of the model by the reference rays (represented by $\boldsymbol{A}$) can resolve (artificial) anomalies (Spakman, 1991). The consistency between the synthetic data $\boldsymbol{d}_e$ and the ray paths is destroyed by adding the noise vector $\boldsymbol{\epsilon}$; however, usually $\boldsymbol{\epsilon}$ is taken to be Gaussian distributed, which is in

accordance with using a least-squares method for inversion. Therefore, by using sensitivity analysis we cannot study the important things that we would like to know, i.e. the correlation of the real data with the real ray paths, specifically, the effects of non-Gaussian noise (data errors and modeling errors) on the solution, and the actual spatial resolution (Spakman, 1991; Van der Hilst et al., 1991, 1993). Furthermore, the results depend on the choice of the synthetic model (e.g. Blanco and Spakman, 1993). Nevertheless, sensitivity analysis is very useful, as, under the assumption that the reference rays approximate the real rays, it provides the information on where in the mantle volume studied we may potentially find high, or poor resolution. If it happens that the synthetic model adopted has no components in the null space of A then sensitivity analysis may overestimate the resolution in the model (Leveque et al., 1993). Using different synthetic models may minimize this risk.

In our analysis we use two synthetic models. The first is a spike model consisting of a regular pattern of single-cell anomalies ('spikes') with an amplitude of 5% relative to the ambient mantle velocities. The 'spike' cells are separated laterally by at least two cells with 0% amplitude. Vertically, the regular pattern is shifted by half of the spike distance to avoid columns of 'spike' cells in depth. This synthetic model allows us to study the ability to image short-wavelength (cell-size) anomaly patterns. The second synthetic model aims at studying the resolving power for smoothly varying anomaly patterns. The model consists of a

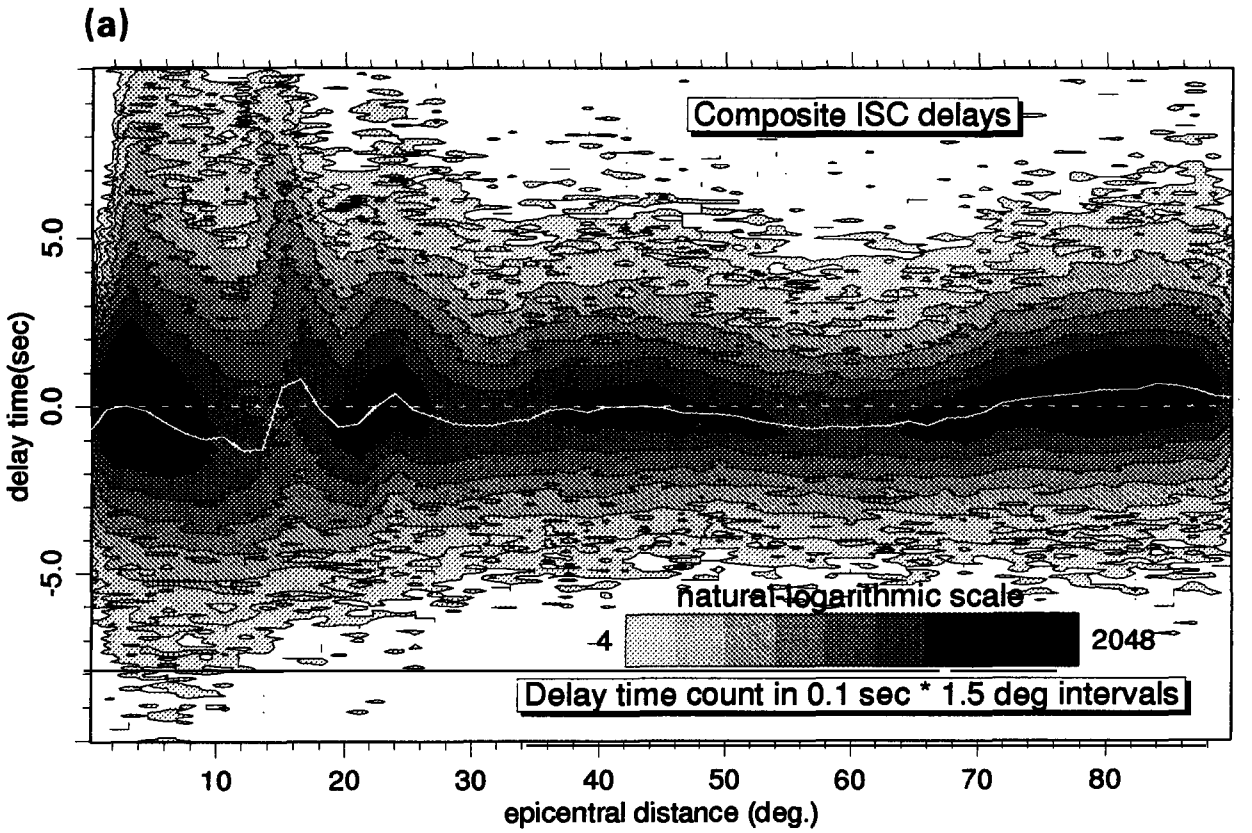

Fig. 7. (a) Density plot of composite ISC delays. Solid white line denotes the average as a function of distance. (b) Density plot of composite PM2 delays, i.e. ISC delays corrected for the reference model bias between PM2 and JB according to the left-hand side of Eq. (4).

harmonic variation of velocity heterogeneity in each layer with a wavelength of six cells and amplitude variation between −3% and +3%. The anomaly pattern in adjacent cell layers is shifted by half a wavelength (three cells), which gives on average a-jump of a 3% anomaly across cell layer interfaces. Both models have been extensively discussed by Spakman and Nolet (1988) and Spakman (1991). Other synthetic models are the so-called 'checkerboard' models (e.g. Inoue et al., 1990) or models specifically designed for studying the resolution of special objects such as subducted slabs (Spakman et al., 1989; VanDecar, 1991; Blanco and Spakman, 1993).

In our tests we add Gaussian distributed noise to the synthetic data $\boldsymbol{d}_e$ with a standard deviation that results in a similar r.m.s. data fit of about 30% in 30 iterations. For the spike test this standard deviation is 0.6 s and for the harmonic test 1.0 s. The synthetic values for the mislocation and station part of the model vector are set to zero. Lack of resolution between the cell solution and the other parameters will result in non-zero amplitudes for the latter in synthetic tests.

6. Inversion results

In the following, we denote by EUR89A the inversion result obtained from ISC data using the JB model, and by EUR89B the 3-D image obtained from inverting PM2 data relative to model PM2. The complete solution EUR89B, together with two sensitivity tests and hit count, is displayed in 20 figures, one for each layer, in Appendix A. Reference velocities and cell layer thicknesses are displayed in Table 1. Four panels are shown for each layer. The layer depth is

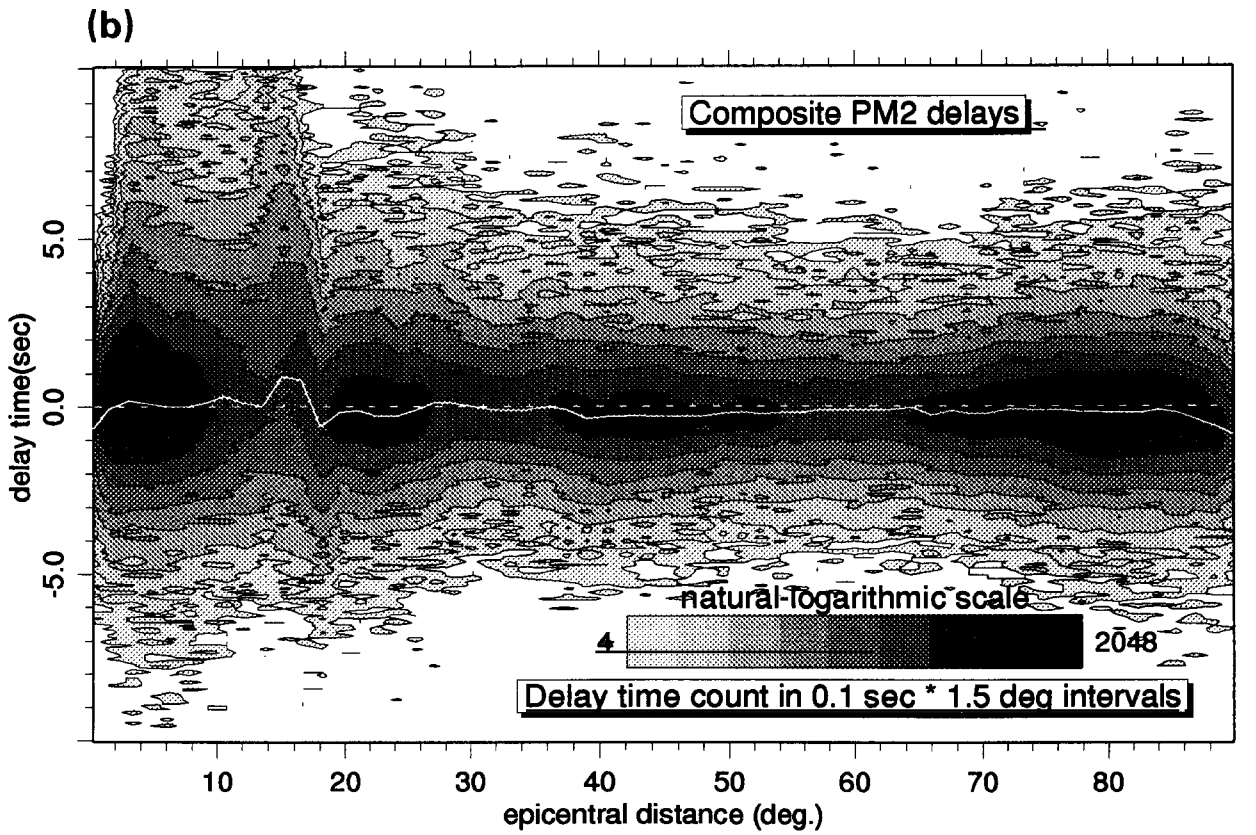

Fig. 7 (continued).

indicated in the upper left corner and stands for the midpoint depth of a cell layer.

The upper left panel gives the EUR89B result contoured between −2% and +2% relative to the reference (PM2) mantle velocity. The contour interval is 0.5%. Velocity anomalies exceeding the scale are contoured with either the upper or lower shading color. In the lower left panel the

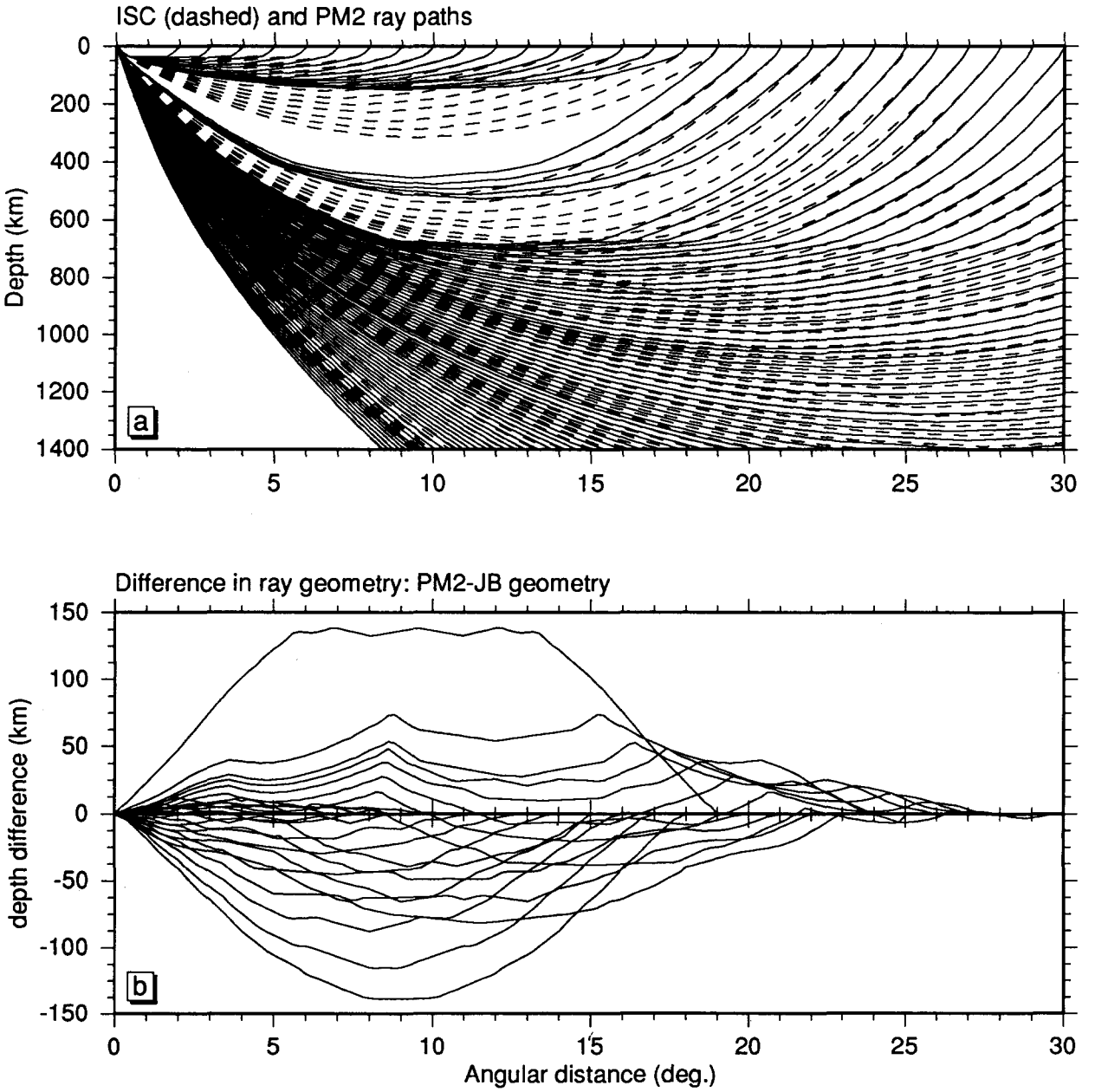

Fig. 8. (a) ISC rays (dashed) and PM2 rays (solid) for a source at 0 km depth and for rays arriving at every degree between 0° and 90°. Only first arriving rays are plotted. (b) The difference in depth between PM2 rays and JB rays of Fig. 9(a) as a function of distance. Only those rays arriving within 30° are shown.

10-logarithm of the hit count is contoured. Cells not sampled, or cells sampled by more than 10 000 rays obtain the shading of the outer limits of the scale. The result of the spike sensitivity test can be found in the upper-right panel. The regular pattern of small gray spots denotes the exact location of the cell anomalies. The line contouring gives the inversion response. The line separation is 0.5% of the anomaly value (spike amplitude is 5%). The last panel displays the result of the harmonic sensitivity test using the same contour scale as for EUR89B. Amplitudes of the exact harmonic model vary between −3% and +3%. Below, we focus first on the hit count and sensitivity tests in map view and in vertical slices, then on reference model effects to gather all the information needed, and finally on the significance of the solution EUR89B.

6.1. Ray sampling; hit count

The cell hit count is defined as the number of rays sampling a cell. In mantle studies this quantity can vary considerably, even from one cell to another. The importance of the hit count is not only that it provides immediate insight into how well cells or mantle areas are sampled (a better measure for that would be the ray density tensor of Kissling (1988)), but also that it has a strong effect on the solution in the sense that amplitudes of the imaged structure correlate to some extent with the cell hit count. The latter depends on the number of iterations performed combined with the scaling of the matrix equations (Spakman, 1988; Spakman and Nolet, 1988). Therefore, we cannot interpret tomographic results without taking the hit count into account.

The ray sampling varies considerably in the cell model. In the upper 400 km the hit count ranges in every layer from zero to more than 10 000 rays in some cells. Below 400 km the pattern becomes smoother, and the hit count typically varies between several tens and thousands of rays per cell. Low hit counts exist near the vertical boundaries of the cell model. The central part is well sampled. With increasing depth below 500 km the area of high sampling becomes larger to the north and east, and shifts towards the NNE. Rays emerging from the north to east and coming from Circumpacific and Indonesian Arc events cause these deeper mantle trends in the hit count (see Fig. 2).

In more detail, the following can be inferred, which will prove useful in the interpretation of the sensitivity tests. The hit count in the crustal layer (16 km) is completely determined by the presence of stations and earthquakes, as rays emerge in the crust with relative steeply inclined angles (Fig. 8(a)). It should be noted that directly below the crust (51 km) the hit count variation is already rather smooth, as a result of the almost horizontal geometry of Pn-type rays sampling the lithosphere only (Figs. 2 and 8(a)). For the same reason the deeper lithosphere below Russia and the Ukraine is mainly sampled in the layers centered about 95 km and 145 km but not at depths around 195 km. Specifically in this and in the next layer (247 km) we observe a drop in hit count in the central part of the cell model and below central Turkey. These relative decreases may be related to two combined circumstances: (1) the relatively few stations and events lead to a local sampling by steeply inclined rays from or to teleseismic distances only; (2) the presence of a low-velocity layer in the PM2 model and the distribution of events and stations in the European–Mediterranean region combine to give an undersampling of the mantle specifically below the two areas mentioned. In general, the low-velocity layer in PM2 causes decreased sampling by regional rays of the depth range 160–350 km (Fig. 8(a)). Sampling of this depth range is provided primarily by steep rays from or to large distances. Furthermore, many stations in central Europe and events in the Aegean region are separated by distances larger than 19°, so below these regions a sampling by regional rays is provided (see Fig. 8(a)).

The velocity jump across the 400 km discontinuity is also visible in the ray hit count (compare the hit count in the layers centered at 360 and 425 km depth). Many rays are strongly refracted across the discontinuity, causing a sampling by subhorizontal ray paths of the model below the discontinuity (Fig. 8). Similar observations can be made for the hit count patterns just above and

below the 670 km discontinuity. In the lower mantle, rays belonging to epicentral distances between 25° and about 55° all bottom between 670 and 1400 km, which provides a predominant subhorizontal sampling in the areas with large hit count.

6.2. *Sensitivity tests*

6.2.1. *Map view images (Appendix A)*

Comparison of the sensitivity test results with the density of ray sampling leads to the inference that high hit count correlates on average with a reasonably high-amplitude response and low hit count correlates with small slowness anomaly amplitudes. This correlation is well understood and must be interpreted as follows: in regions poorly constrained by the data (ray paths), the scaling of our inverse problem is such that we take advantage of the intrinsic damping property of the LSQR algorithm (Van der Sluis and Van der Vorst, 1987) to obtain smooth and small-amplitude heterogeneity (Spakman and Nolet, 1988).

Let us now concentrate on how well the illumination of the cells by PM2 ray paths can resolve mantle structure. In the crustal layer (16 km) the amplitude response is poor, in spite of a high sampling of the central part of the model. We suspect that the cause may be found in a trade-off between cell amplitudes and station corrections, which results in a lack of vertical resolution. The amplitude variation in the result of the harmonic test (HMT) can still be recognized and some of the cells in the spike test (SPT) have a reasonable response, but resolution is poor in this layer.

In the layers centered about 51 km and 95 km the HMT and SPT models are almost excellently recovered in the well-sampled region. Outside this region all kinds of detailed observations can be made about the spatial resolution. For instance, if we compare the HMT and SPT results for Spain and the Western Mediterranean at 95 km, then we may infer that the HMT model is better recovered than the SPT model. This illustrates the dependence of the resolution estimates on the test model. Anomalies on the scale of the cell dimensions can hardly be resolved, whereas anomaly patterns with an amplitude variation of the order of three cells are at least detectable.

At this point, a remark on model dependence of sensitivity tests seems appropriate. The difficulty in interpreting results from test models such as the 'checkerboard' model or the harmonic model is that lack of resolution causes averaging (smearing) of amplitudes between cells in the test result. In such test models it is often difficult to distinguish between a predominant lack of vertical resolution and poor lateral resolution. When we use the SPT model this separation can often be studied easily. The SPT, model contains many zero-amplitude cells surrounding the spike cells. The spike response (or impulse response) can then be studied, to decide on the direction in which lack of resolution occurs. Examples will be given below. The drawback of the SPT model is that, if it results in a poor inversion response, the inability to image small detail cannot be used to conclude that large anomalies (of the order of many cells) cannot be imaged or detected well (e.g. Blanco and Spakman, 1993). This has been illustrated above for the Spanish and Western Mediterranean region. Even where the HMT model fails to give a good response, anomalies with much larger wavelength can potentially still be imaged with a high spatial accuracy, i.e. accuracy relative to the spatial size of the large anomaly (Blanco and Spakman, 1993). Conversely, the ability to image small detail need not necessarily imply a good resolution for larger objects if (by chance) the adopted test model can be constructed completely from eigenvectors with non-zero eigenvalues (Leveque et al., 1993).

In the layer at 145 km the spatial resolution in the central part of the model can still be called reasonably good. The fact that synthetic amplitudes tend to be underestimated in this and subsequent layers is primarily due to the incomplete convergence of the solution to the least-squares solution in the first 30 iterations of the LSQR algorithm (Spakman and Nolet, 1988). Lack of lateral resolution can be inferred in the eastern part, where the spike response is smeared in the lateral sense. Lack of vertical resolution occurs in NW Europe, where smearing of the spike response across layers can be inferred from the

presence of spike anomalies in places where no spike is located in this layer (it should be recalled that the pattern of spikes in adjacent layers is shifted by half of the spike distance).

In the four layers below 145 km resolution is much poorer. This is caused by the low-velocity zone in PM2 combined with a jump in velocity at 400 km. As we have discussed for the hit count patterns, this depth range is predominantly sampled by rather steeply inclined rays. Direct P waves tend to bottom below 400 km and above 150 km in model PM2 (see Fig. 8). Lack of depth resolution is most important between 150 and 400 km. This can easily be inferred from the SPT test, which shows leakage of many spikes from adjacent layers. However, the lateral resolution is, on average, good; the spike responses are almost all nearly circular, with only in some cases some indication of lateral smearing. This implies that in the map view images the lateral variation of anomalies in EUR89B is rather well resolved. What is uncertain to some extent is the depth at which the anomalies are located. We note that the apparent east–west smearing visible in the HMT result between 150 and 400 km does not result from lack of lateral (east–west) resolution but from poor depth resolution. The synthetic pattern of the HMT model is shifted by half a wavelength to the right in subsequent layers. In an east–west cross-section of the synthetic model we would find synthetic anomalies of the same sign. Both lack of depth resolution and poor lateral resolution in the east–west direction could produce a smearing of anomalies as is visible in the HMT result. However, the SPT result demonstrates that primarily poor depth resolution is the cause for the apparent east–west smearing in the HMT result.

Below 400 km the spatial resolution improves again. Areas with a predominant lack of vertical resolution or poor lateral resolution can be identified easily from the SPT result. One could infer that anomaly patterns with an amplitude variation over several cells are detectable in the depth range 400–670 km, although we cannot rely too much on the detailed variation of their amplitudes and contours. We note that below the Western Mediterranean the SPT result is very poor, whereas the HMT indicates that at least sign changes in anomaly patterns over many cells (3, 4, 5,...) are detectable.

The spatial resolution in the lower mantle is rather high in the well-sampled region of the cell model. In the Mediterranean and Western Europe, we find again the difference in the inversion response between the HMT and SPT results, indicating that although the resolution for small detail may be poor larger anomaly patterns may be well detectable. At all depths, good examples can be found in the SPT result of a lack in lateral resolution caused by the predominantly subhorizontal sampling of the lower mantle. The vertical resolution is much better, considering the few spike responses leaking from adjacent layers.

In conclusion, we believe that the resolution for anomaly patterns on the scale of several to many cells is reasonably high for most of the mantle volume studied. Estimates for resolution for details on the scale of one cell, or for a particular area, can only be made from a detailed 3-D analysis of the sensitivity test results. The inferences we have made in this section are sufficient for studying the resolution of larger-scale anomaly patterns in EUR89B.

Station statics and event parameters obtained nonzero values in the synthetic tests, indicating that a trade-off exists between the solutions of all three parameter sets. We would have obtained a much better sensitivity result for the cells if we had ignored the station and event parameters in the synthetic tests. Also, results of synthetic tests improve if one ignores synthetic data noise. Obviously, inferences drawn from such tests are less useful for studying the resolution in real data inversions.

6.2.2. Vertical slices (Appendix B)

In Appendix B, nine slices are presented for the investigation of sensitivity results in the vertical direction. The layout for the inversion results is similar to that for the map view figures of Appendix A. In addition, at the top, two maps are plotted which give the orientation of each depth section. The slice for EUR89B, the hit count and the HMT result are computed along the straight line in the center of the map on the

(a)

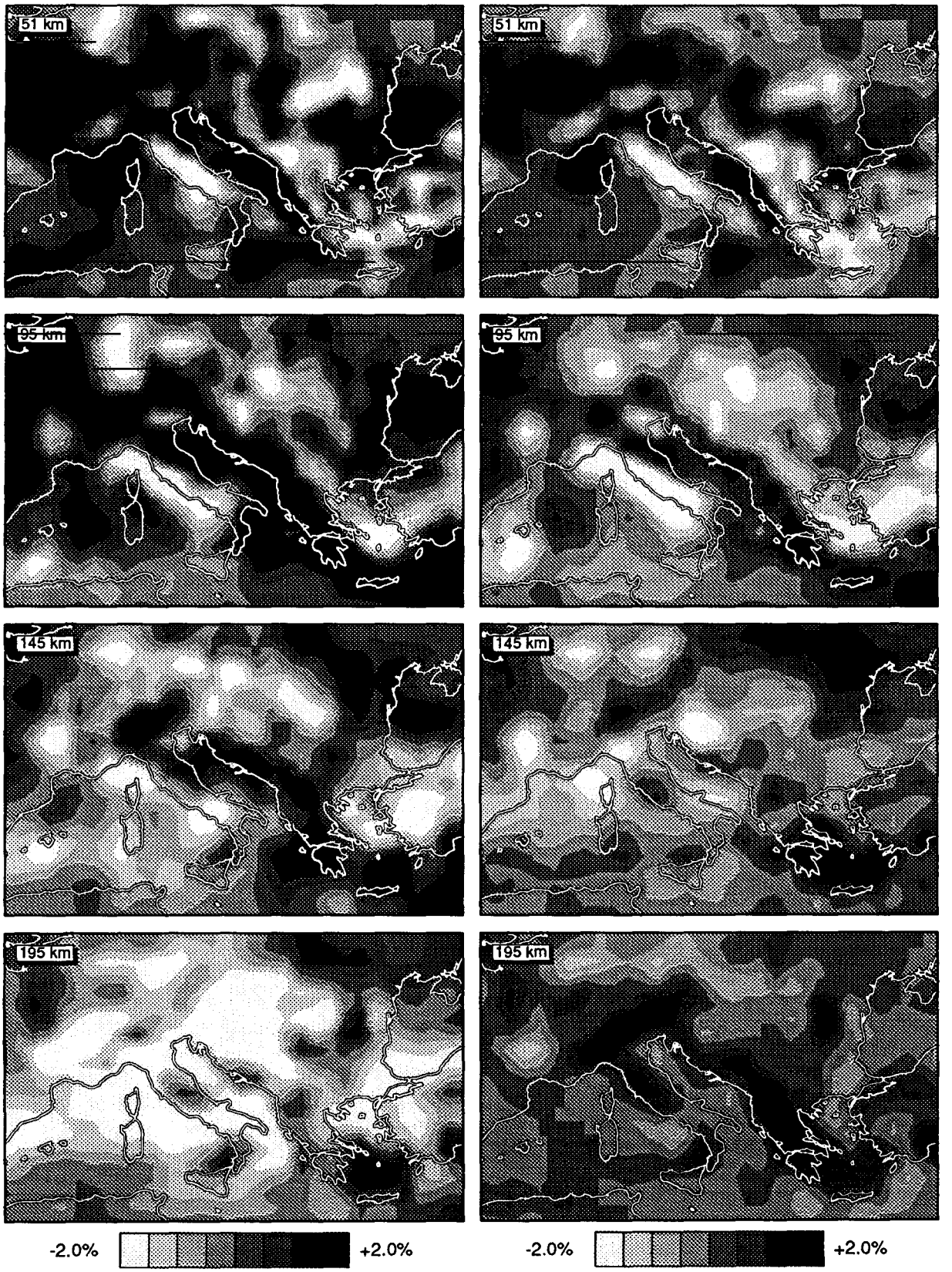

(b)

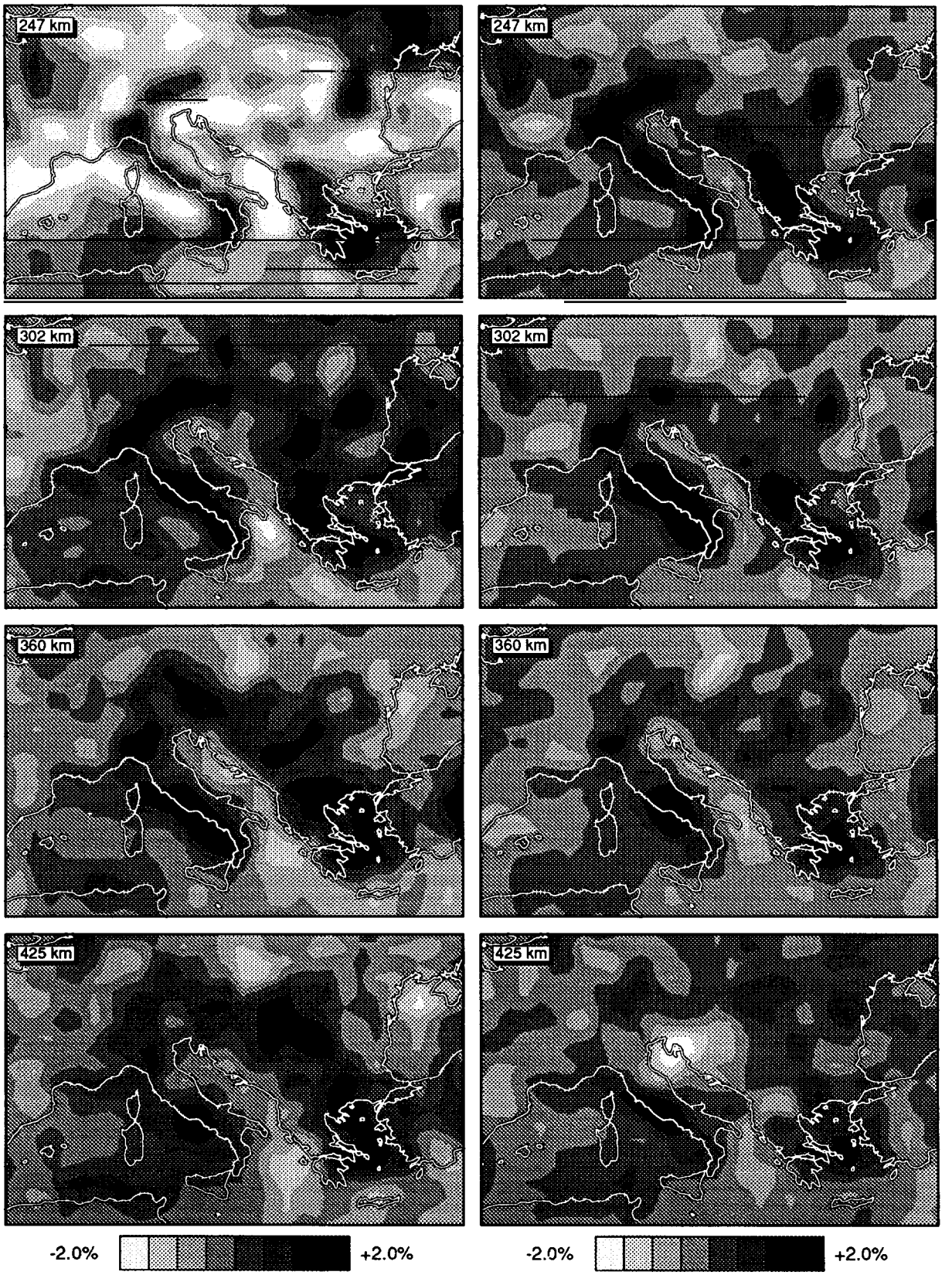

(c)

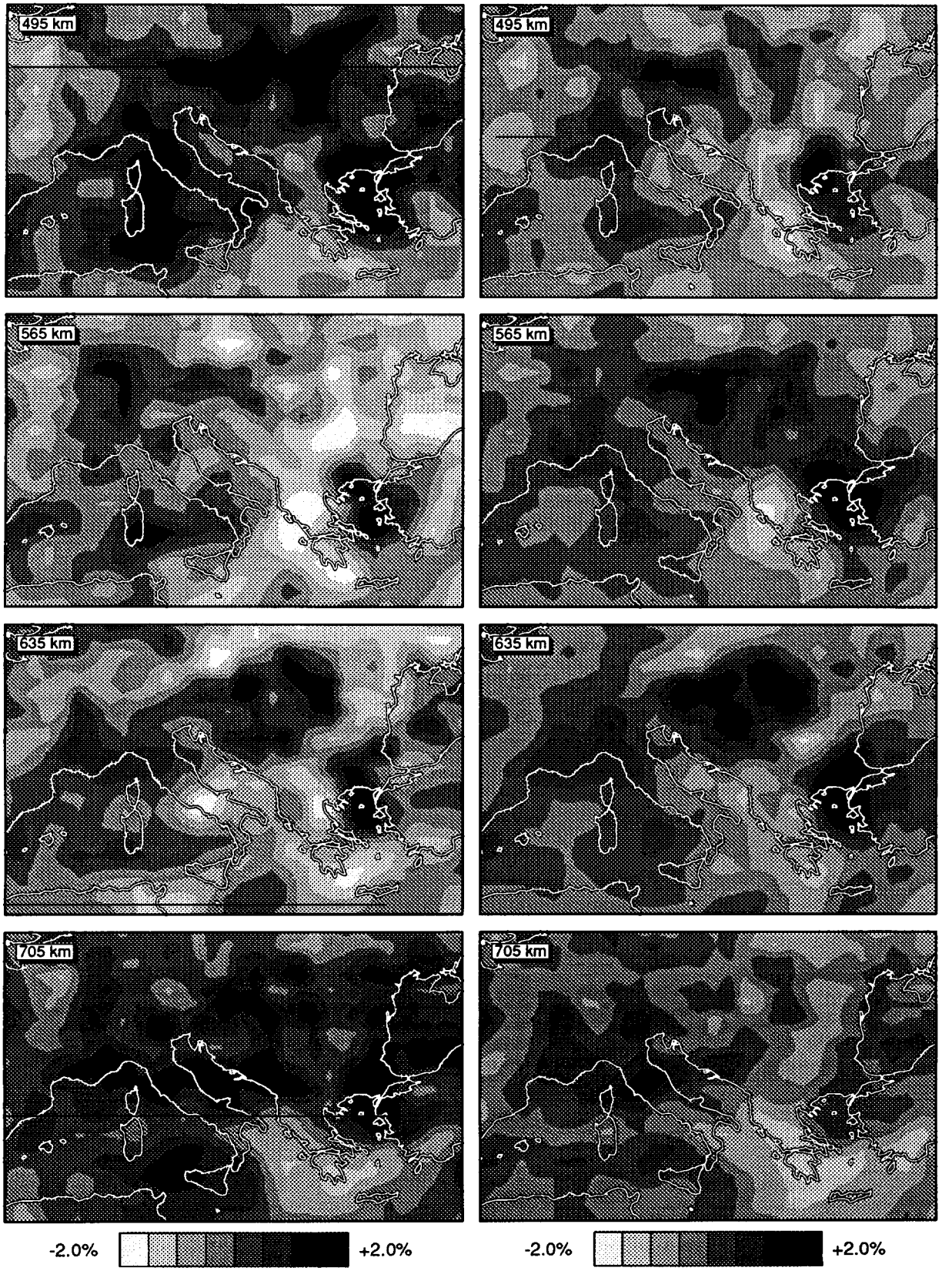

left. The slice for the SPT result is taken along the straight line in the map on the right. In general, these two profiles are slightly different because the orientations of the slices are determined by where the maxima and minima are found in the HMT model, and where the spikes are located in the SPT model, respectively. In the panels for hit count and sensitivity results, an additional contour is plotted for reference (the thick white line with a black boundary); this represents the contour of 0.2% anomaly in EUR89B. For the hit count and HMT result this contour can be compared directly with the panel for EUR89B. In the SPT result the 0.2% contour belongs to EUR89B along the slice for which the SPT, result is computed.

The first eight slices are taken along directions shared by most of the ray paths, i.e. slices connecting major source and receiver regions. The first four slices (Figs. B1–B4) have a roughly NW–SE orientation, in line with stations in central and NW Europe and with earthquakes in SE Europe (the Aegean region). The sections shown in Figs. B5–B8 intersect the Aegean region with azimuths directed to Circumpacific events. The last slice is taken roughly along the European Geotraverse (Blundell et al., 1992).

In Figs. B1–B4 high spatial resolution is found in the upper 170 km (in the high hit count regions). Below that depth and down to approximately 400 km lack of vertical resolution is clearly visible in all the sections. This occurs because many rays are able to avoid the low-velocity zone in reference model PM2 and sampling by nearly vertically incident rays is dominant. The undersampling of this depth range is also visible in the hit count in the center of the panels in Figs. B2, B3 and B4. Specifically, this is where we find the lowest spatial resolution, similar to our observations for the map view images. It is important to note that the potential to resolve heterogeneity in lateral directions is high; there is hardly any smearing of spike anomalies in the lateral sense. In the central part of the panels and below 400 km the spike response improves considerably. When moving to the NE (i.e. from Fig. B1 to Fig. B4) high resolution is also present in the lower mantle above 1200 km. An important conclusion we can draw from the SPT sections in Figs. B1–B4 is that no significant smearing of anomalies occurs along ray paths connecting sources in the Aegean region and stations in NW Europe.

Similar observations can be made from the HMT result, but in this case for the detectability of larger-scale anomalies in the mantle. Poor depth resolution is expressed by the smeared harmonic patterns. Good lateral resolution can be derived from the fact that in the lateral sense the harmonic amplitude variation is imaged fairly well. The HMT result is difficult to interpret because a small lack of vertical resolution will smear the subtle pattern variation significantly. An interesting difference between the SPT and the HMT results can be observed to the left and right in most sections. Although the spatial resolution is poor, high amplitudes are recovered in the HMT result but no significant response is found for the spike result. This indicates that if anomalies existed in the mantle of large spatial extent below NW Europe or below the Eastern Mediterranean, then these anomalies would probably be detected but not well resolved. In EUR89B not much is mapped below the indicated regions, suggesting that at least large-scale anomalies do not exist in those poorly resolved regions of the mantle.

We have refrained so far from giving interpretations of the EUR89B result. For our discussion of the next four sections (Figs. B5–B8) it is, however, interesting to depart from that. The anomaly dominating in all four sections is a dipping high-velocity body which is intersected at various angles. A similar anomaly has also been imaged in the earlier upper-mantle study (only to a depth of 600 km) (Spakman, 1988, 1991), and is interpreted as the image of the African plate

Fig. 9. A comparison between models EUR89A (left panels) and EUR89B (right panels) for the the central part of the model and at depths between 50 and 705 km. The results for EUR89A are plotted relative to the JB model and those for EUR89B relative to the PM2 model (Fig. 6) (see section 6.3).

subducting below the Aegean (Spakman et al., 1988). Spakman and Nolet (1988) have discussed in detail the resolution of this Aegean slab using sensitivity tests similar to those described in this study, and arrived at the conclusion that the slab structure was likely to be resolved and was not due to smearing of a spatially small slab anomaly along down-dip oriented ray paths. The slab anomaly we detect in this study is similar in shape in the upper mantle to that found earlier and it is mapped at exactly the same location. However, here we also find a distinct lower-mantle continuation. As mentioned in the Introduction, one of the aims of the present study was to investigate the possible dependence of deep-reaching anomalies on the natural limitations imposed by the upper-mantle cell model used in the earlier study. The anomaly associated with Aegean subduction is the most prominent of these deep-reaching velocity patterns. Using the sensitivity tests we can address the reliability of the slab anomaly.

First, we remark that the sections in Figs. B7 and B8 are more or less oriented in the dip direction of the strongly curved Hellenic subduction zone. Figure B6 shows an oblique intersection at an angle of about 50° with the dip direction, and Fig. B5 shows a section taken along an azimuth of about 10–15° west of the dip direction. In all sections we can make similar observations for the spatial resolution as we did for the sections shown in Figs. B1–B4. For instance, we infer a high potential for imaging detail above 170 km, lack of vertical resolution between 170 and 400 km, and improving resolution below 400 km. In the lower mantle the synthetic patterns are recovered very well. That smearing of the slab anomaly in the dip direction is a possibility to consider follows from the hit count plots, from which we can infer that the highest hit count roughly follows the geometry of teleseismic ray paths. It should be noted, however, that we have taken the sections at distinctly different azimuths and hence we also infer that the sampling by teleseismic rays occurs in a large range in azimuth (see section 2, and Fig. 2), which may also explain the high spatial resolution obtained in the lower mantle. Many of the rays sampling the Aegean slab originate at events located in Circumpacific subduction zones and may already have acquired a negative delay in the Circumpacific slabs. In the inversion we try to account for these delays by inverting for origin time errors associated with these events. The sensitivity results within the slab outline indicate that lack of down-dip resolution may exist, but predominantly between 170 and 400 km. However, even in this depth range individual spike responses can be detected. The HMT result convincingly shows that the sign changes in the pattern can be resolved within the slab outline, indicating that if the Aegean slab was significantly shorter this would probably be detected in the inversion.

Our conclusion from the sensitivity test results is that the deep-reaching positive anomaly associated with the Aegean subduction may be largely resolved. Obviously, we have to be careful in inferring actual resolution from sensitivity analysis (see section 5.2), and specifically in this case where we consider a very large positive anomaly that in reality, may deflect the actual ray paths towards the core of the slab anomaly. Therefore, the conclusion on the apparent deep subduction below the Aegean should be that the tomographic results are sufficiently accurate to consider the hypothesis that deep subduction has occurred below the Aegean as opposed to the possibility that the subducting slab is only penetrating to depths of a few hundred kilometers as indicated by seismicity (Fig. 10). Slab seismicity only defines the seismically active part of a slab and not its total length. Absence of seismicity below a few hundred kilometers in a deep-reaching Aegean slab may be explained by considering the force balance of subduction and the thermal structure of the slab in the land-locked basin setting of the Aegean subduction (Wortel et al., 1990).

The last section (Fig. B9) follows roughly the European Geotraverse profile. From the hit count pattern, we infer that in this case also illumination from teleseismic rays dominates. The sensitivity tests show high resolution in the upper 150 km in the well-sampled region (central Europe and the Alps). Below that, depth resolution is rather poor for cell-scale anomalies. From the amplitude response in the HMT result we infer

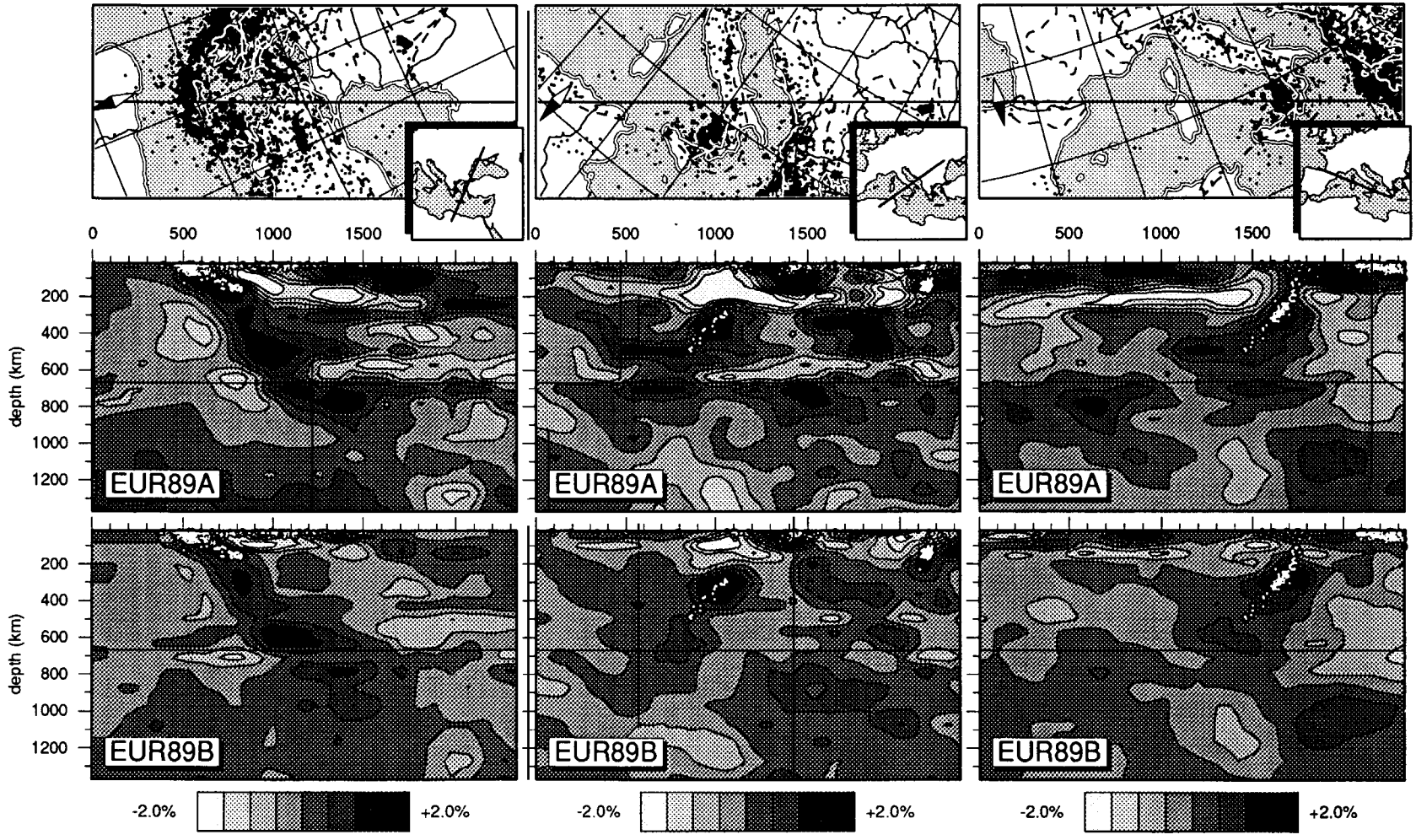

Fig. 10. Three cross-sections to illustrate reference model effects. Left: Aegean; center: central Mediterranean; right: Western Mediterranean. Dots in the cross-section denote hypocenters located within 50 km of the plane of cross-section (see section 6.3).

that large-scale (a few hundreds of kilometers) anomalies in the mantle below northern Germany would be detectable if present. The only anomalies in EUR89B of appreciable amplitude are found below the Alps and Scandinavia. In the latter case, the positive anomalies would correlate with the cold Precambrian root below Scandinavia. The exact extent of these larger-scale anomalies is not well resolved.

6.3. *Reference model effects*

The influence of the reference model in mantle tomography has been studied by Van der Hilst and Spakman (1989), Zielhuis et al. (1989) and Van der Hilst et al. (1991, 1993). Here we will briefly address the effect of the reference model on imaging heterogeneity in the European–Mediterranean mantle. This discussion is also prompted by the fact that the EUR89B inversion result only provides a slightly better data fit than the EUR89A results. Hence, discriminating between the two 3-D models on account of data fit alone is less warranted than, for instance, in the case of Van der Hilst et al. (1991, 1993) for the NW Pacific mantle.

In Figs. 9(a–c) the results for EUR89A and EUR89B are presented for the central part of the cell model and to a depth of 700 km. The column layout of these figures makes direct comparison easy. In the EUR89A result we find, on average, high velocities in the top layers, followed by a distinct (heterogeneous) low-velocity zone at depths between 145 and 247 km. No clear indication of the presence of a 400 km discontinuity is found in the tomographic results. The 670 km discontinuity is, however, clearly 'visible': in the two layers above the 670 km discontinuity negative anomalies dominate, and directly below the 670 km boundary we find an average increase in P velocity. This is precisely what we would expect (see Fig. 6). Model EUR89B exhibits much more balanced heterogeneity with depth and we can conclude that the reference model effects visible in EUR89A have effectively been accounted for in EUR89B as a result of the change in reference model and associated reference ray paths.

In cross-section, reference model anomalies can be illustrated even better. Three sections are plotted in Fig. 10. For the same sections both the EUR89A and EUR89B results are plotted. High velocities in the lithosphere, low velocities at depths around 200 km and the velocity jump across the 670 km discontinuity are visible in all three sections. In the Aegean cross-section (left panels) the fact that we image the 670 km discontinuity so clearly in EUR89A again shows the high resolution we may have at this depth. It should be noted that low velocities just above 670 km and adjacent to the slab nearly cut the slab anomaly in two. To the left of the slab anomaly we do not see any indication of the 670 km discontinuity, presumably because of poor resolution.

In the EUR89B sections the reference model bias is not present, as these effects are now properly accounted for in the reference model. The layer just below the 670 km boundary is, however, on average slightly positive, indicating that the jump in velocity in PM2 may be somewhat too large. On account of these results, i.e EUR89B vs. EUR89A, we believe that using model PM2 as a reference model leads to a better linearizable tomographic problem in which reference rays provide a better approximation for actual rays.

The PM2 ray paths provide a different illumination of the mantle than JB ray paths, and it is interesting to investigate the effect of this change on the 3-D heterogeneity imaged. Although a close comparison of the left and right panels in Figs. 9(a–c) reveals much difference in heterogeneity detail on a small scale, the larger-scale differences or correspondences are easily depicted. As PM2 rays bottom at shallower depth in the lithosphere (Fig. 9(a)) we can find the patterns in EUR89A for depths 51–195 km in EUR89B at depths 51–145 km, i.e. the depth 195 km of EUR89A is comparable with the depth 145 km in EUR89B. Hence, the larger-scale patterns are shifted upward as a result of the change in reference model. At 195 km we are in the heart of the low-velocity zone in both EUR89B and the PM2 model. This upward shift in anomaly pattern seems consistent up to the 670 km boundary.

The significance of this upward shift in anomaly

patterns can be illustrated in a brief comparison with results from surface-wave studies, for instance for the upper mantle below western Italy. There we find positive velocity anomalies at shallower depths (145 km) in EUR89B than in EUR89A. Also, in surface wave studies an increase in S-wave velocity is found at depths of about 150 km (Panza, 1984; Snieder, 1988; Zielhuis, 1992) and at the same location. As the method and data for surface-wave tomography are completely independent and different from those in P travel-time tomography, this correspondence adds to the reliability of both types of results obtained.

Finally, independent of the problem of whether or not the change of reference model has led to a more accurate imaging of actual mantle heterogeneity, we can also conclude from the comparison of EUR89A with EUR89B that the larger-scale patterns found in the mantle are relatively stable with respect to the nonlinear effects associated with a change in reference model. This observation contributes to the actual existence of 3-D heterogeneity associated with the patterns imaged.

7. Larger-scale aspects of the mapped heterogeneity

The anomaly patterns imaged in EUR89B display considerable detail which, especially in the upper layers, may be resolved well according to the sensitivity tests. Although the images in the upper layers may at first sight seem somewhat random, detail of the order of the cell size (0.8°, or 1/62 of the length of a panel in Appendix A) seems resolvable in the central area. Below the lithosphere, anomaly patterns vary on distances extending over cells. These anomalies may be resolved reasonably well, i.e. the anomalies are somewhat blurred images of existing heterogeneity which is presumably located where we find the anomaly patterns in EUR89B. We cannot expect to resolve the detailed variation of amplitudes within anomalies, nor are amplitudes resolved well. Amplitudes are on average underestimated except, perhaps, where we find the highest spatial resolution in the sensitivity tests.

In this section we will address the larger-scale anomalies found for the upper mantle in the Mediterranean. Before doing so, it is interesting to compare the results obtained with other tomographic results, which may provide additional credibility to the anomalies imaged in EUR89A and EUR89B.

7.1. Comparison with results from other large-scale mantle studies

We primarily restrict this discussion to the large-scale mappings of S-wave velocity because these result from completely independent methods and data. The first European–Mediterranean maps of S-velocity heterogeneity for the crust and uppermost mantle were determined by Panza et al. (1980), Calcagnile and Panza (1981), Calcagnile et al. (1982), Mueller and Panza (1984) and Panza (1984) from an analysis of surface waves with a method called phase velocity regionalization. The results obtained provided a new and clarifying view on the structure of the lithosphere–asthenosphere system to depths of about 200 km. On a larger scale, a reasonable to good correlation exists between these results and the patterns imaged now by P travel-time tomography. For instance, high velocities are found in the lithosphere of NW Europe, low velocities in the asthenosphere north of the Alps, and higher velocities in the lithosphere of the Adriatic plate. Also, a very good correspondence exists with the low velocity anomaly imaged for the crust and lithosphere of central–western Italy. Specifically, Panza and Mueller (1979), Mueller and Panza (1984) and Panza (1984) identified a number of deep-reaching high-velocity anomalies denoted as 'lithospheric roots', located below the Alps, the central–northern Apennines and below southern Spain. The root below the Alps was also detected by Babuska et al. (1984, 1990) from an analysis of teleseismic P residuals. Below these three regions high P-wave velocities are also found in EUR89A and EUR89B.

Snieder (1988) applied surface-wave tomography using waveforms of direct and scattered sur-

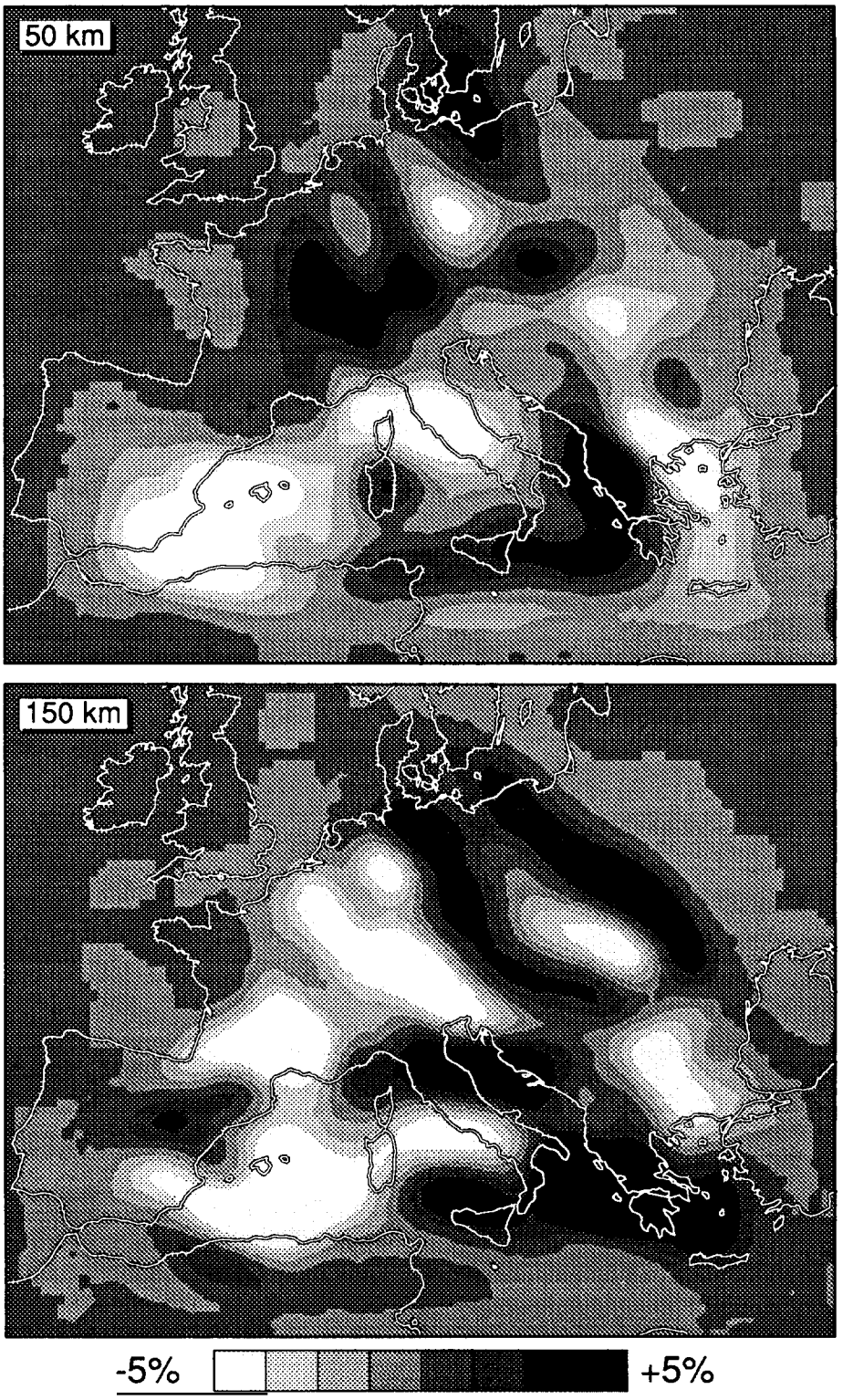
50 km
150 km
-5%
+5%

face waves to map the S-wave velocity of the lithosphere and uppermost mantle in a two-layer model with 100 km layer thickness. His results are shown in Fig. 11. It should be noted that Snieder's results were obtained by inverting waveforms from only a few tens of seismograms from regional events recorded by the NARS array (Nolet and Vlaar, 1982; Dost, 1987). In spite of the few data used for the inversion, implicitly determining lack of lateral resolution, the S anomalies mapped show (on a large-scale) an interesting correspondence with EUR89B and the S-wave results of Panza et al. (1980) and Calcagnile et al. (1982). Examples are the high velocities below the Hellenic Arc and the Calabrian Arc, the low velocities in the lithosphere below central Italy and in the asthenosphere north of the Alps, and the higher velocities in the lithosphere of NW Europe. The low velocities below the Western Mediterranean correspond well to those mapped by Panza et al. (1980), but are not very well represented in EUR89B; this may be due to the poor sampling of the upper 150–200 km. Low-velocity heterogeneity is more obvious in EUR89A (see Fig. 9a) and less pronounced in EUR89B, as in the latter heterogeneities are imaged relative to a low-velocity zone in reference model PM2. Interestingly, in the second layer of Snieder's results the high-velocity anomaly found in the upper right may be the image of the boundary between the Russian Platform and the younger western European lithosphere, a boundary usually denoted as the Tornquist–Teisseyre Zone. This velocity contrast was also imaged, although poorly resolved in depth, in the earlier P delay-time study (Spakman, 1991) and in EUR89A and EUR89B.

Recently, Zielhuis (1992) obtained a 3-D mapping of S-wave velocities for the lithosphere and upper mantle using the technique of partitioned waveform inversion (Nolet, 1990). With data from only a few hundred seismograms, Zielhuis imaged S-wave velocity patterns in remarkable detail in the upper few hundred kilometers. In Fig. 12 results are shown for two depths, 80 and 200 km. If we compare the S results at the 80 km level with the results obtained in EUR89B at 95 km and 145 km, a reasonably good correlation can be observed between the patterns of anomalies. The image of the Tornquist–Teisseyre Zone and velocity patterns in central and SE Europe correlate fairly well with EUR89B results. Specifically, the Tornquist–Teisseyre Zone and the high velocities in the lithosphere of the Russian Platform are pronounced anomalies in S-wave image and seem rather well resolved (Zielhuis, 1992). From the sensitivity tests we infer that in the EUR89B model the resolution may be sufficient only to map the jump in velocity across the Tornquist–Teisseyre Zone but insufficient to image the velocities in the lithosphere of the Russian Platform (see Figs. A3, A4, B5 and B6). In the slice at 200 km depth in Fig. 12, slightly positive anomalies are found below Italy and strong positive anomalies below the Dinaric–Hellenic zone. Both positive anomalies are also mapped at greater depth (Zielhuis, 1992). As noted above, Panza (1984) and Mueller and Panza (1984) already inferred the existence of the same positive S-velocity anomaly below central Italy between depths of 100 and about 200 km. In the results of Snieder (1988) and Zielhuis (1992), the lithosphere structure below the Alps does not exhibit a positive seismic velocity anomaly as is found in, for instance, EUR89A and EUR89B or in the S-wave results of Panza and coworkers.

The brief comparison between S and P structures imaged leads to similarities of velocity heterogeneity patterns, but also to mismatches. There are a large number of causes that may lead to different results. Notably, each tomographic method has its own problems with nonlinearity, and there are differences in the scale at which structures seem to be resolvable both in depth and lateral extent, in the quality and number of data used in the inversion, and in the dependence of S and P velocities on temperature and composition. However, we believe that the correspon-

Fig. 11. S-wave heterogeneity model obtained by Snieder (1988).

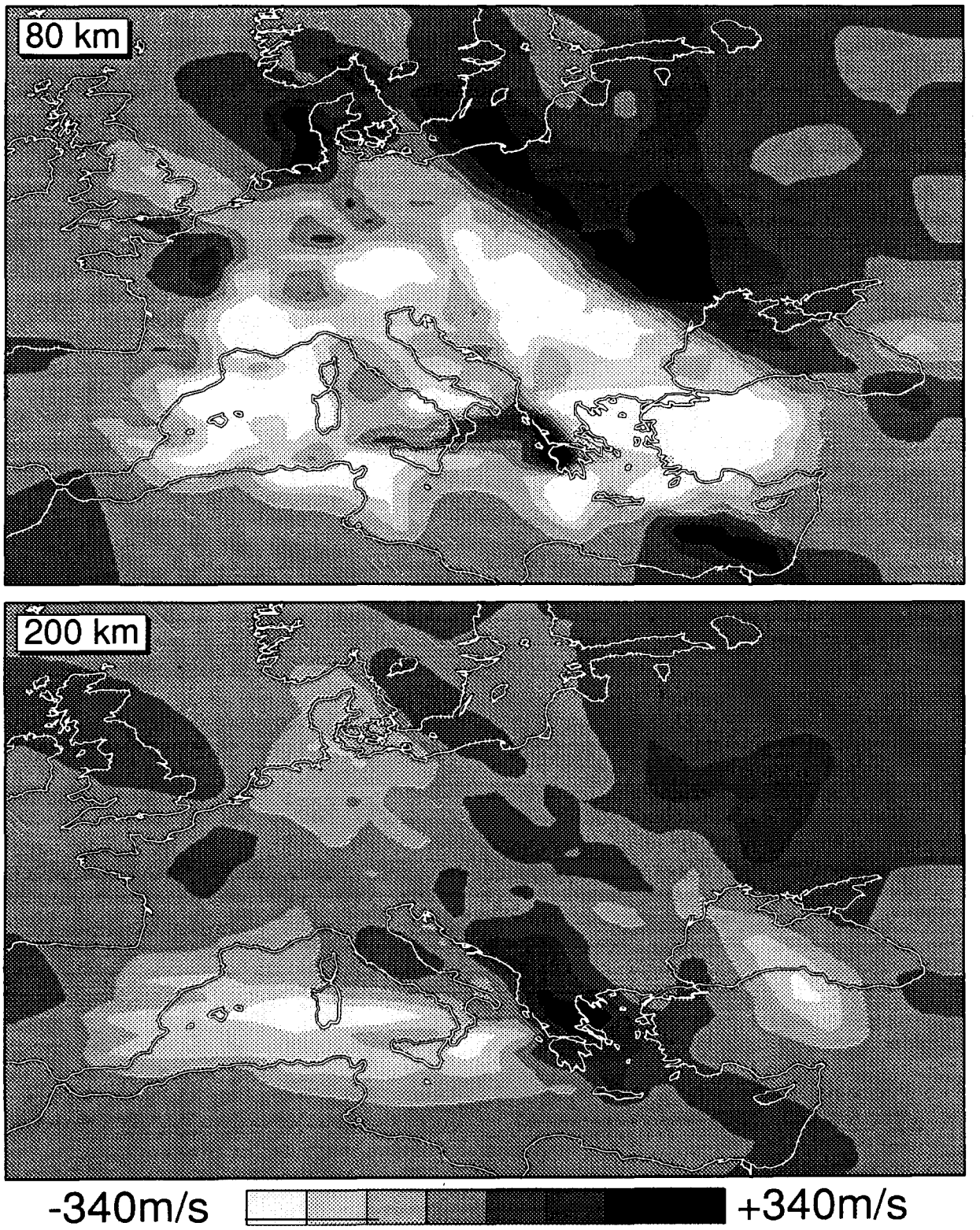
80 km
200 km
-340m/s
+340m/s

dence in pattern of major anomalies is more than a coincidence. The important inference we may draw here is that independent methods and data, and hence independent tomographic results, lead to the detection of 3-D mantle structures located below Italy and the Dinaric–Hellenic Arc that map into positive anomalies for both S and P velocity. This gives additional credibility to the actual existence of these mantle structures.

A comparison of the new results from EUR89A and EUR89B with those obtained earlier (Spakman, 1988, 1991) is also necessary. This comparison is significant because the cell models used are different; here we use smaller cells (0.8° vs. 1°) and more layers in the upper mantle (12 vs. 9), and the cell models are also oriented differently and parameterize the mantle to different depths (1400 km vs. 670 km). Furthermore, the data used in the first study stemmed primarily from regional event–station combinations and no teleseismic data were used. Figure 13 displays a part of the results obtained in that study. This model is called EUR85A. The anomaly patterns in EUR85A compare best with model EUR89A—as both are determined using ISC data and the JB reference model—and display similar reference model artifacts. The strong resemblance between EUR85A and EUR89A leads to the important conclusion that anomalies imaged in the upper mantle are largely independent of velocity structures in the lower mantle.

Lastly, Granet and Trampert (1989) imaged the mantle below Europe and the Mediterranean to a depth of 1200 km. They used only 10890 P delays and 1120 large blocks (3° × 3° and six cell layers), but arrived at an anomaly patterns that resemble our results well on a larger scale.

7.2. *Interpretation of larger-scale structures below the Mediterranean*

In this section we will address some of the larger-scale aspects of the patterns imaged below the Mediterranean. The interpretations given here are based on the more detailed analyses presented for model EUR85A by Spakman (1986, 1990) and Spakman et al. (1988), for the Spanish region by Blanco and Spakman (1993), and for the evolution of the Mediterranean during the Cenozoic by Wortel and Spakman (1990, 1992). Here, we are primarily interested in how the results from EUR89A and EUR89B can further support these analyses.

In all models EUR85A, EUR89A and EUR89B, the pattern of anomalies imaged below the asthenosphere is dominated by an irregular zone of positive anomalies that closely correlates with the Alpine orogenic belt in the Mediterranean. Spakman (1986, 1990) has interpreted this pattern as the mapping of subducted lithosphere associated with the destruction of parts of the Meso- or Neo-Tethys. One element that justifies this interpretation is that the positive anomalies in those regions with intermediate to deep seismicity (southern Spain, the Tyrrhenian and the Aegean) are all part of the belt of higher velocities. Clearly, this belt is of an irregular shape and is not imaged as one continuous zone, which indicates that one cannot explain the anomalous zone as being evolved from one large and simple subduction process. Furthermore, tectonic provinces, such as the Western Mediterranean basins, Apennines, Alps, Carpathians and Pannonian basin, the Dinarides, Hellenides and Eastern Mediterranean basins, all have their specific aspects of development (e.g. Dercourt et al., 1986). However, the mantle structure imaged may provide additional information which allows us to explain and correlate the tectonic evolution of these regions in space and time (Wortel and Spakman, 1990, 1992).

From a completely different angle, support for the interpretation of large-scale subduction has been provided by De Jonge et al. (1993), who predicted the velocity heterogeneity in the mantle using tectonic reconstructions of the Mediterranean by Dercourt et al. (1986) and Dewey et al. (1989). The tectonic reconstructions were primar-

Fig. 12. Sections through the S-wave heterogeneity obtained by Zielhuis (1992) at depths of 80 and 200 km.

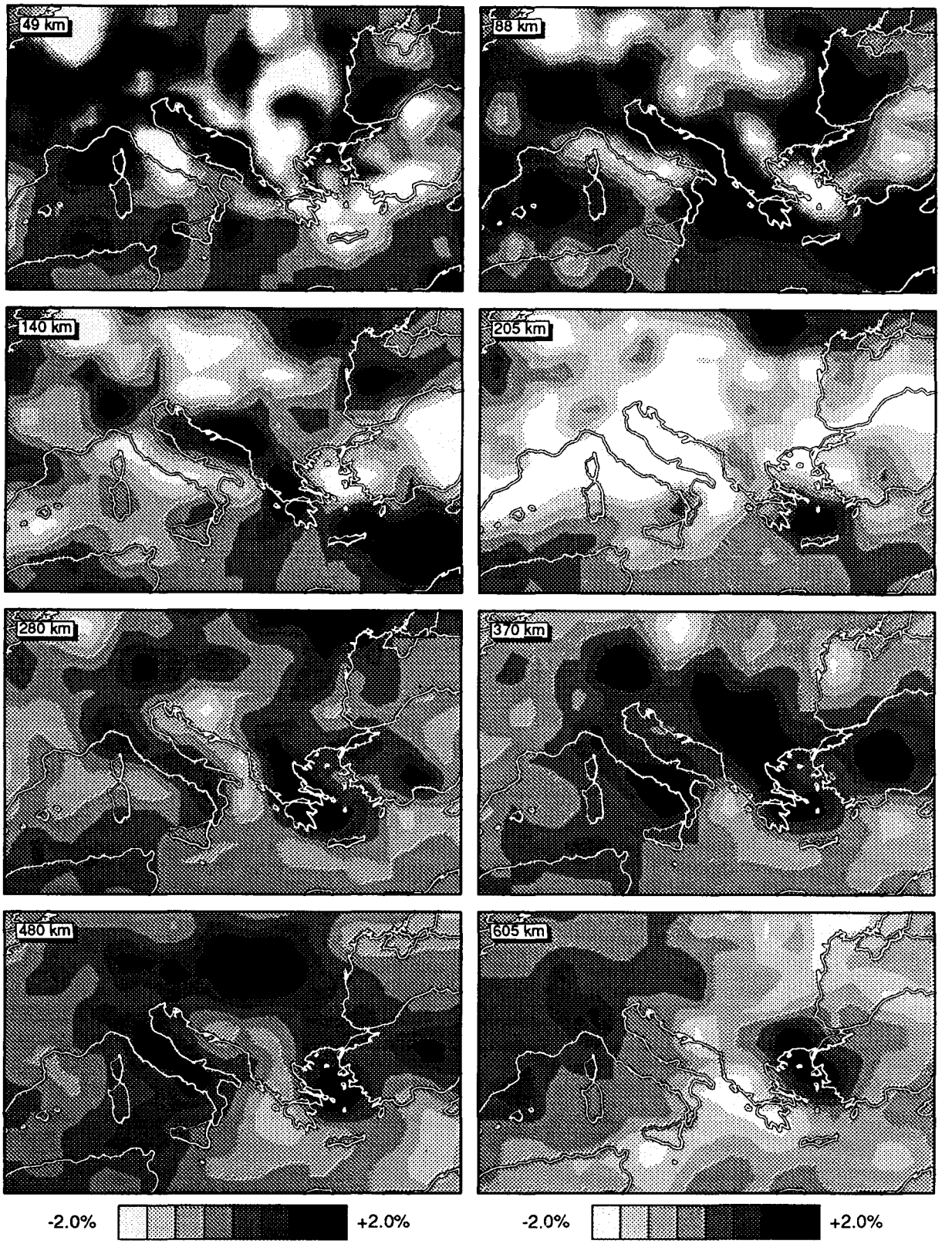
49 km
88 km
140 km
205 km
280 km
370 km
480 km
605 km
-2.0%
+2.0%
-2.0%
+2.0%

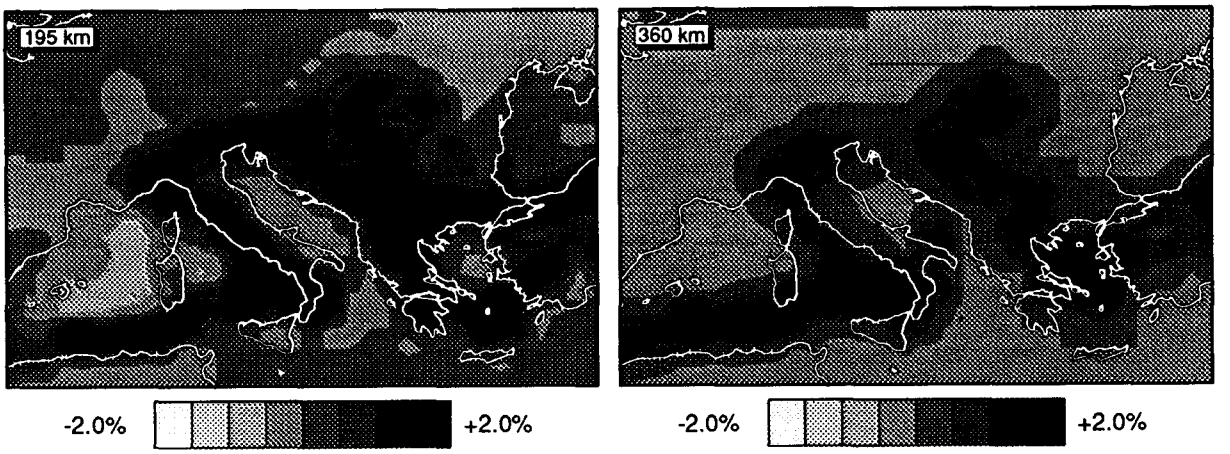

Fig. 14. Two depth sections, at 195 km and 360 km, through predicted mantle model DRW of De Jonge et al. (1993).

ily based on geophysical and geological data obtained for the near surface and crust, and not the seismological data used in this study. First, De Jonge et al. (1993) predicted temperature anomalies from an interpretation of the tectonic reconstructions, and then they converted the temperature anomalies into P-wave velocity heterogeneity. For a correct comparison with the tomographic results, the thermal mantle structure needs to be projected on the cell model used for tomography. For two depths, 195 and 360 km, the results of De Jonge et al. are displayed in Fig. 14 for a model denoted DRW (compare with Fig. 9). The high-velocity structures are predicted from subduction that occurred mainly during the Cenozoic. The correlation with the large-scale patterns in EUR89B is striking. Obviously, there are also differences, for instance, in amplitudes between the predicted anomalies and anomalies determined from inversion (e.g. the North African margin). The latter depend on, for example, ray sampling, resolution and convergence of the least-squares solution, whereas the mantle prediction does not. Nevertheless, this first-order correlation supports the interpretation of large-scale subduction in the Mediterranean area.

Spakman et al. (1988) discussed the significance of deep subduction below the Aegean for the tectonic development of the region, and arrived at the conclusion that the minimum duration of subduction (imaged to 600 km in that study) was at least 26 m.y. On account of alternative scenarios for the convergence of the African and European plates, this time span can be enlarged to 40 m.y. In this paper, we find in EUR89A and EUR89B subduction below the Aegean to depths of at least 670 km but possibly down to 800–900 km. De Jonge et al. (1993) predicted a thermal anomaly associated with Aegean subduction to a depth of 800 km. If the Aegean subduction relates to the destruction of one oceanic basin (the Eastern Mediterranean part of the Tethys ocean) then the duration of subduction may possibly be extended to even longer than 40 m.y.

Below southern Spain (the Betic–Alboran region) a large positive anomaly is located between 150 and 670 km. The sensitivity tests indicate that this mantle region is on average poorly resolved. Blanco and Spakman (1993) performed a detailed study of this anomaly in a tomographic study of the mantle below the Iberian Peninsula, and concluded (after several tests with sub-sets of data and with various synthetic models) that this anomaly results from a high-velocity body situated in the upper mantle below the Betic–Al-

Fig. 13. Part of model EUR85A obtained by Spakman (1988, 1991).

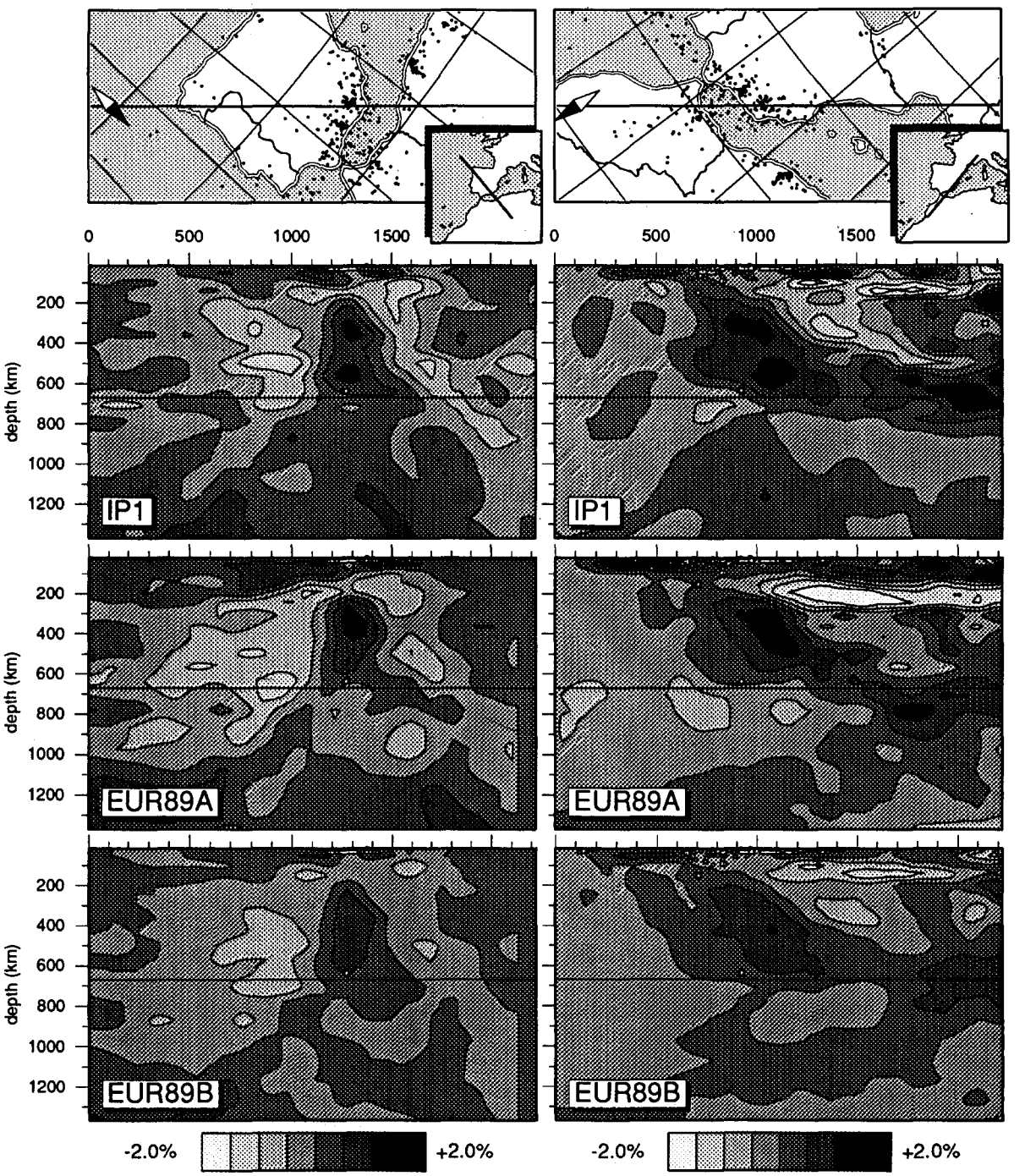

Fig. 15. Comparison of results for the slab anomaly below southern Spain along two cross-sections. IP1 is the model determined by Blanco and Spakman (1993). The positive anomaly in the upper mantle is interpreted as an image of subducted lithosphere. Panels to the left give a section perpendicular to the assumed dip of the slab anomaly. Panels to the right give a cross-section along the assumed strike of the slab anomaly. The white dot at 640 km denotes the hypocenters of the deep seismicity below southern Spain.

boran region. This anomaly is interpreted as the image of a subducted slab. A tentative timing for subduction can be obtained by placing the Betic slab into the tectonic scenario of Platt and Vissers (1989) for the Betic–Alboran region, which would lead to a last phase of subduction during the Oligocene (Blanco and Spakman, 1993). Figure 15 allows a comparison between model IP1 of Blanco and Spakman (1993) and our results (model IP1 is determined relative to our PM2 reference model). The left column of panels is taken along a section along the assumed dip direction of the slab (either NW or SE) and the right column of panels along the assumed strike of the subduction zone (roughly SW–NE). It should be noted that the deep events at 640 km (e.g. Buforn et al., 1991b) provide support for the interpretation of lithosphere subduction. Mueller and Panza (1984) and Panza (1984) (for a review, see Panza and Suhadolc (1990)) discussed also a higher-velocity root below southern Spain which exhibits less pronounced S-wave velocity differences with the surrounding lithosphere than the roots below the Alps and central–northern Apennines. The location of the root below southern Spain is somewhat westward with respect to the high-velocity body found in this study. Possibly the positive S-wave anomaly below southern Spain can be explained by the recent subduction related to the convergence of Africa and Iberia as evidenced by intermediate seismicity (Buforn et al., 1991a).

Under Italy, the depth below which the subducted lithosphere is found in EUR85A and EUR89A is about 200–250 km. In model EUR89B, however, the first appearance of positive anomalies is found at shallower depth below the central–northern Apennines, in the layer centered about 145 km (e.g. Fig. 9(a)). This anomaly correlates reasonably well with the results of Panza (1984), Mueller and Panza (1984) and Zielhuis (1992). Actually, the small positive anomaly visible in EUR89B at 145 km corresponds exactly with the location of the high-velocity anomaly of Panza (1984) and Mueller and Panza (1984). Panza (1984) and Panza and Suhadolc (1990) associated this root with subduction of presumably continental-type lithosphere. Using teleseismic tomography, Amato et al. (1993) also mapped a positive velocity anomaly in the mantle below the Apennines reaching lithospheric depths, which they too linked to subducted lithosphere. In their analysis, Amato et al. (1993) used very accurately determined arrivals from teleseismic events recorded by Italian station networks.

To illustrate this complex mantle region in more detail, a cross-section perpendicular to the apparent strike of the positive anomaly below the Apennines is shown in Fig. 16. The cross-section is taken through the core of the anomaly's most shallow part, in the layer at 145 km. For the same cross-section four panels are shown computed from models EUR89A and EUR89B, the model of Zielhuis (1992), labeled PWI here, and the mantle prediction model DRW of De Jonge et al. (1993). All four panels show positive velocity anomalies below the Apennines and below the Dinarides, illustrating the existence of subducted material east and west of the Adriatic micro-plate. The lithosphere of the Adriatic plate is visible as the positive anomaly in the center of the panels computed from EUR89A and EUR89B. In the PWI result only low velocities are found for the Adriatic plate, and in the DRW result the Adriatic plate is not visible because this flat-lying plate is not modeled as being thermally anomalous. At present, the Adriatic plate is still underthrusting the Apennines, as was shown in a careful analysis of intermediate seismicity to depths of 90 km by Selvaggi and Amato (1992). The events studied by Selvaggi and Amato would exactly plot in the EUR89B panel on the western limit of the Adriatic lithosphere below the Apennines.

In the panels for EUR89A and EUR89B, and to some extent for PWI, there is no connection between the Adriatic plate and the subducted lithosphere present below either side. This pattern, with lower velocities separating the lithosphere at the surface from subducted lithosphere at larger depth, is imaged below entire Italy and parts of the Dinaric–Hellenic zone to the Peloponnese, and is interpreted as resulting from slab detachment (Spakman et al., 1988; Spakman, 1990). Slab detachment is also proposed for the Betic subduction (Blanco and Spakman, 1993,

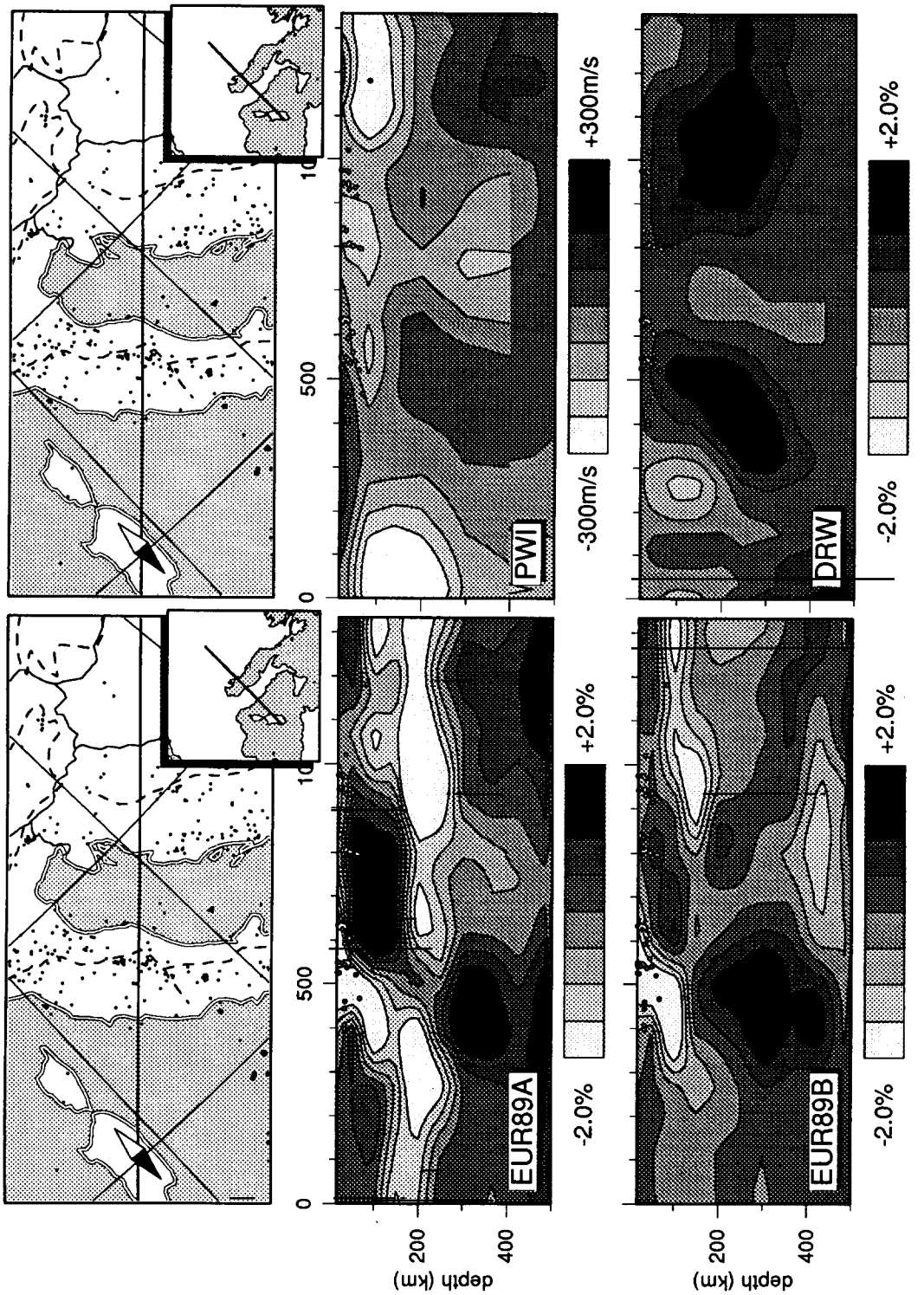

Fig. 16. Four different results along the same vertical section (to a depth of 500 km) across the high-velocity anomaly below Italy and located at the position where a distinct high-velocity anomaly in S-wave velocity was found by Panza et al. (1980), Panza (1984) and Mueller and Panza (1984). The panel PWI is computed from the S-velocity model of Zielhuis (1992), and the panel DRW is computed from the mantle prediction of De Jonge et al. (1993).

Fig. 15). Presumably, only the subducted slab below the southern Aegean is still continuous (Fig. 10). In this context, the lithospheric root of Panza (1984) can be interpreted as the upper part of the detached lithosphere found below Italy. For southern Spain we note that detachment of a piece of lithosphere has also been proposed to explain the peculiarly deep seismicity at 640 km depth (Chung and Kanamori, 1976). Detachment in this context is inferred from the facts that a seismic gap exists between 150 km and the deep events, and that the focal mechanisms of the deep events are difficult to explain in the present framework of plate convergence. This has led to the description of a decoupling between the shallow and deep events in terms of a detached piece of lithosphere of unknown size. We also note that slab detachment is not visible in the mantle predictions of De Jonge et al. (1993) because the tectonic reconstructions on which their forward modeling was based do not allow for the discrimination between attached and detached slabs. Slab detachment may explain why we find the subducted material at somewhat greater depth in the tomographic results than in the mantle prediction (De Jonge et al., 1993).

In map view, the cell layer in which slab detachment is imaged is found in EUR89B at 145 km depth (see Figs. 9 and A4). Below the Dinaric–Hellenic zone we find lower velocities in this layer, whereas higher velocities prevail in both adjacent layers. In EUR89A we find slab detachment at greater depth (panels 195 km and 247 km); this is a result of the difference in reference models. Below western Italy we find low velocities from the crust down to the detached lithosphere. The detached lithosphere has presumably been attached to the Adriatic plate and is subducted in a W–NW direction below Italy. This is in accordance with current views on the creation of the Western Mediterranean basin (e.g. Dewey et al., 1989; Panza and Suhadolc, 1990). Lastly, we note that the large zone of low velocities below NW Italy can be associated with the asthenospheric wedge which has developed above the subducting plate.

The interpretation of large-scale subduction below the Alpine belt combined with the process of slab detachment forms the basis of a hypothesis for the large-scale dynamic evolution of the Mediterranean during the Cenozoic (Wortel and Spakman, 1990, 1992). In this hypothesis, the process of lateral (along-strike) migration of slab detachment plays a key role. In the model proposed by Wortel and Spakman (1992), the Betic slab, the Tyrrhenian slab and the subducted lithosphere below Italy are all remnants of one oceanic basin that was subducting during the early Cenozoic below the eastern Iberian margin. This early subduction zone is assumed to have a roughly SW–NE strike, i.e. it was aligned from southern Spain to the Alps before the creation of the present Western Mediterranean basins. By some mechanism, slab detachment is assumed to be triggered in the vicinity of the Alps. Once triggered, slab detachment becomes a self-perpetuating process that migrates laterally along the strike of the subduction zone. The gravitational forces acting on the subducting plate will be concentrated on the still undetached part of the slab. Slab roll-back (Elsasser, 1971), and back-arc basin formation (i.e. of the present Western Mediterranean and Tyrrhenian basins) may then result from the increasing force concentration as the detachment migrates. A mirror image of this dynamic evolution presumably occurred below SE Europe, although with a different timing (Wortel and Spakman, 1992). Also, the evolution of the Carpathian Arc and Pannonian basin can be assessed with the slab detachment hypothesis, which makes the process of lateral migration of slab detachment the unifying element for the formation and tectonic evolution of major arcs and basins in the Mediterranean region (Wortel and Spakman, 1993). The power of the dynamic model for lateral migration of slab detachment is that this process leads to predictions of geological and geophysical observables, e.g. horizontal and vertical crustal motion, state of stress, volcanism and patterns of sedimentation, and therefore the model can be tested.

7.3. Remarks on lower-mantle heterogeneity

Some of the larger-scale positive velocity anomalies in the lower mantle (Figs. A13–A20)

can be interpreted as continuations of anomalies present in the upper mantle. This is, for instance, the case for the positive anomalies below the northern Aegean (Figs. B5–B8), and below the Alps and northern Italy (Figs. B1 and B9). The clearest example is the Aegean slab (Figs. 10 and B5–B8), for which we infer continuation of the slab anomaly down to depths of 800–1000 km. Here, we are not going to dwell on the issue of sinking of subducted lithosphere into the lower mantle. For a discussion and further references on this topic, readers are referred to Van der Hilst et al. (1991, 1993). We conclude that, in view of the spatial resolution, at least below the northern Aegean, slab penetration of the lower mantle must be considered a possibility. Many of the other anomaly patterns imaged in the lower mantle remain puzzling; such features include the negative velocity anomalies appearing at depths greater than 1000 km and correlating with the Tertiary Western European rift system.

8. Discussion

Without doubt, ISC delays are noisy data, but still constitute an enormously useful data set which has been used for many tomographic studies. If one uses many data and a sensible model parametrization, and provided that the cell model is sampled well, average signals on mantle heterogeneity may be correctly filtered from the delays and projected into significant images of mantle heterogeneity. We did not perform a detailed statistical screening of the data to discriminate between valuable and useless data. We only required a minimum number of observations for events to provide some confidence in the source location. In effect, we added source and station parameters also to filter out noise from the data; the source parameters specifically, are useful in this respect (Spakman and Nolet, 1988). Spakman (1991) discussed one test in which the ISC delay times are randomly assigned to the reference ray paths by randomly permuting the delay-time vector in Eq. (5) while keeping the order of the equations fixed. The permuted data possess, of course, the same bulk statistics, such as the average and r.m.s. value. Inversion of this data set led to random and small-scale anomaly patterns with very small amplitudes of (0.2% or less). This test demonstrated that the ISC delays contain information on mantle structure and that the delays are strongly correlated with the ray paths. This test provided the only direct evidence that the mapping obtained was significant and that the data are not purely noise. Other evidence for a significant mapping, such as a good correlation with surface tectonics, or with presumably existing slabs, or heat flow, is of course welcome but can only be called circumstantial.

In using teleseismic data we have to account for the effects of lateral heterogeneity located outside the cell model. For teleseismic events we inverted for an origin time error and for teleseismic stations for a station correction. Both may also account for the average effects of mantle heterogeneity outside the cell structure. Wavefront healing may destroy an appreciable high-frequency component in the data acquired in distant heterogeneity (e.g. Circumpacific slabs). Spakman (1993) estimated that, on average (and roughly), 0.5 s of an (ISC) delay acquired in the upper mantle may have been destroyed on the wave front at 70° distance. Trying to invert for the remaining 'smooth' signal of distant heterogeneity by means of estimating station statics and origin time errors may therefore be an effective approach. In our study, the sensitivity tests demonstrate that the spatial resolution in the lower mantle is good; this prevents leaking of lower-mantle heterogeneity to shallower depths. Furthermore, the comparison between EUR85A and EUR89A indicates that upper-mantle anomalies can be imaged independently from lower-mantle anomalies.

Using an improved reference model has led to results which do not exhibit significant reference model artefacts, from which we can conclude that EUR89B is a better approximation of mantle structure than EUR89A, as the nonlinear effects associated with an improper reference model (Van der Hilst and Spakman, 1989) have been largely accounted for. In our modeling of delay times we use reference rays in the improved reference model PM2 but starting from ISC

source locations. Although we correct for the delay-time contribution associated with mislocation by inverting for source parameters, the imaging matrix is still constructed from slightly misplaced ray paths. Using data from events that are relocated first in an improved reference model would prevent this inconsistency. Engdahl and Van der Hilst (1991), Van der Hilst et al. (1991, 1993) and Van der Hilst and Engdahl (1992) performed this for tomography of the mantle below the NW Pacific, for which they used the iasp91 model as reference model. Relocating earthquakes before 3-D inversion has also other important advantages (see papers mentioned above). Alternatively, Remkes and Spakman (1993) used an iterative approach for imaging mantle heterogeneity below the same area as in this study. They also started with an improved reference model and in each iteration step estimated relocation vectors, station statics and an update of the reference model, and performed a 3-D inversion. The next iteration started from relocated sources. The preliminary results obtained are similar to those of EUR89B in larger-scale aspects.

As for many other inverse methods in geophysics, it is extremely difficult, if not impossible, to prove the significance of the results. The variance reduction is reasonable, considering the data components $\epsilon_{\approx}$ we cannot invert for, but the data fit only tells us that the 3-D result can explain the delay times better than the reference model. The sensitivity tests performed in this study are helpful in localizing potentially well-resolved, reasonably resolved, and poorly resolved anomalies. This information can also be used together with hit count patterns in learning to understand the amplitude variations in the tomographic solution, and in selecting anomaly patterns useful for interpretation. Fortunately, independent results (e.g. surface-wave analysis, waveform tomography, forward mantle predictions of mantle structure and local studies) provide additional support for the significance of the larger-scale patterns imaged. The similarity between EUR85A, EUR89A and EUR89B also confirms the actual existence of the heterogeneity imaged.

The tomographic results obtained in this study are sufficiently supported by sensitivity tests and results from independent research to allow interpretation of anomalies in a geodynamical context. Obviously, interpretation starts with the assumption that the anomalies are significant. The most useful interpretations are those that eventually lead to tectonic models that in turn provide predictions of surface observables independent of the data used here. As in any forward modeling approach, rejection of such models because of poor or wrong predictions may falsify the original interpretation of the tomographic result. In turn, this may help to increase our understanding of tomographic images.

Acknowledgments

We thank Roel Snieder, Alet Zielhuis and Marc de Jonge for permission to use figures of their results. We appreciate the thoughtful reviews provided by Sören Gregersen and Uli Achauer. Bernard Dost provided us with the computer facilities of the ORFEUS Data Center for data processing. The large computations for this research were made possible by the Academic Computer Centre Utrecht (ACCU) of the Utrecht University through free usage of a Convex 120 in 1989. Part of this research has been carried out in the framework of the Pionier project (PGS 76-144), which is supported by the Netherlands Organization for Scientific Research (NWO).

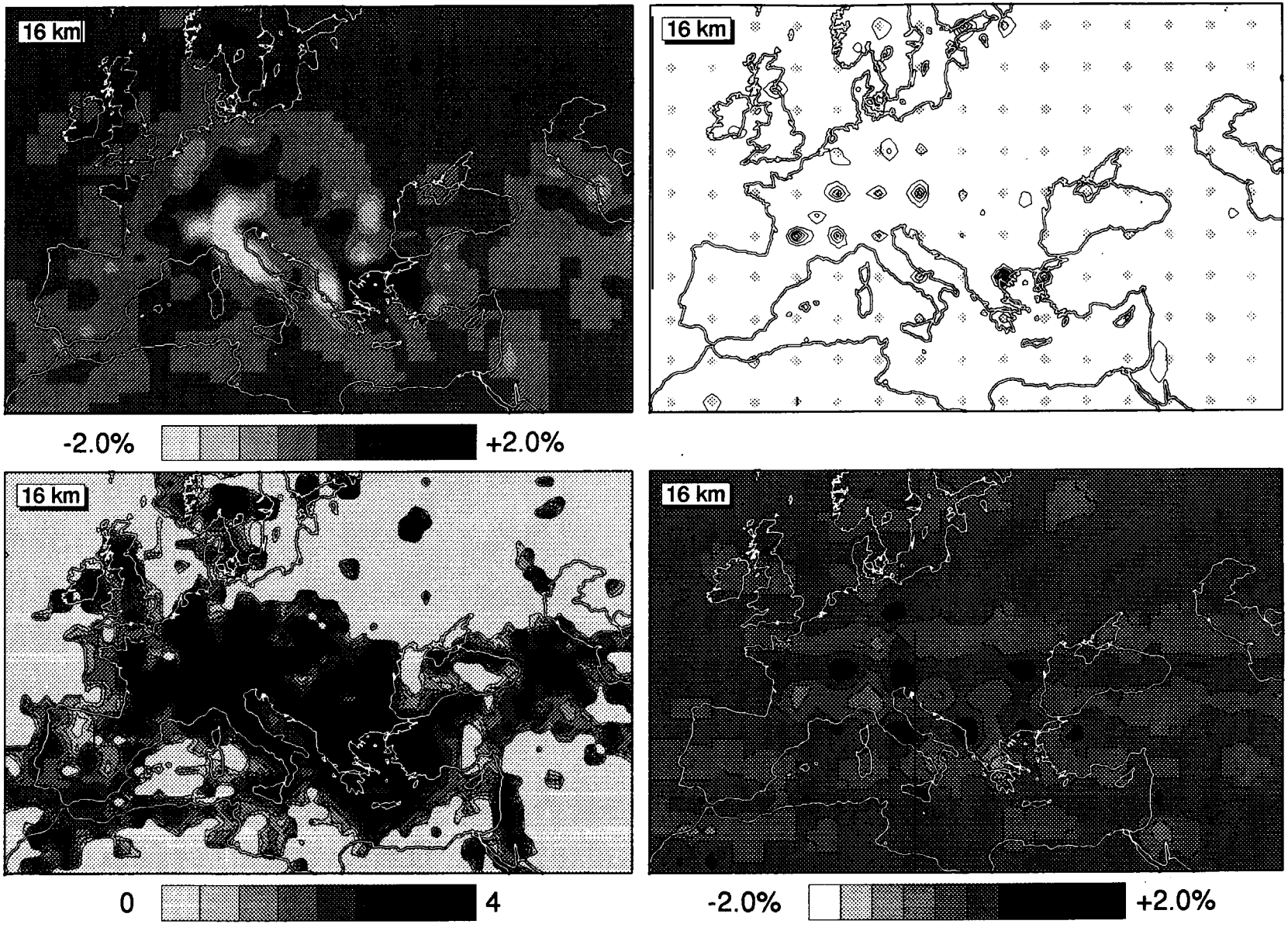

Appendix A: Fig. A1.

Model EUR89B, hit count and sensitivity test results for each cell layer. The depth indicated is the mid-point depth of each cell layer. (See section 6 for description.)

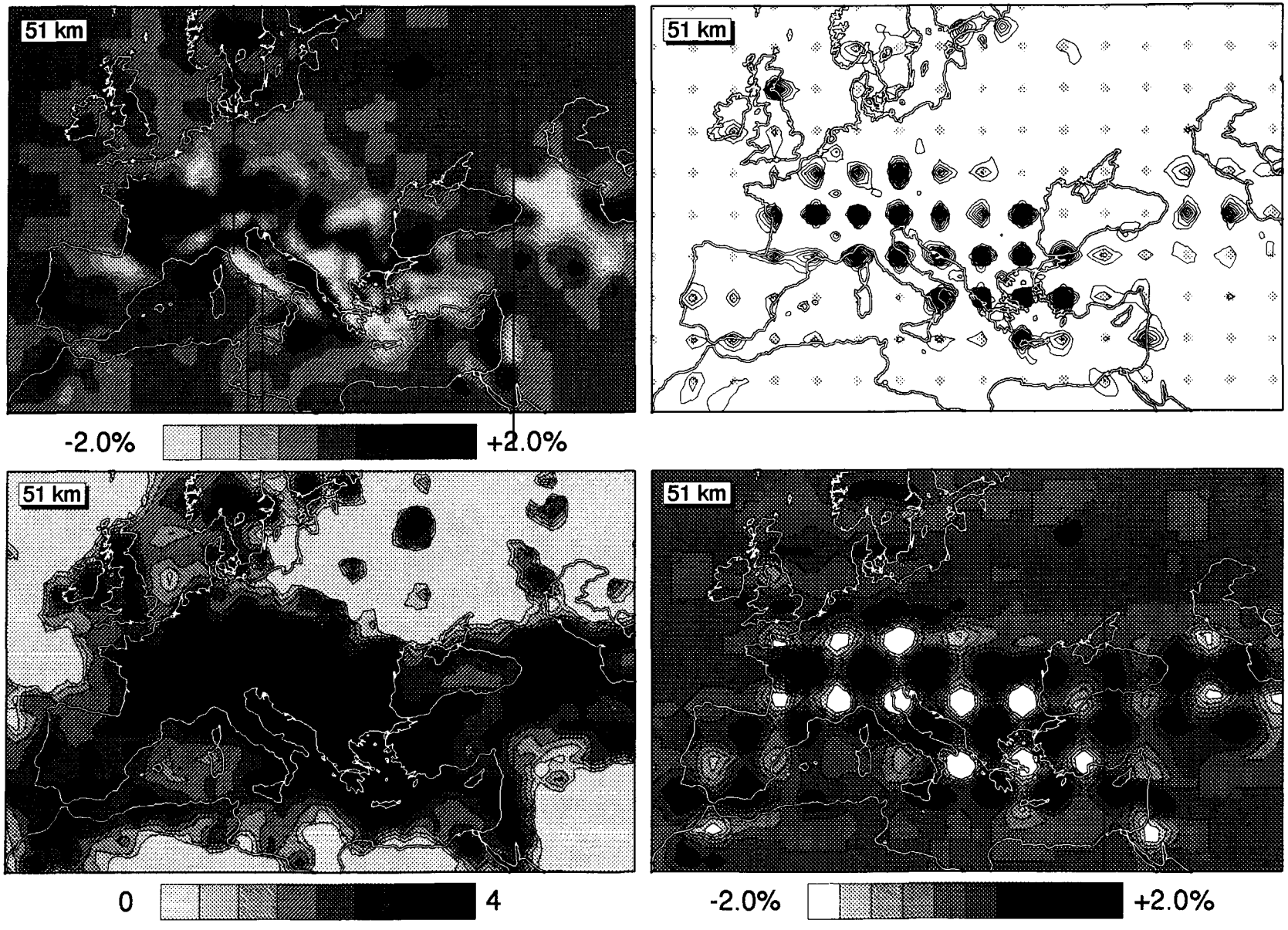

Appendix A: (continued). Fig. A2.

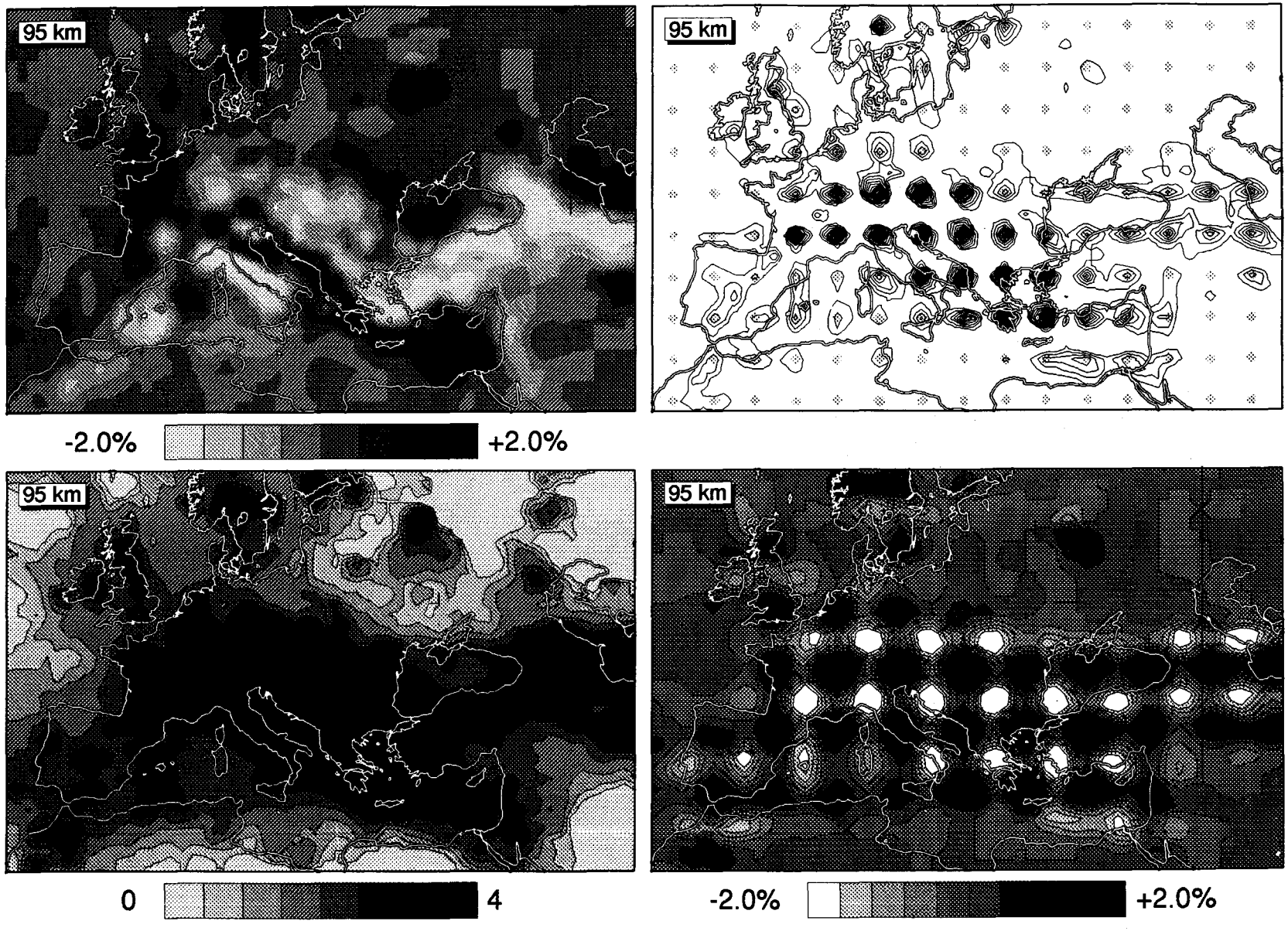

Appendix A: (continued). Fig. A3.

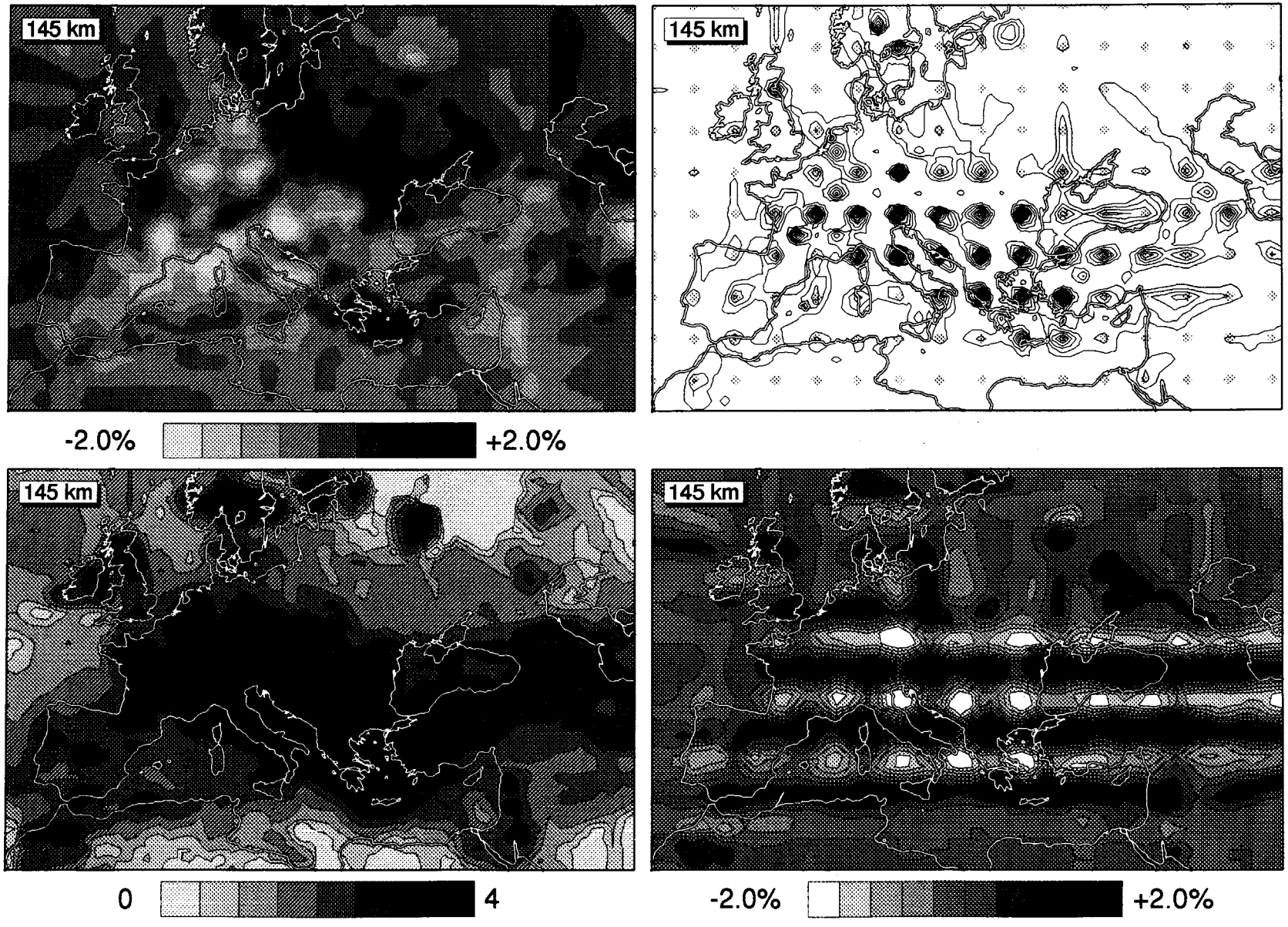

Appendix A: (continued). Fig. A4.

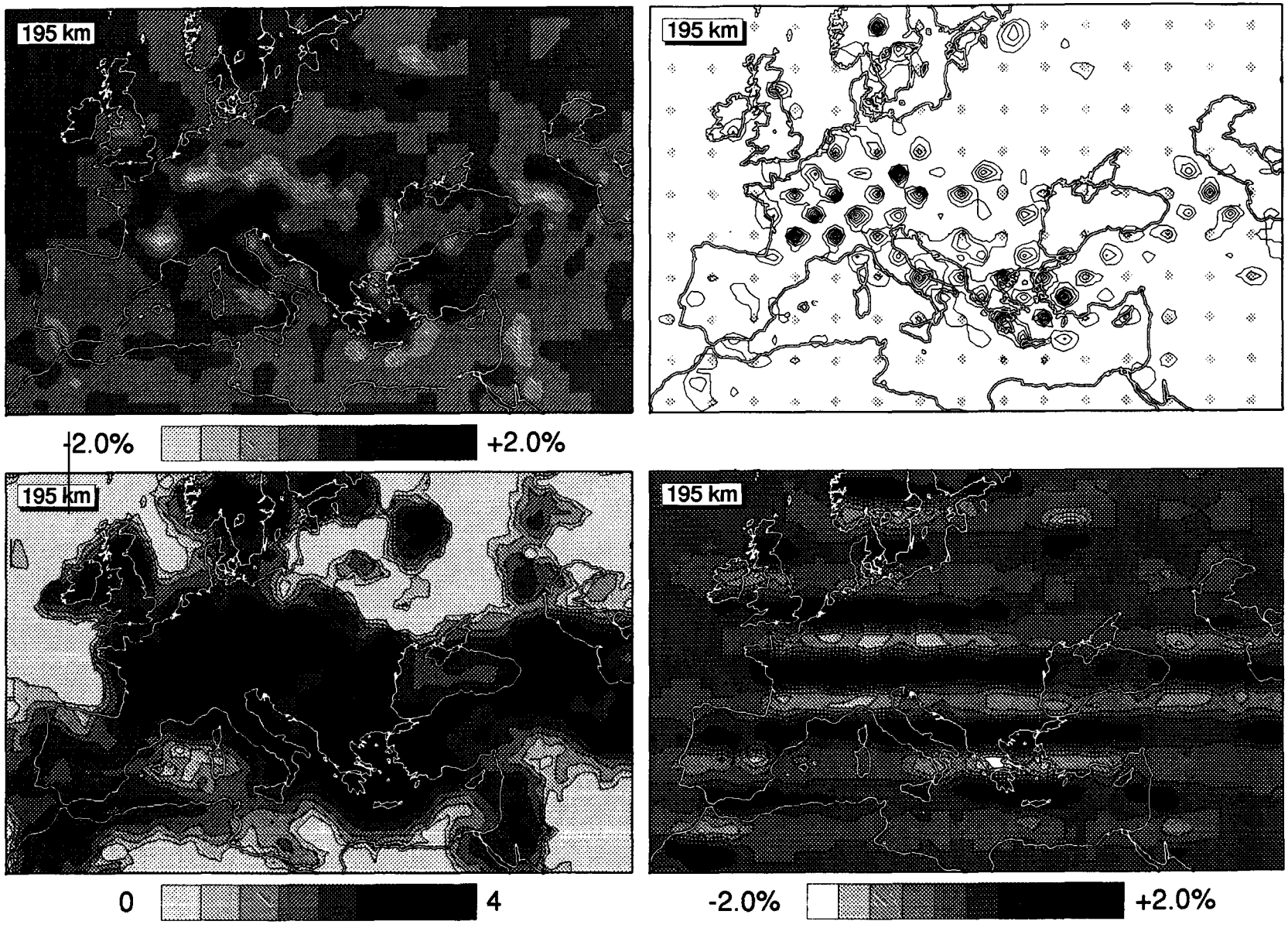

Appendix A: (continued). Fig. A5.

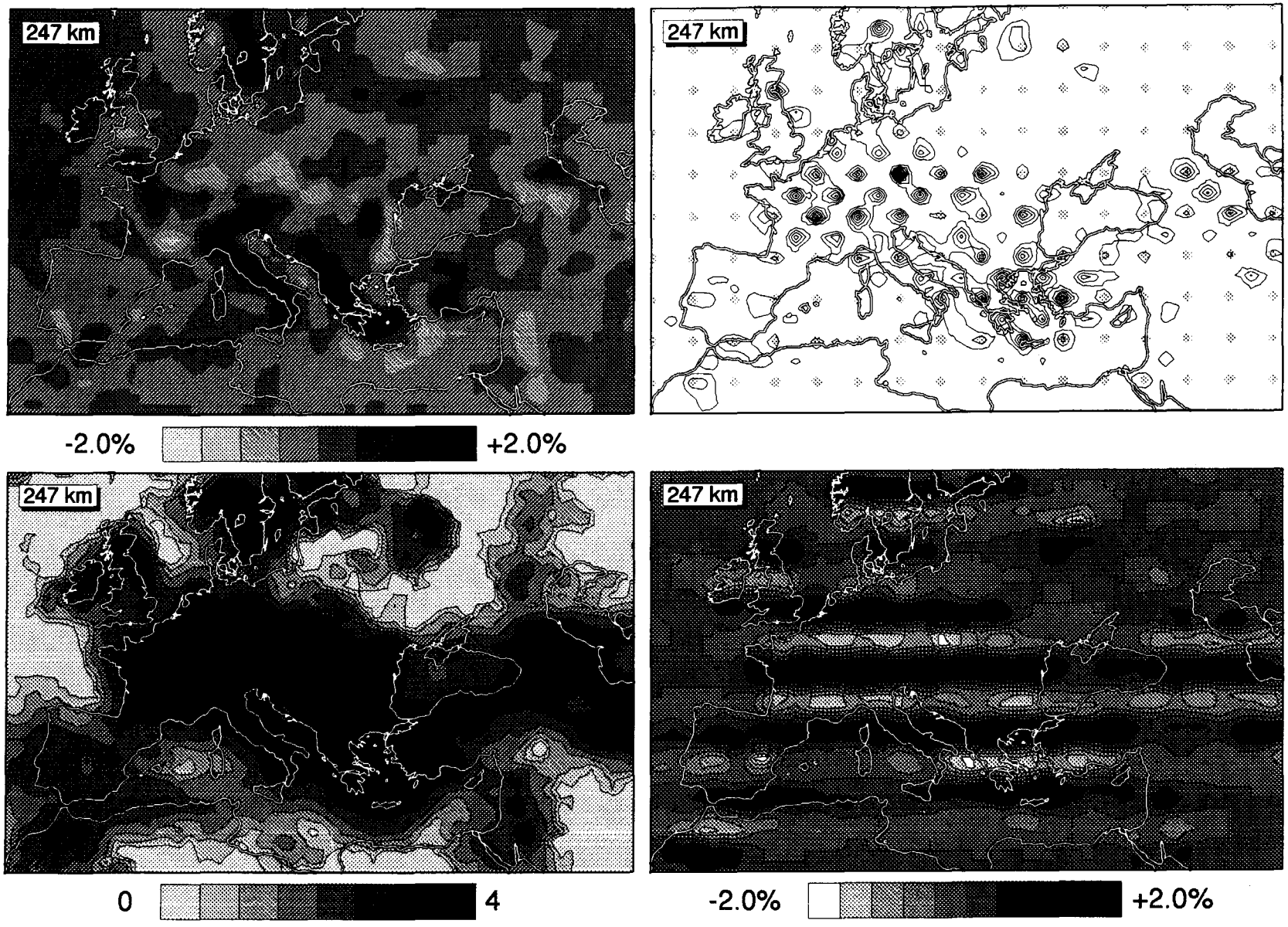

Appendix A: (continued). Fig. A6.

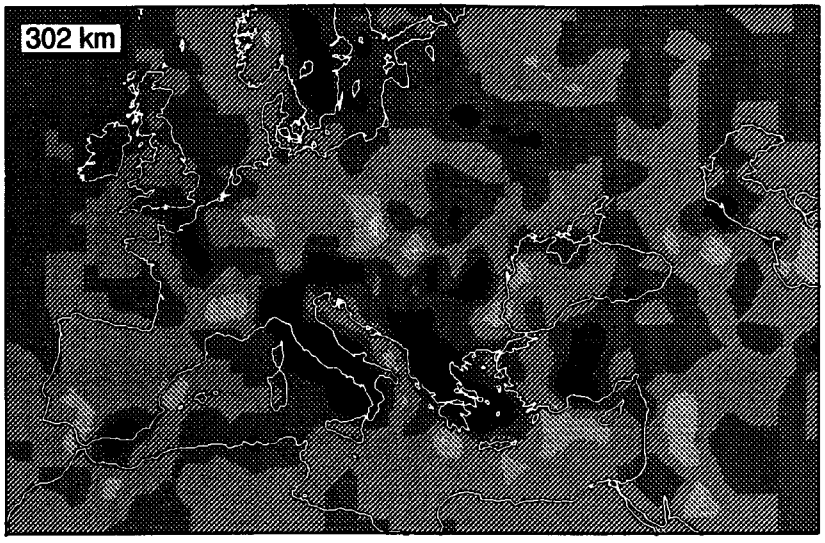

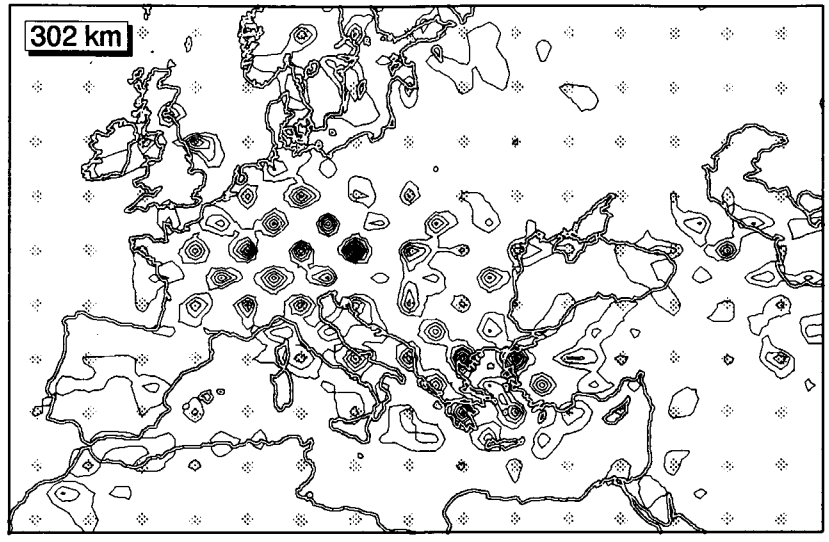

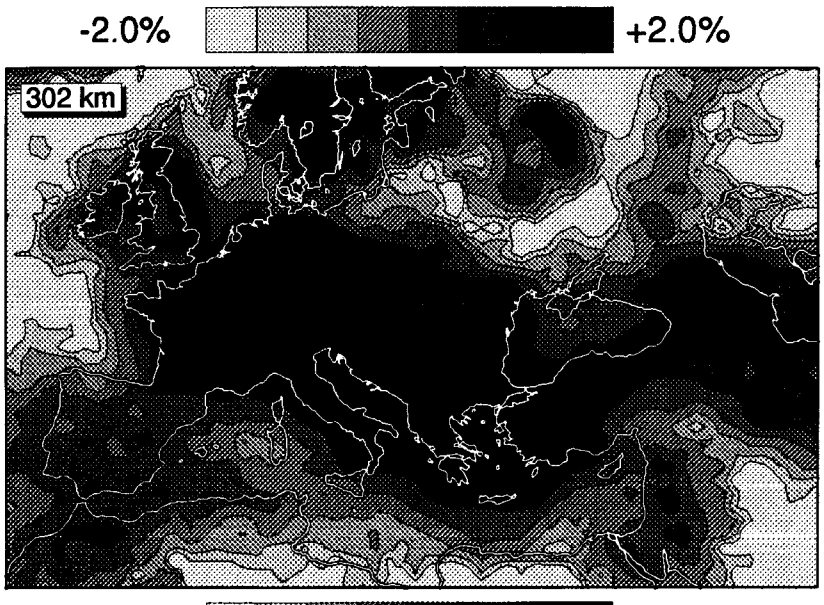

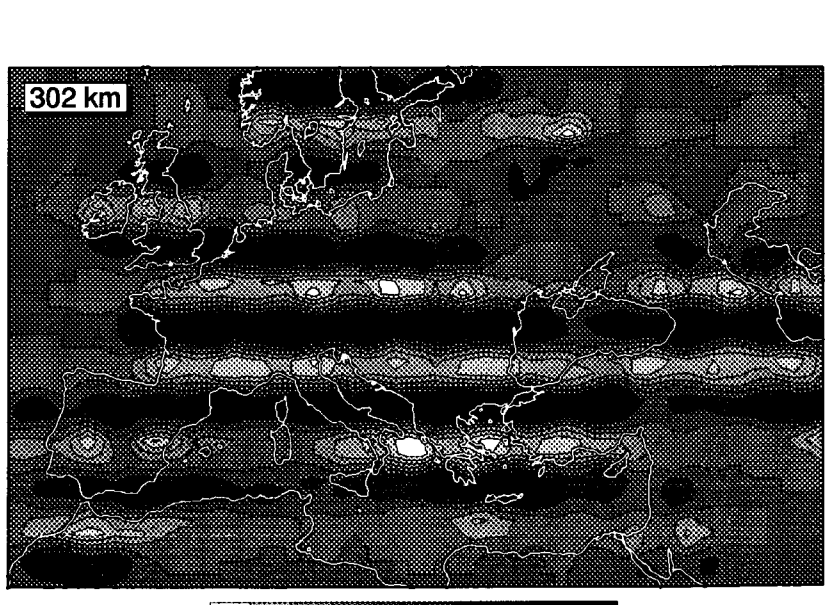

Appendix A: (continued). Fig. A7.

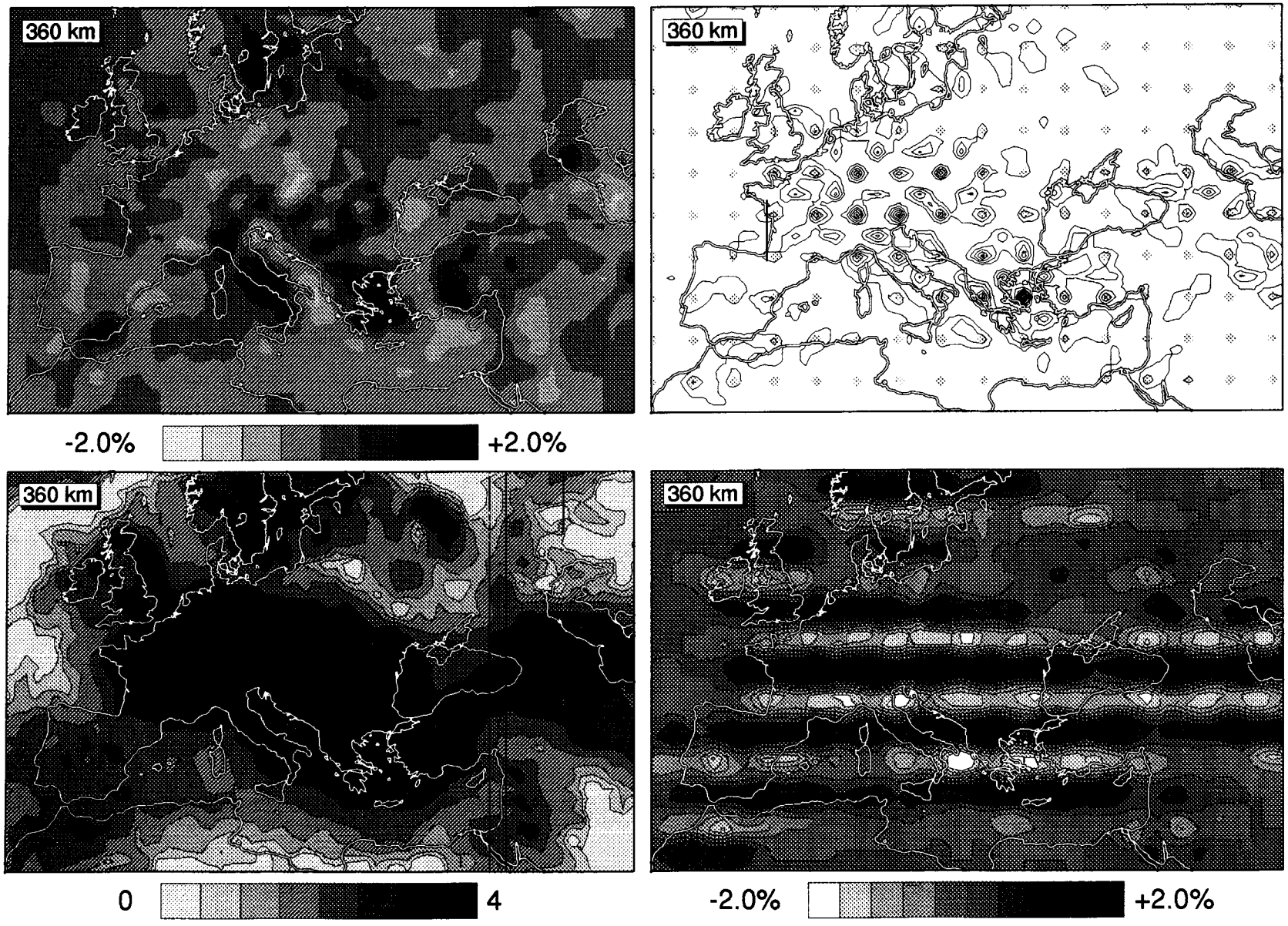

Appendix A: (continued). Fig. A8.

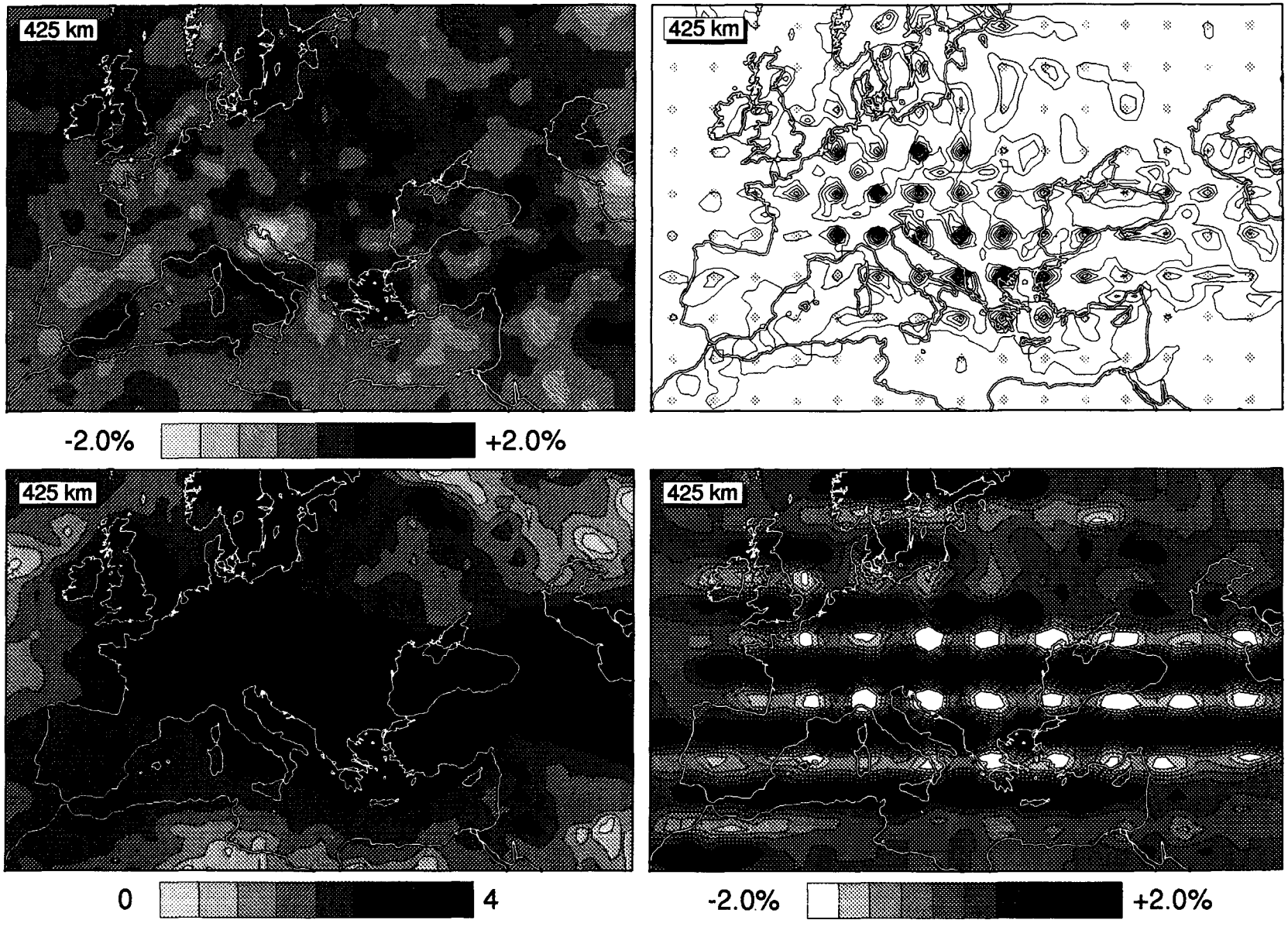

Appendix A: (continued). Fig. A9.

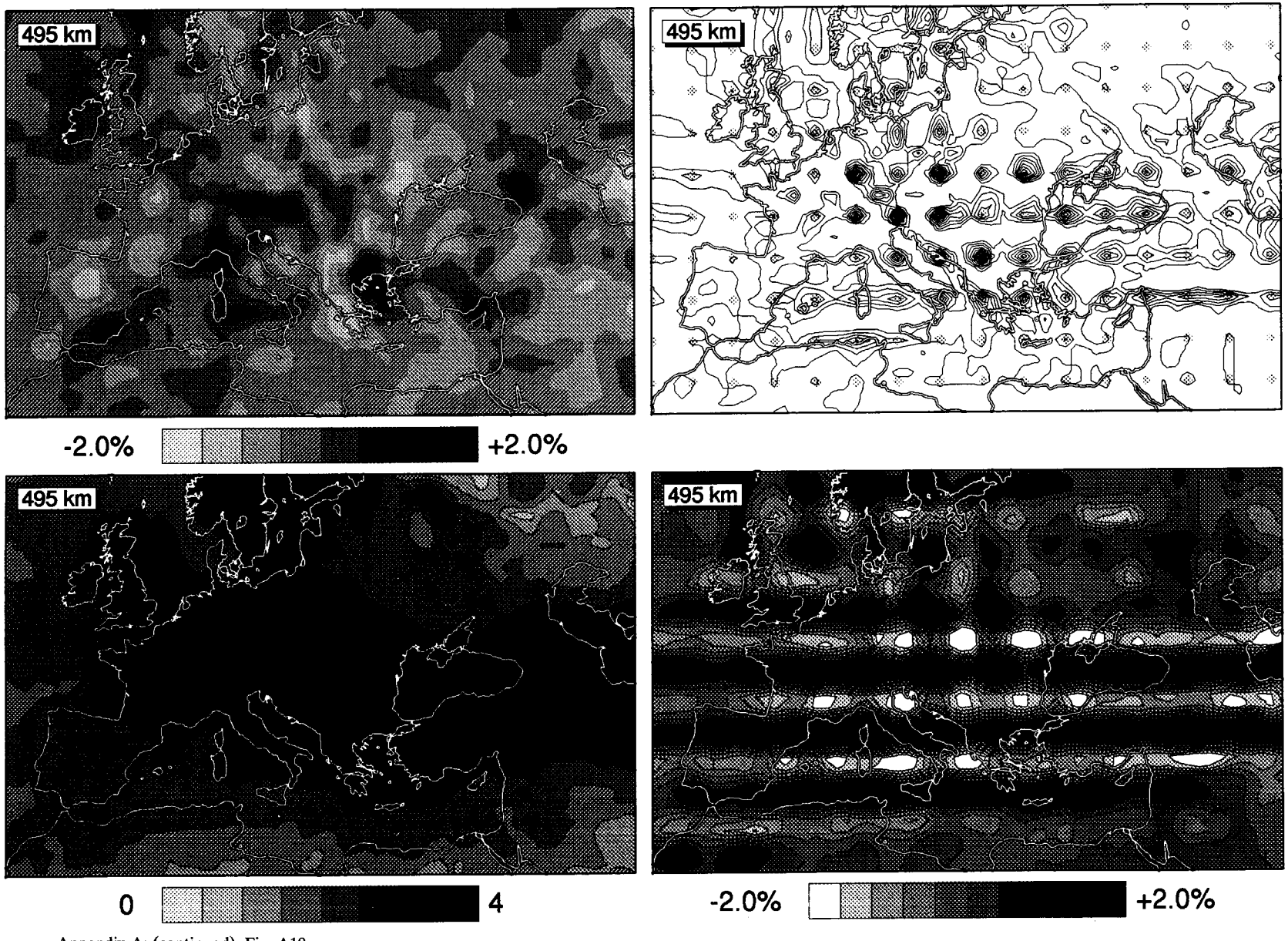

Appendix A: (continued). Fig. A10.

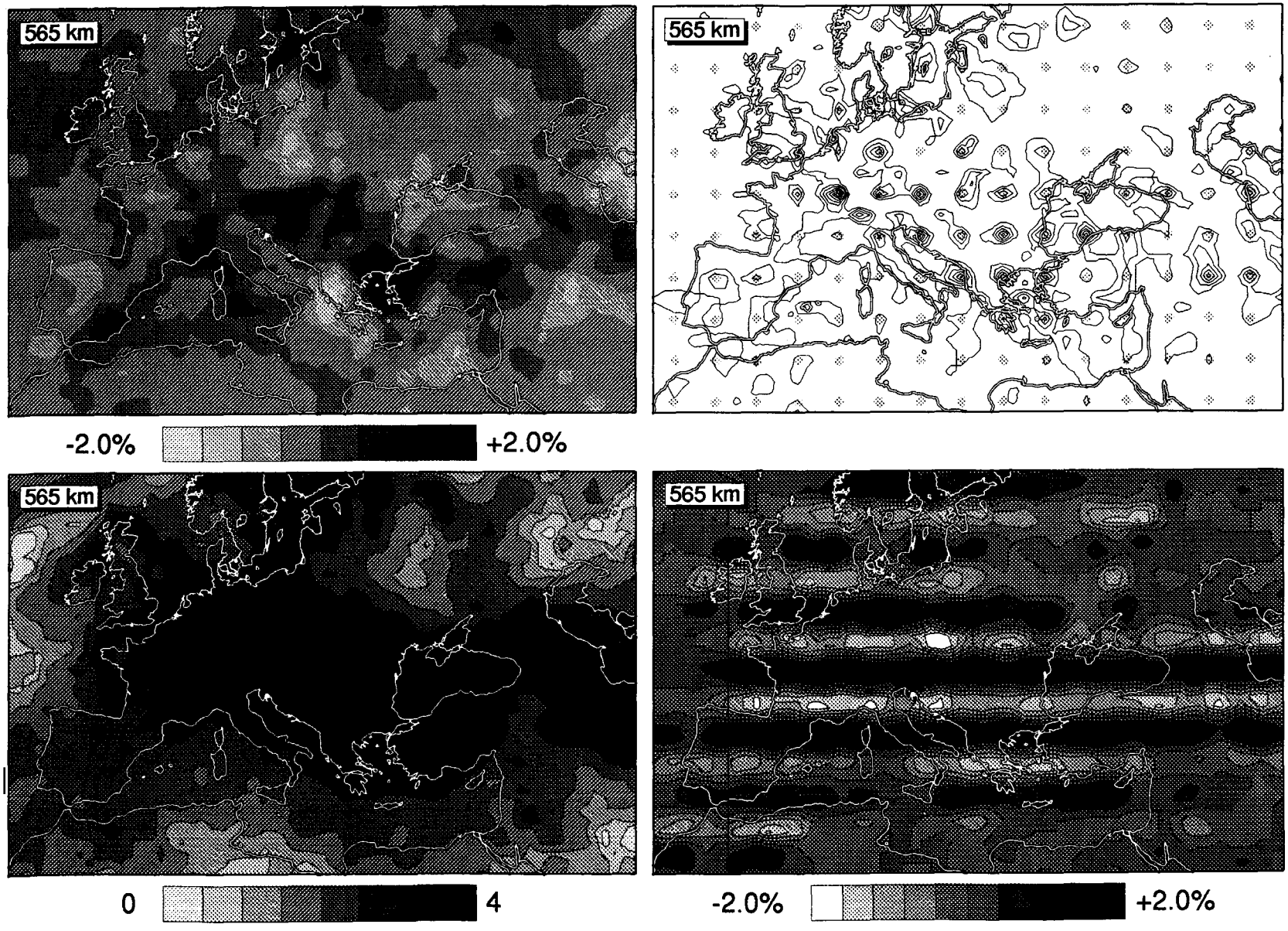

Appendix A: (continued). Fig. A11.

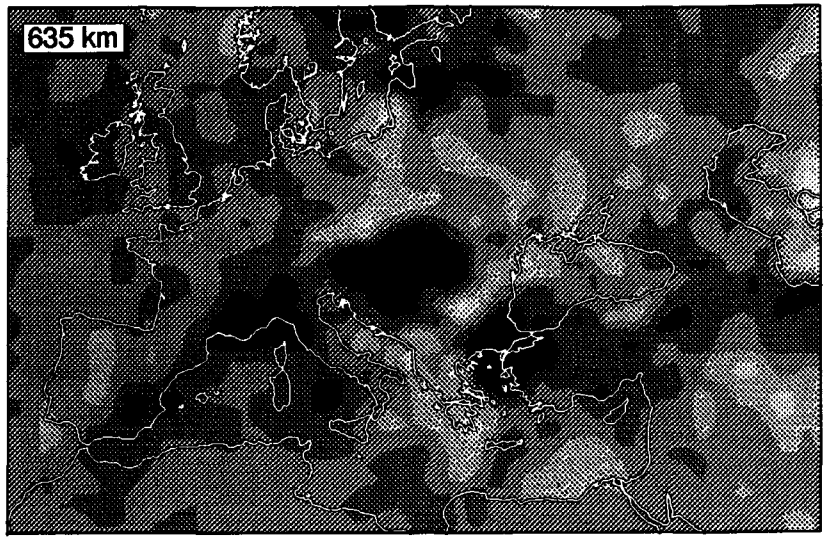

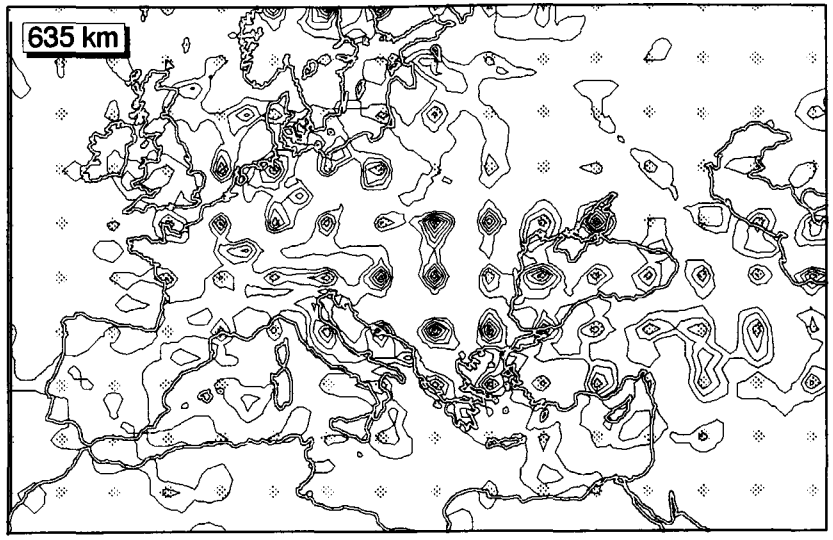

-2.0% +2.0%

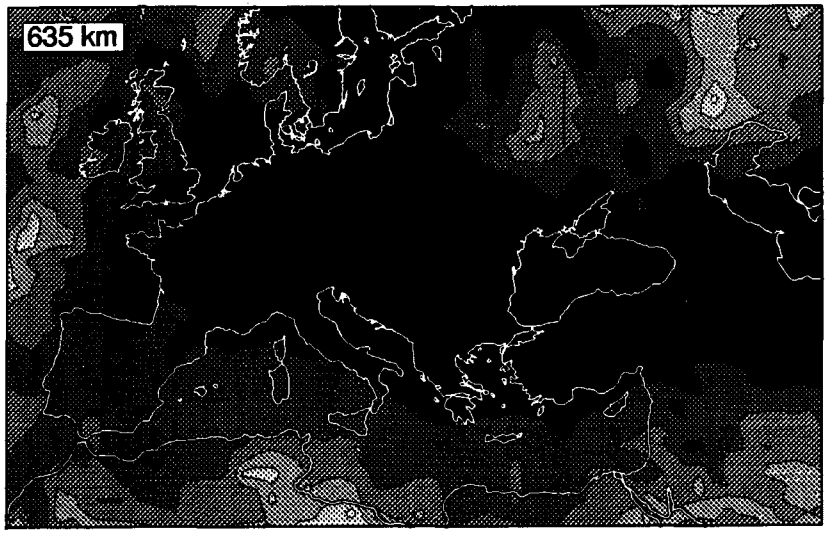

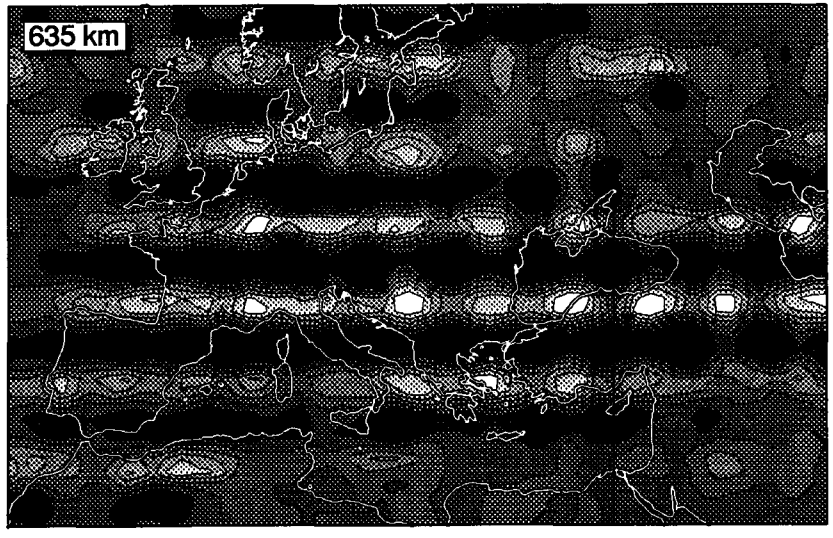

0 4

-2.0% +2.0%

Appendix A: (continued). Fig. A12.

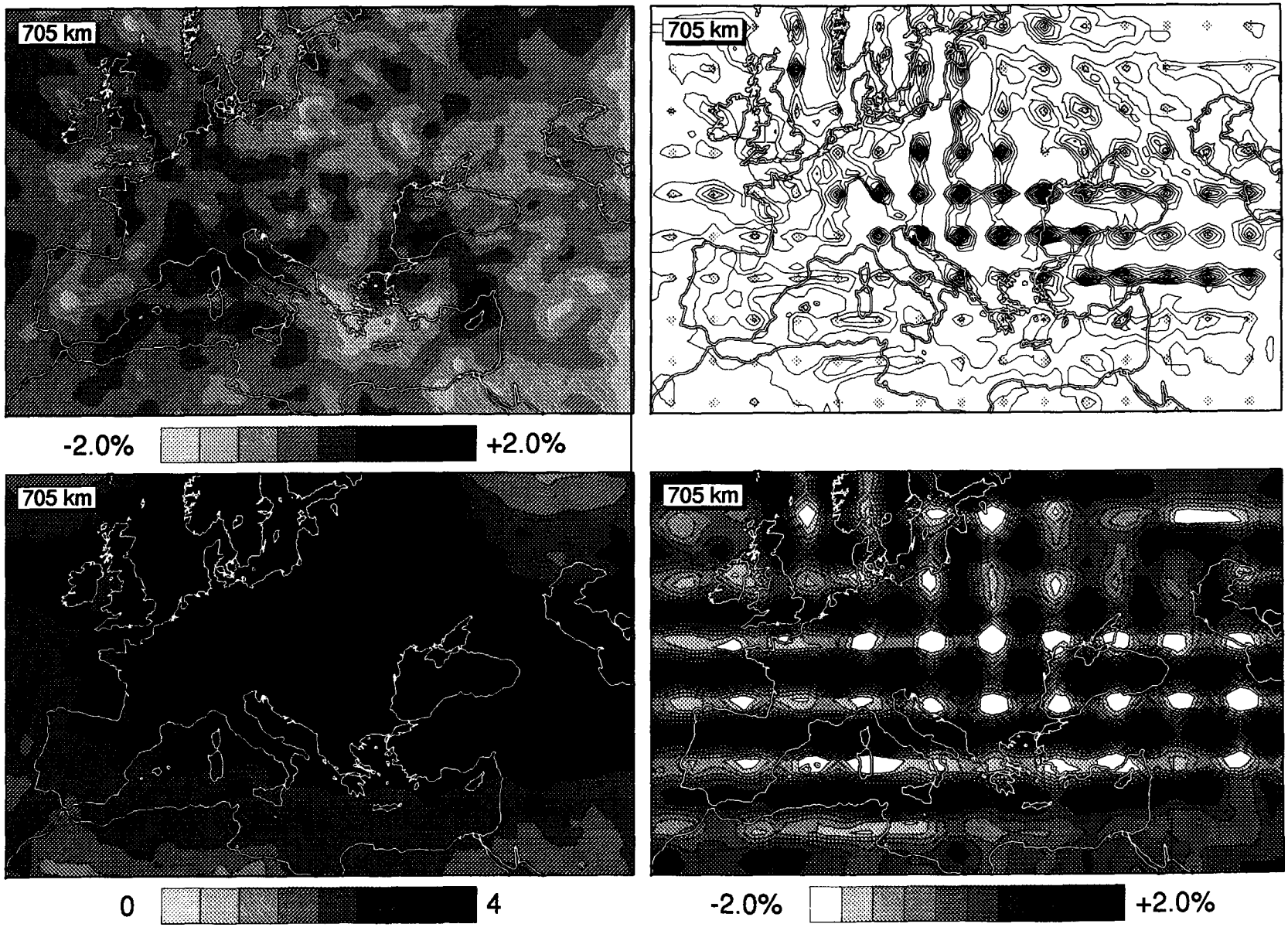

Appendix A: (continued). Fig. A13.

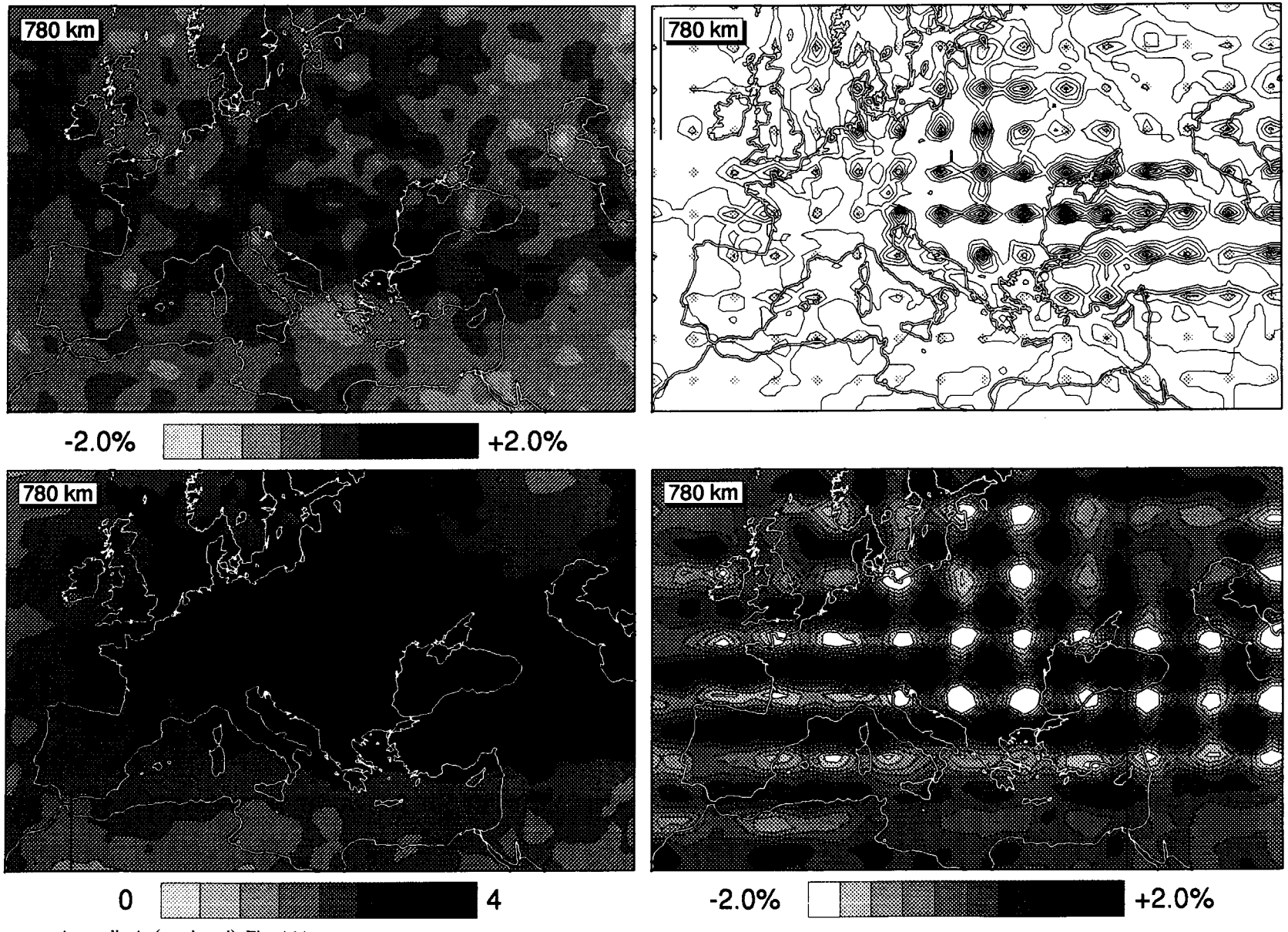

Appendix A: (continued). Fig. A14.

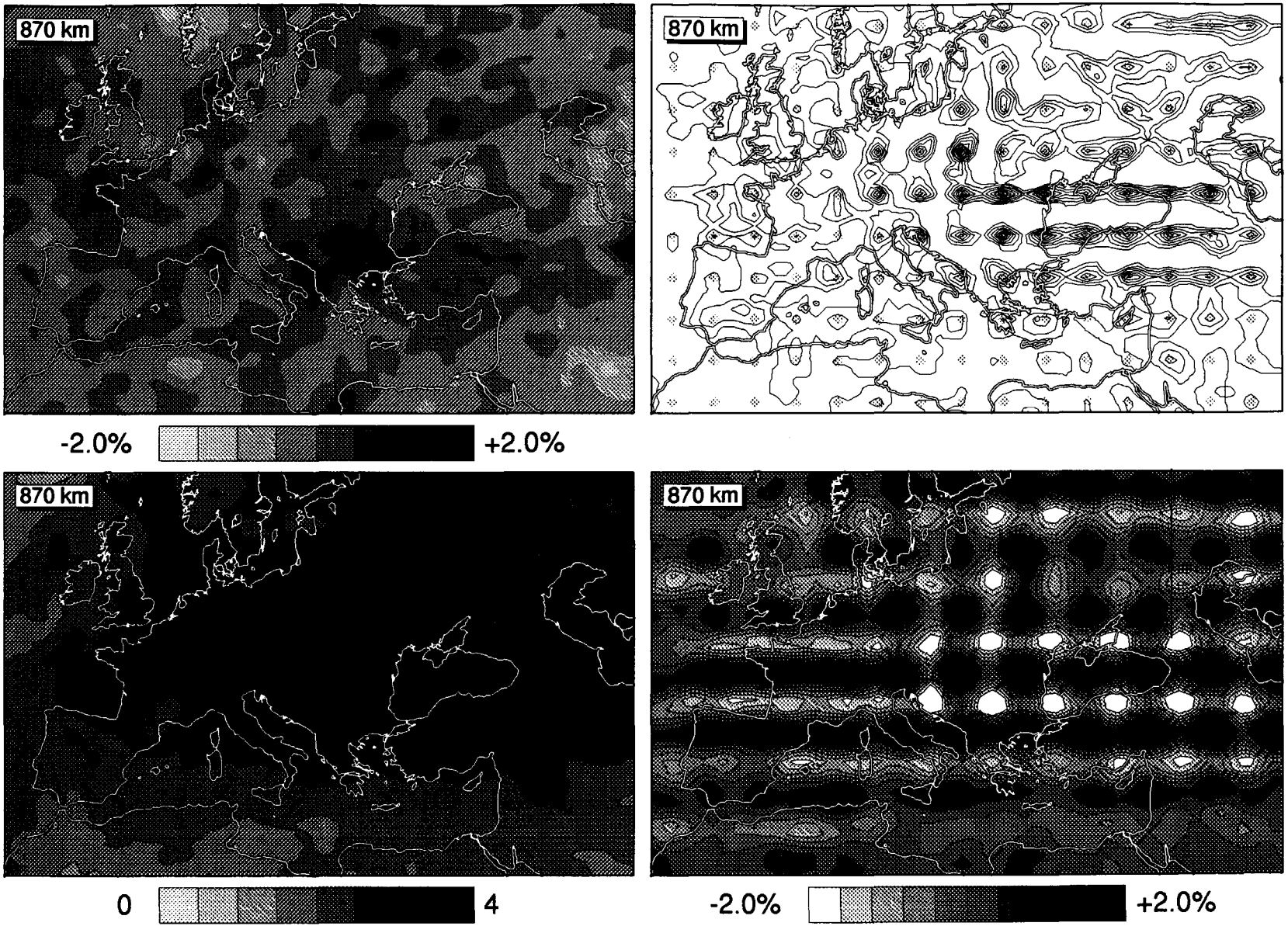

Appendix A: (continued). Fig. A15.

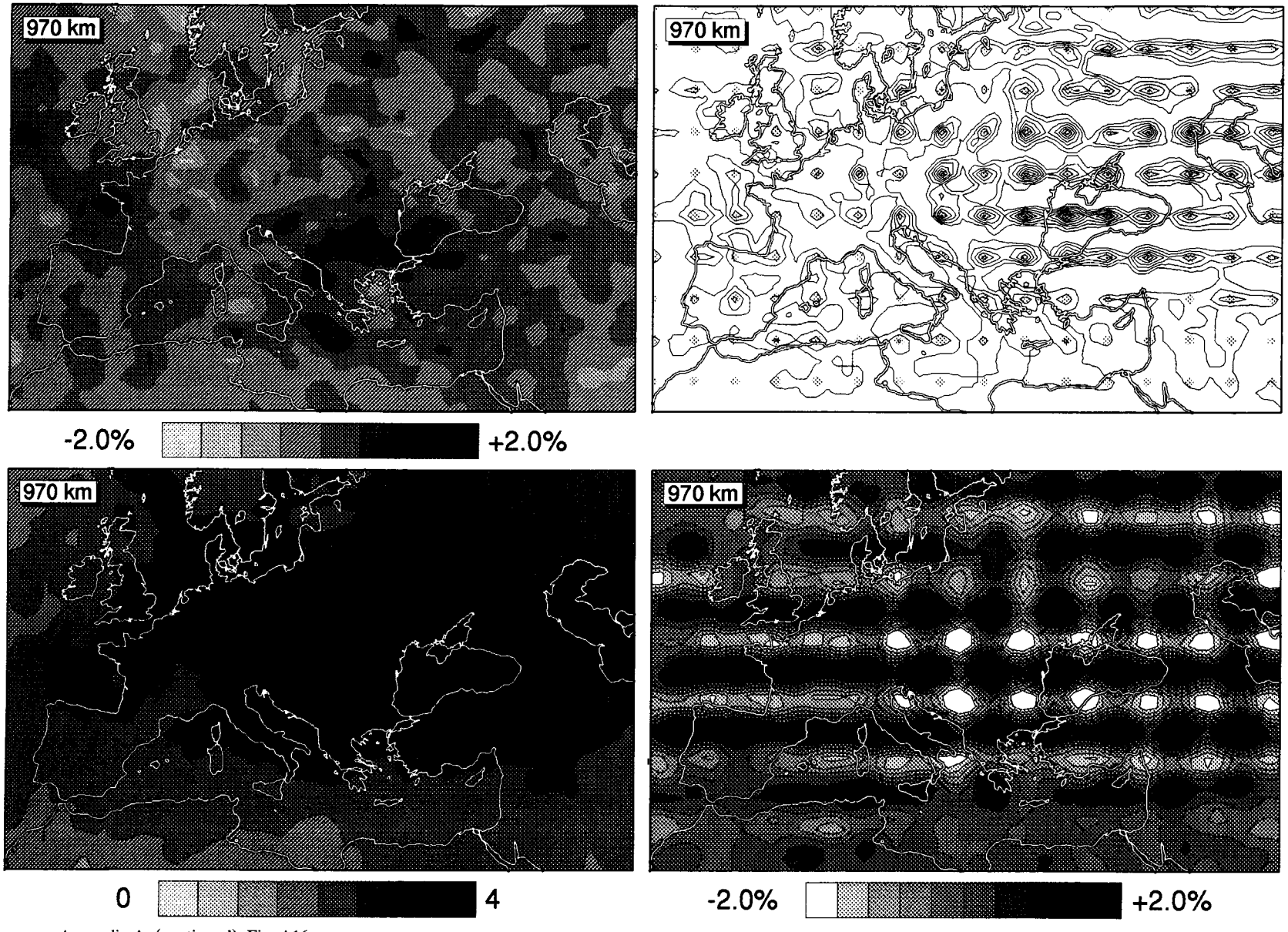

Appendix A: (continued). Fig. A16.

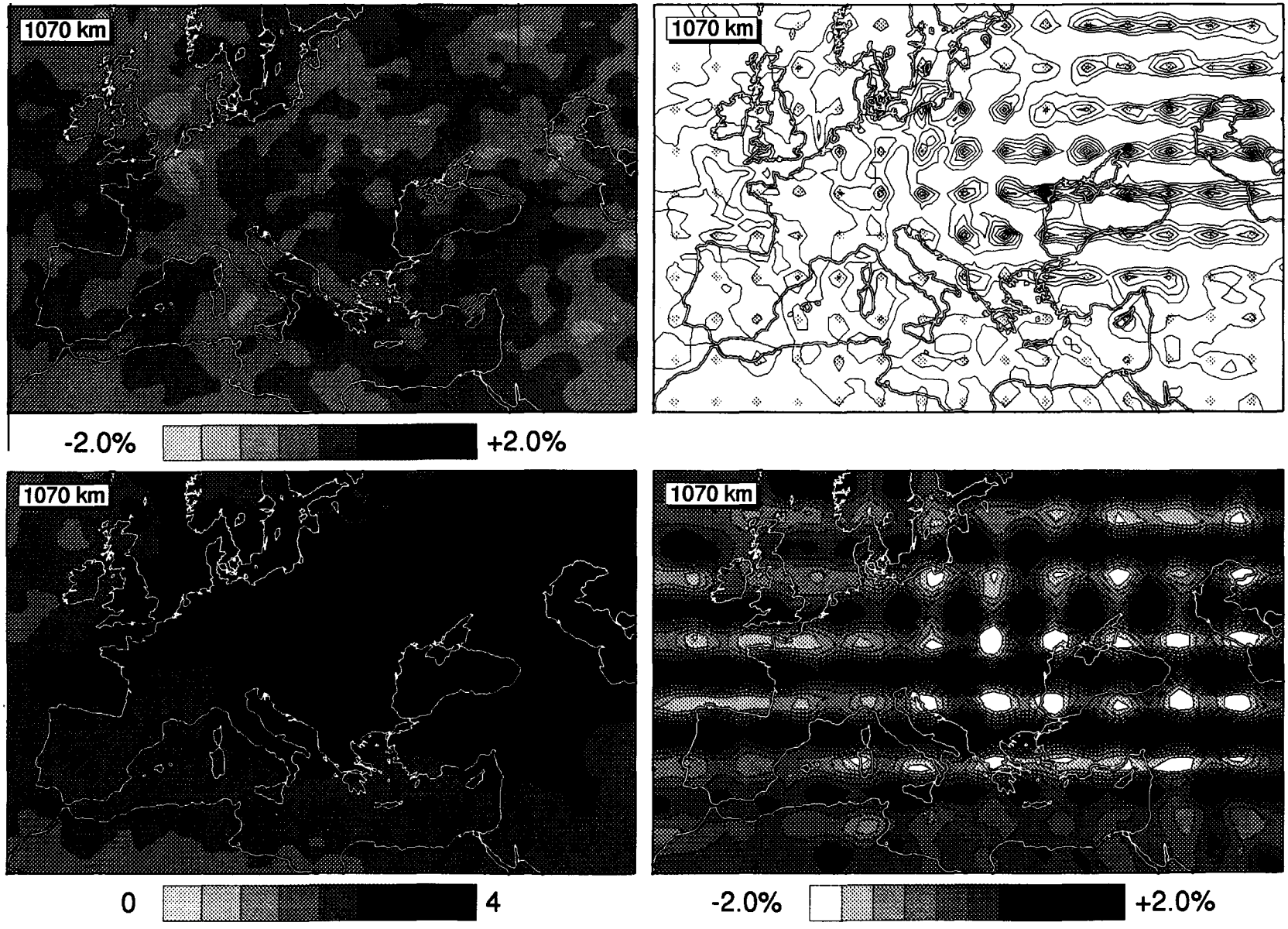

Appendix A: (continued). Fig. A17.

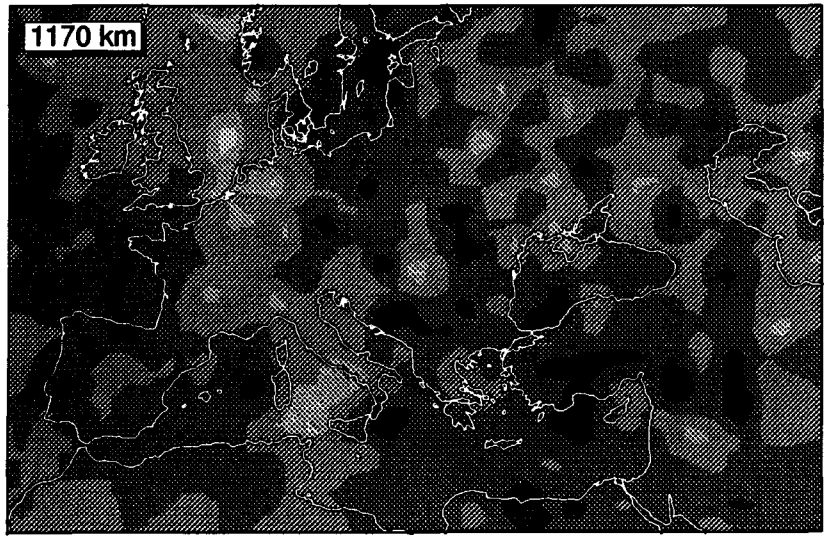

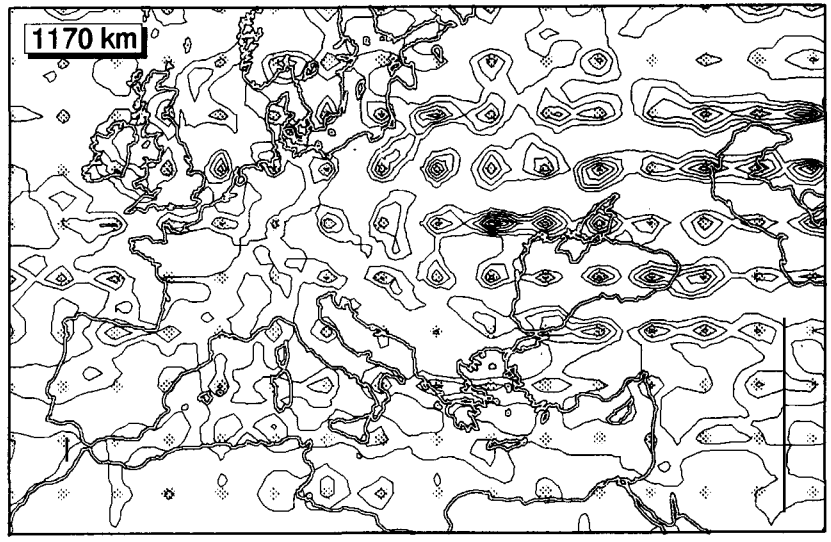

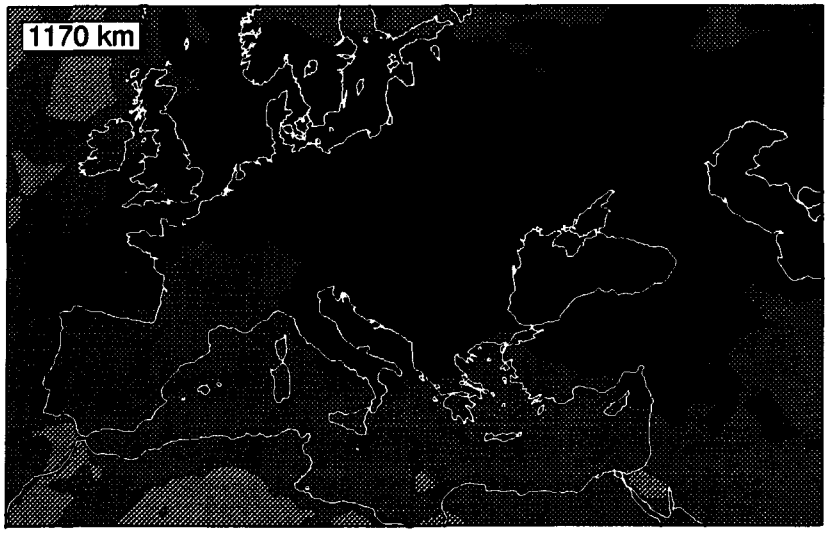

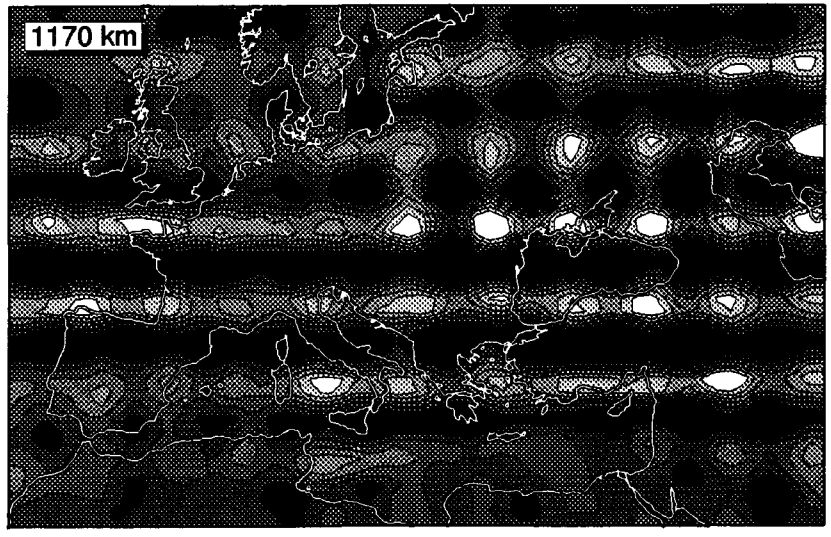

Appendix A: (continued). Fig. A18.

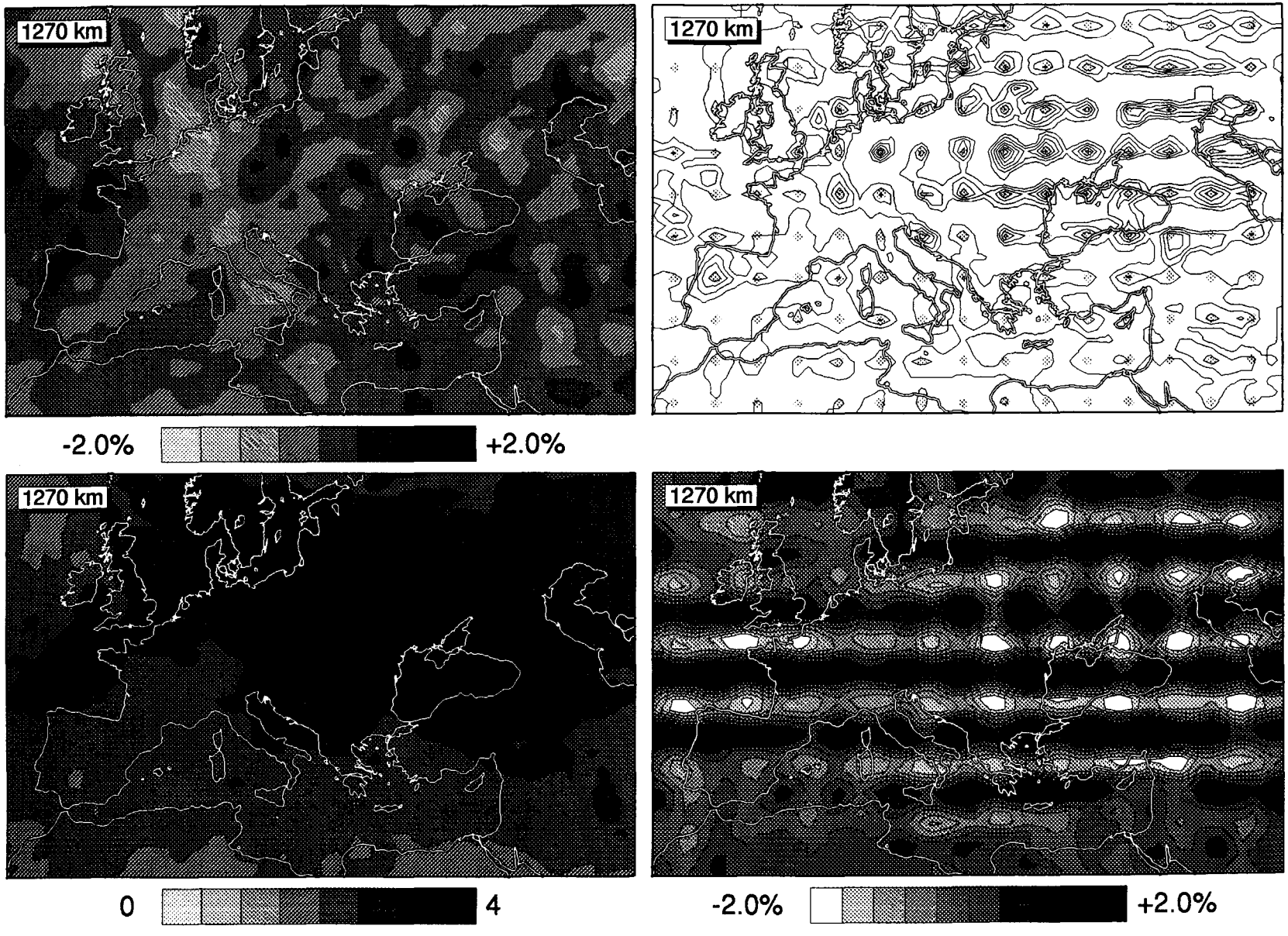

Appendix A: (continued). Fig. A19.

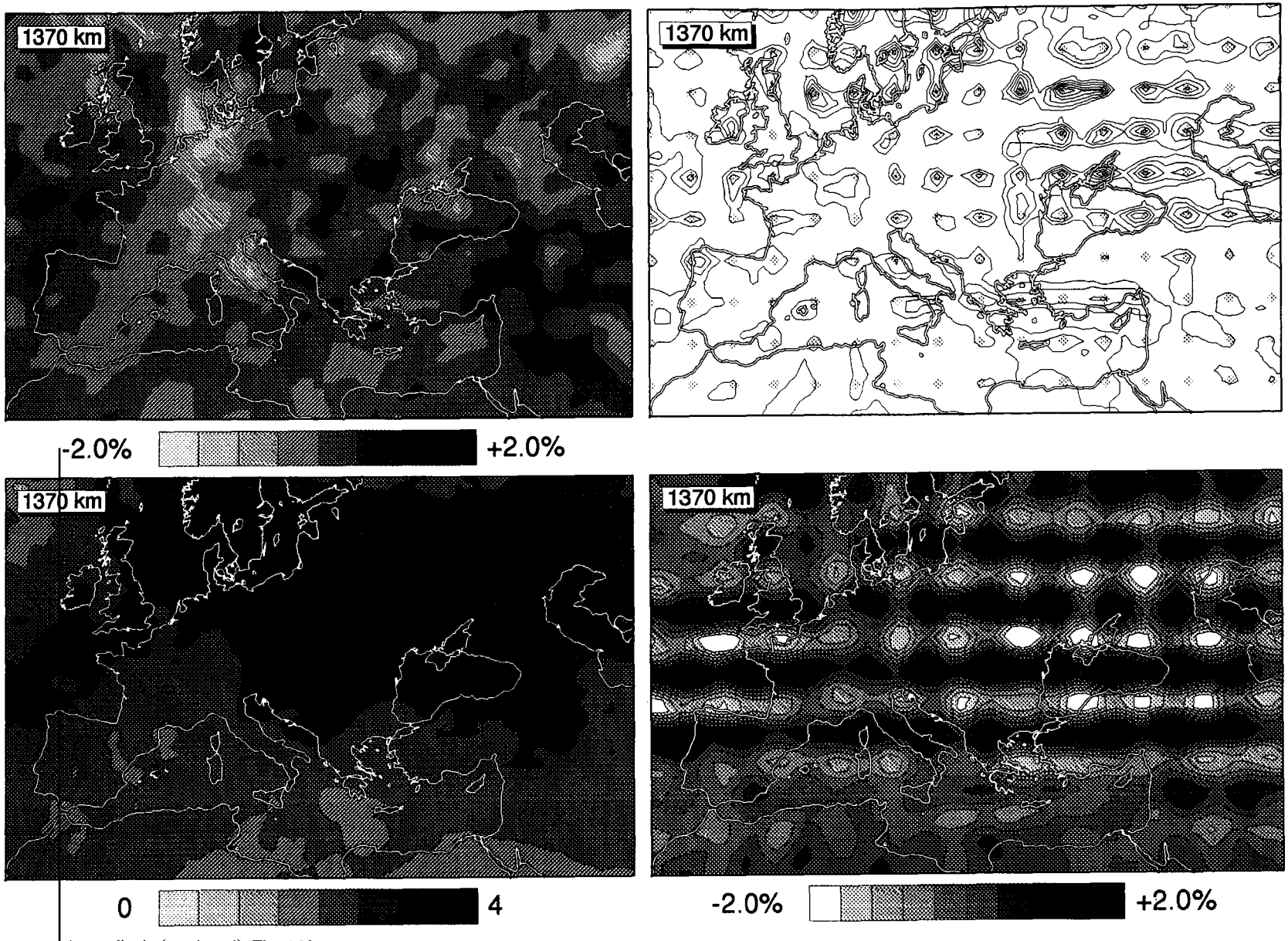

Appendix A: (continued). Fig. A20.

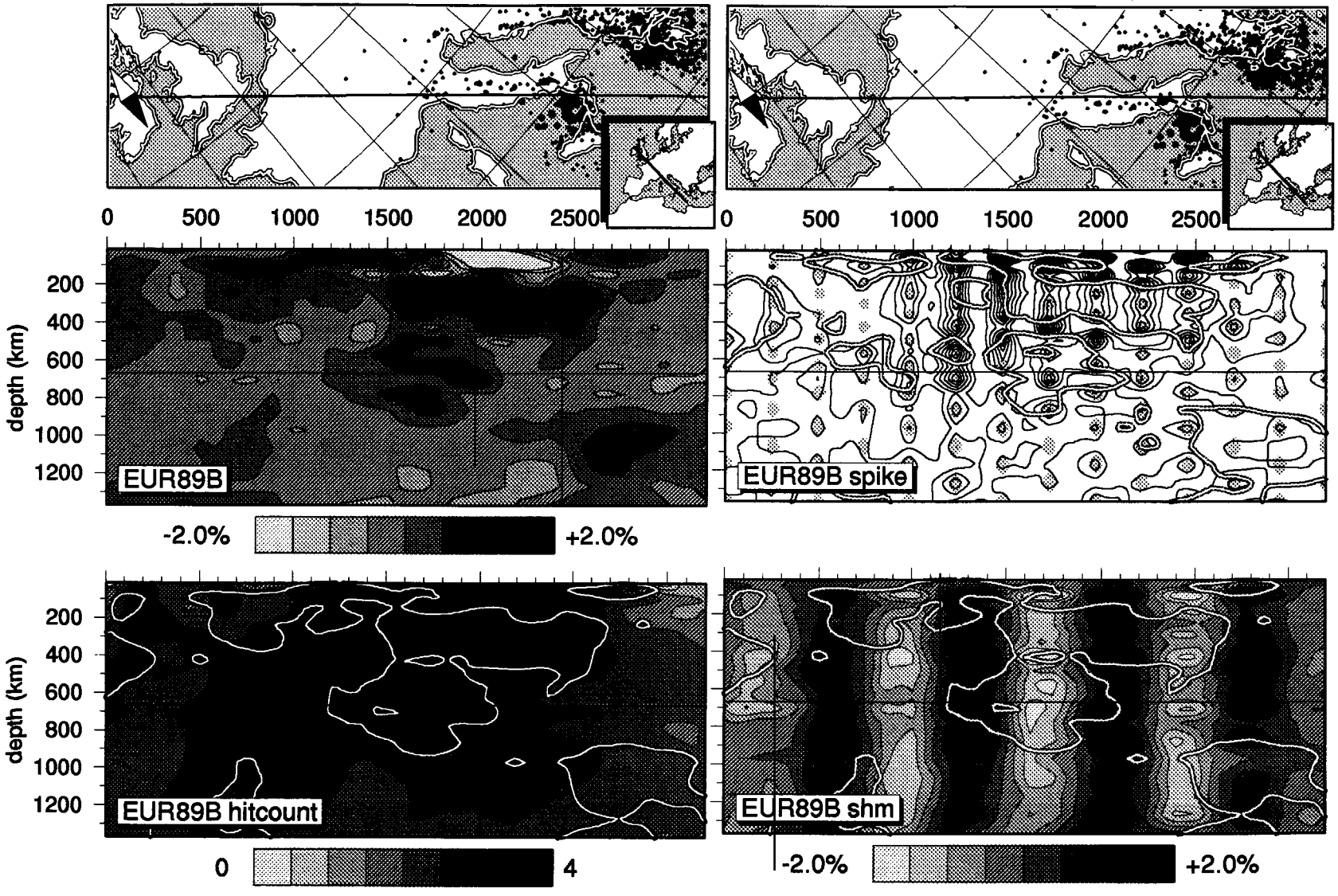

Appendix B: Fig. B1.
Nine vertical sections through model EUR89B, hit count and sensitivity test results. (See section 6.2.2 for description.)

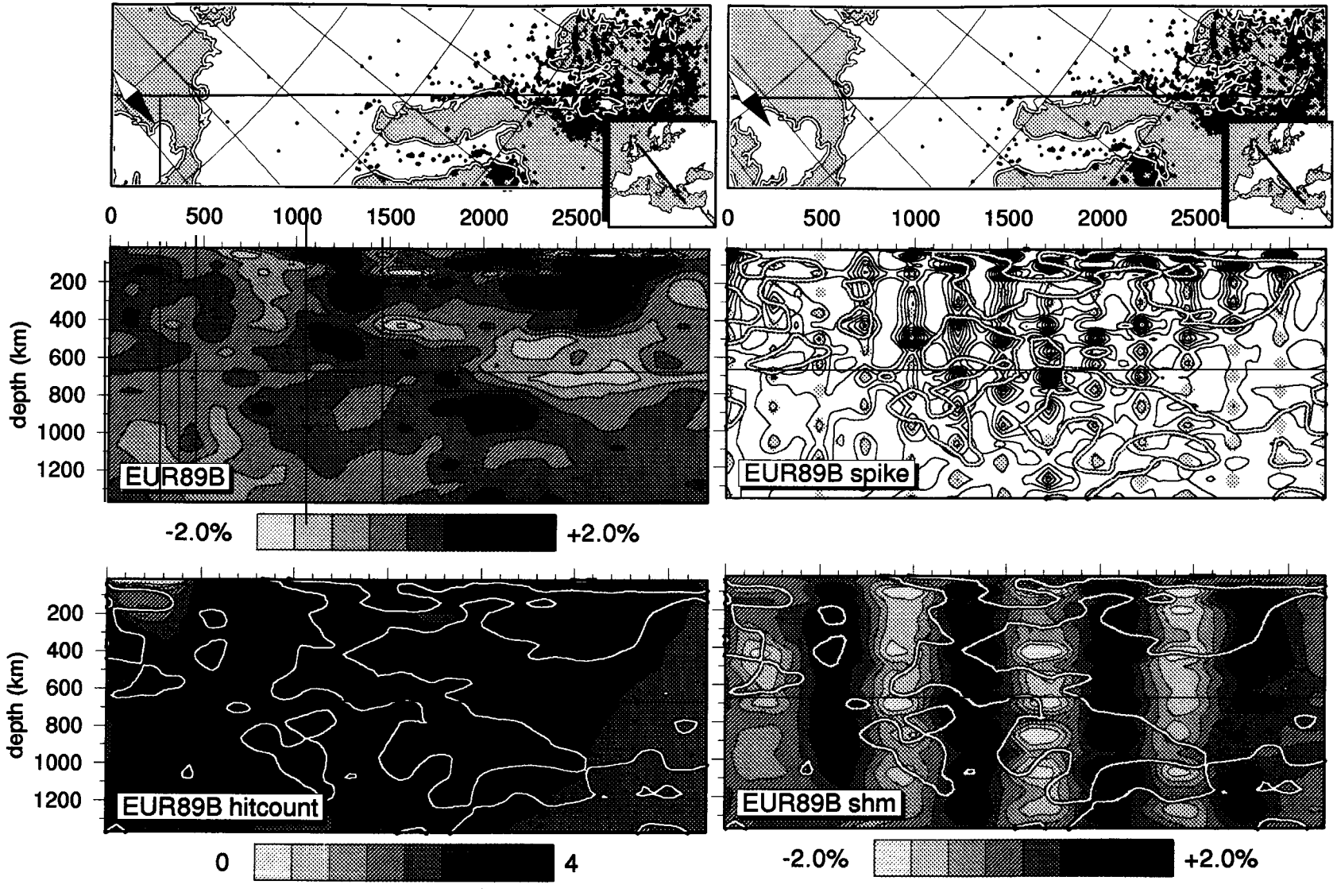

Appendix B: (continued). Fig. B2.

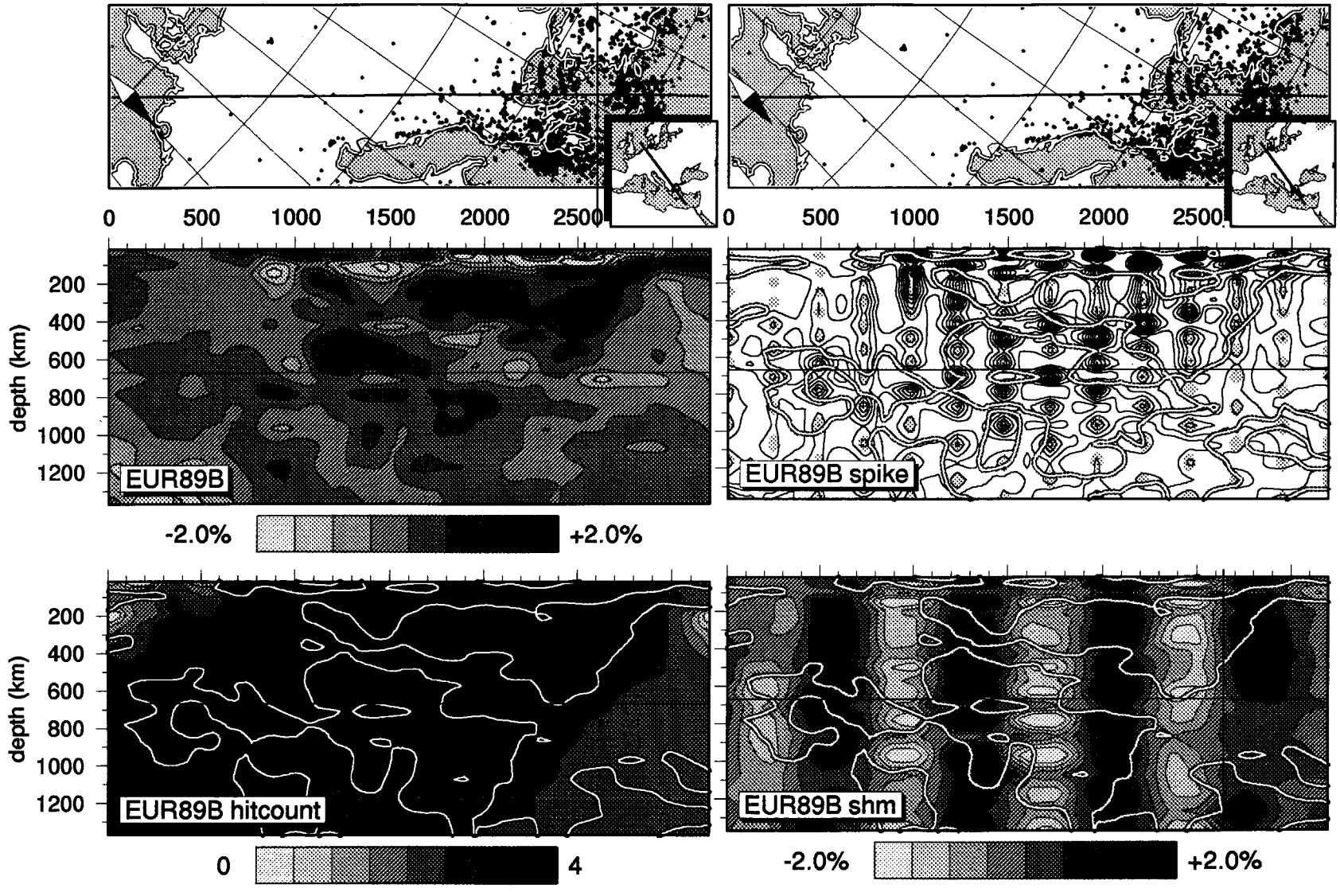

Appendix B: (continued). Fig. B3.

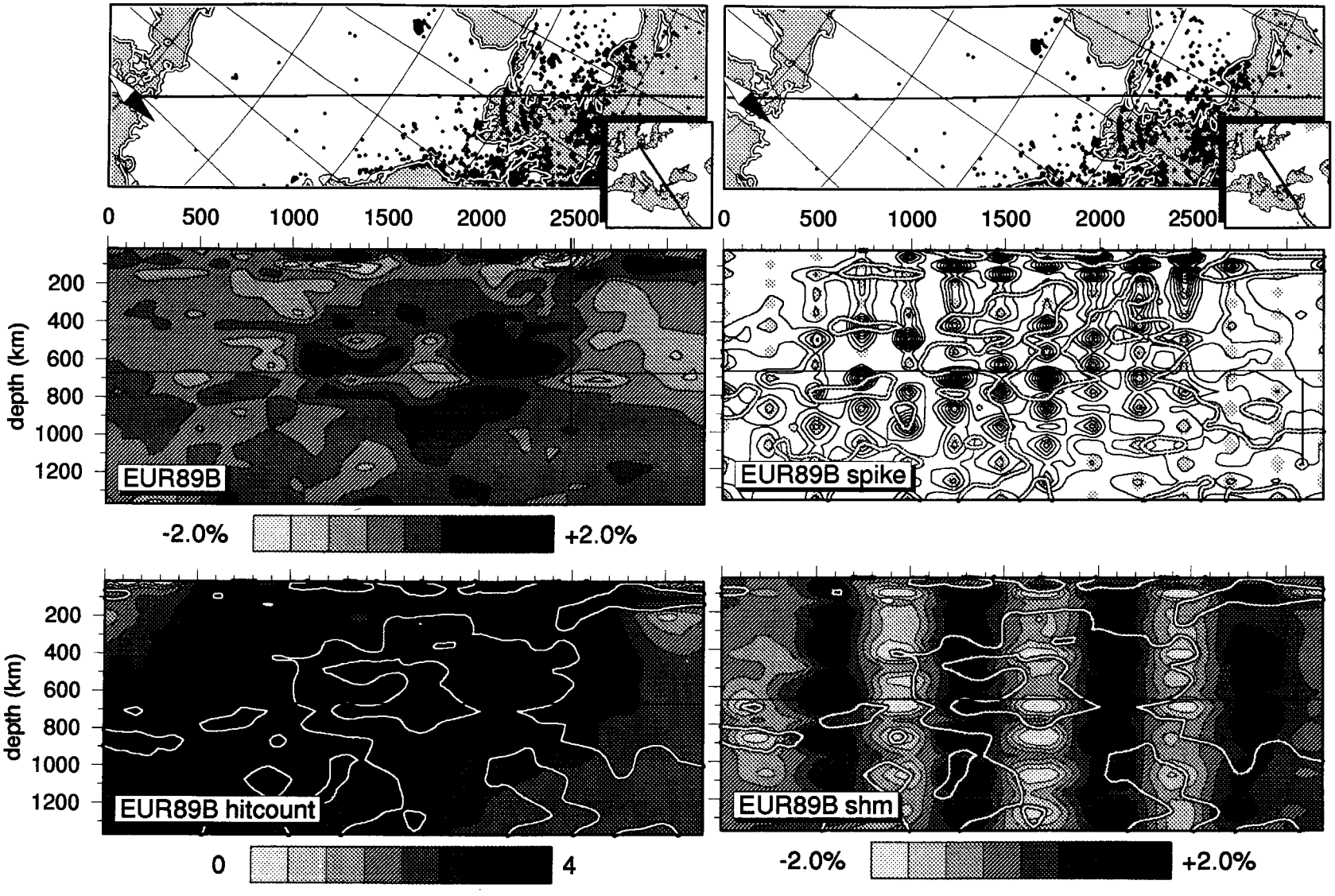

Appendix B: (continued). Fig. B4.

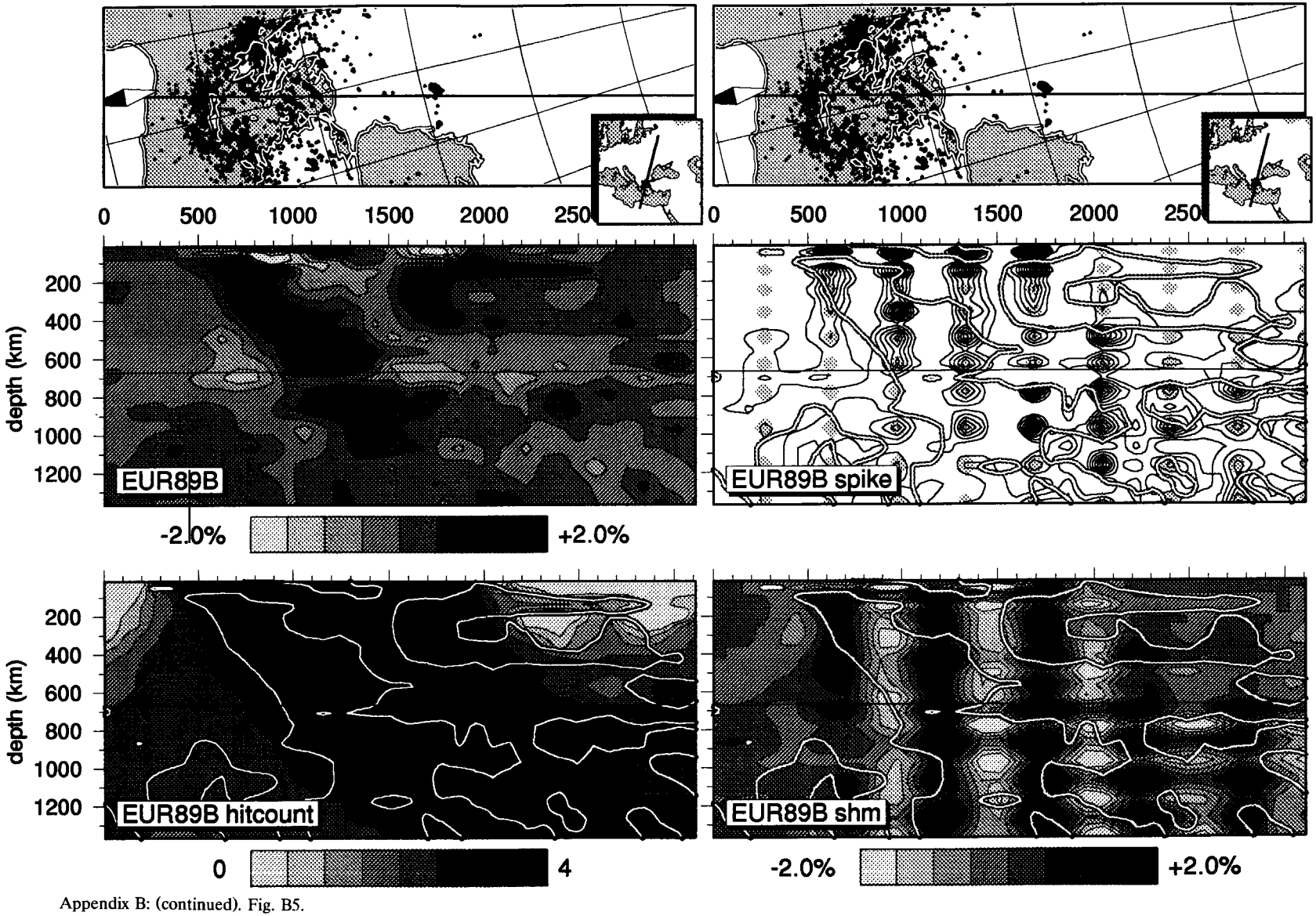

Appendix B: (continued). Fig. B5.

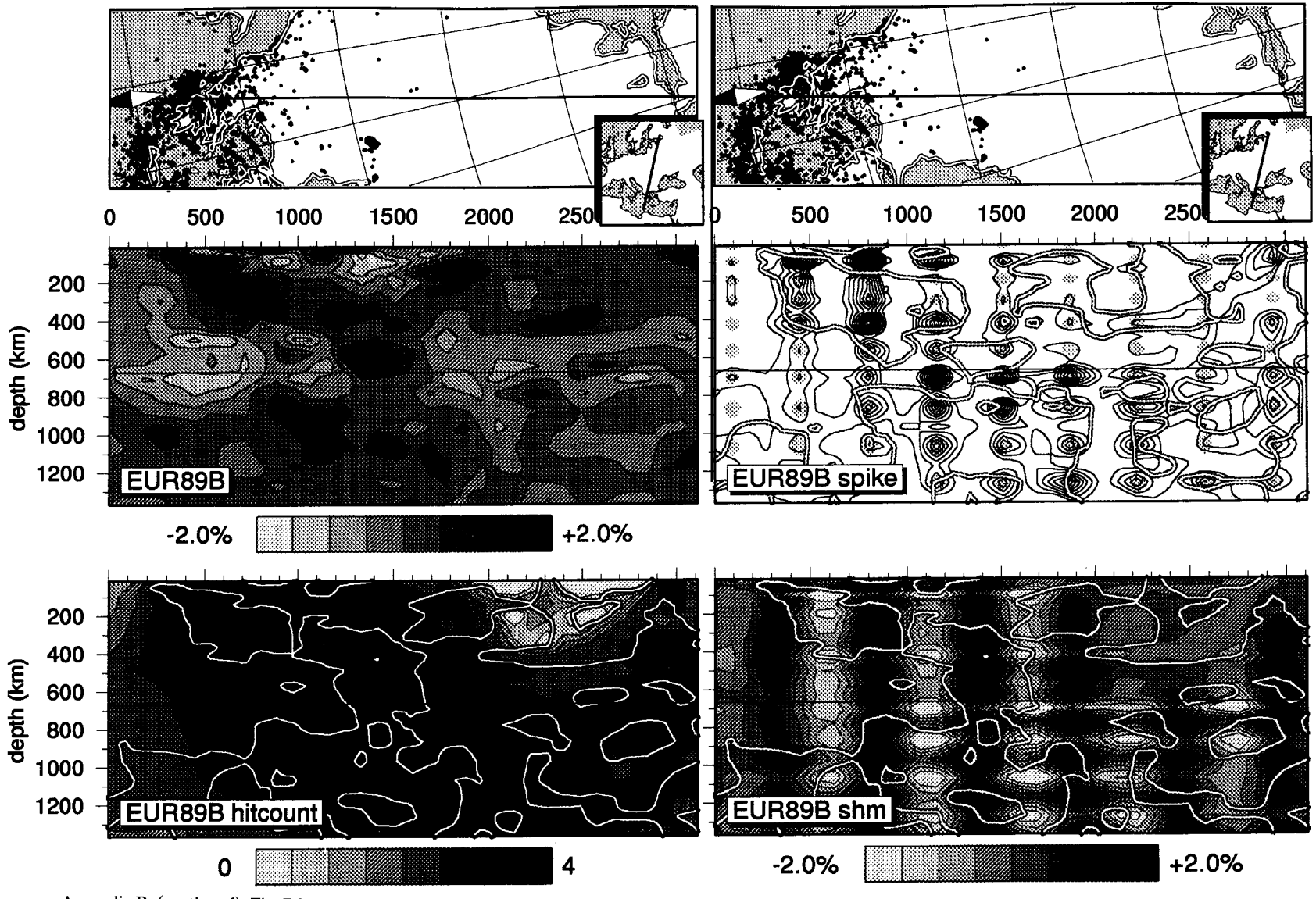

Appendix B: (continued). Fig. B6.

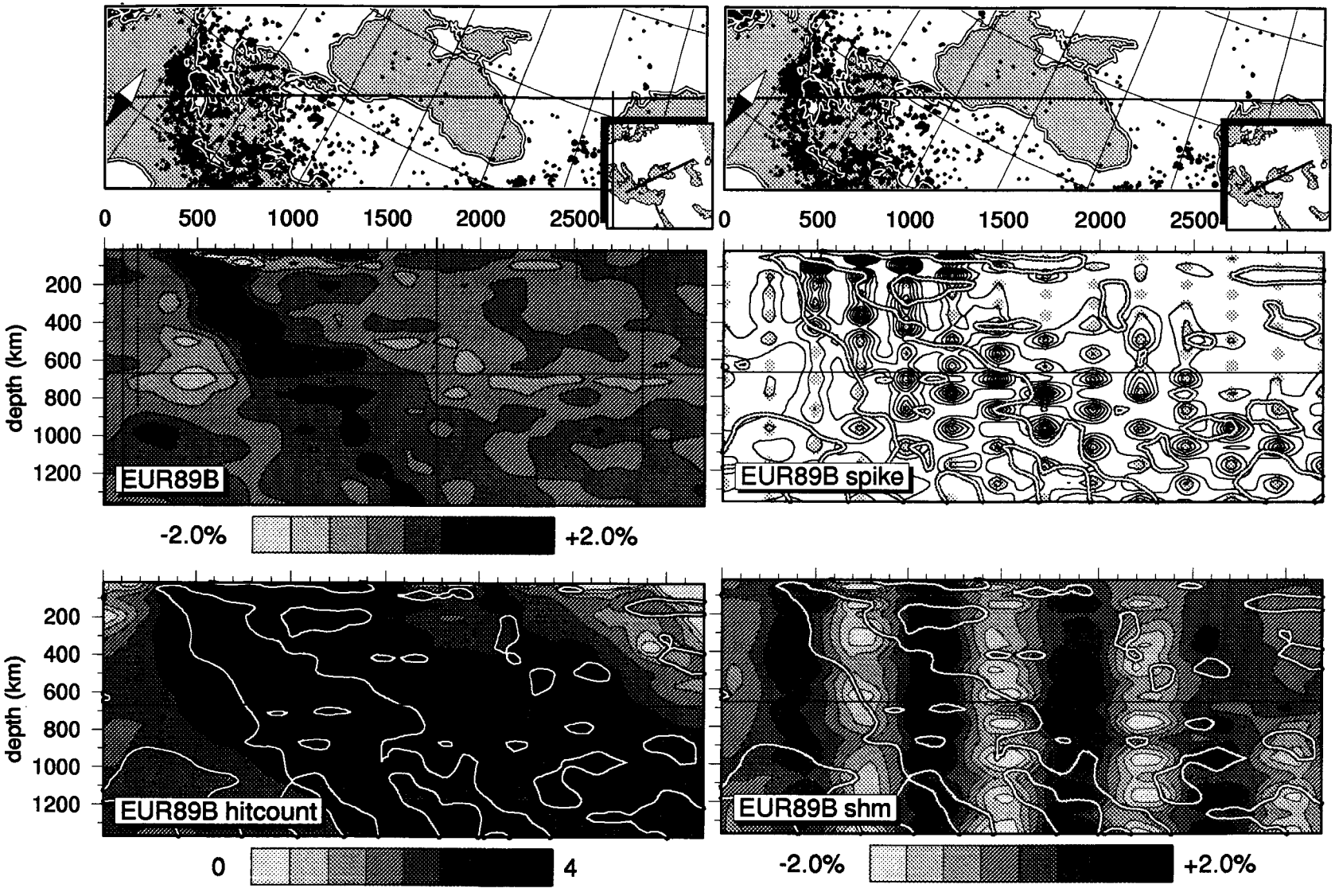

Appendix B: (continued). Fig. B7.

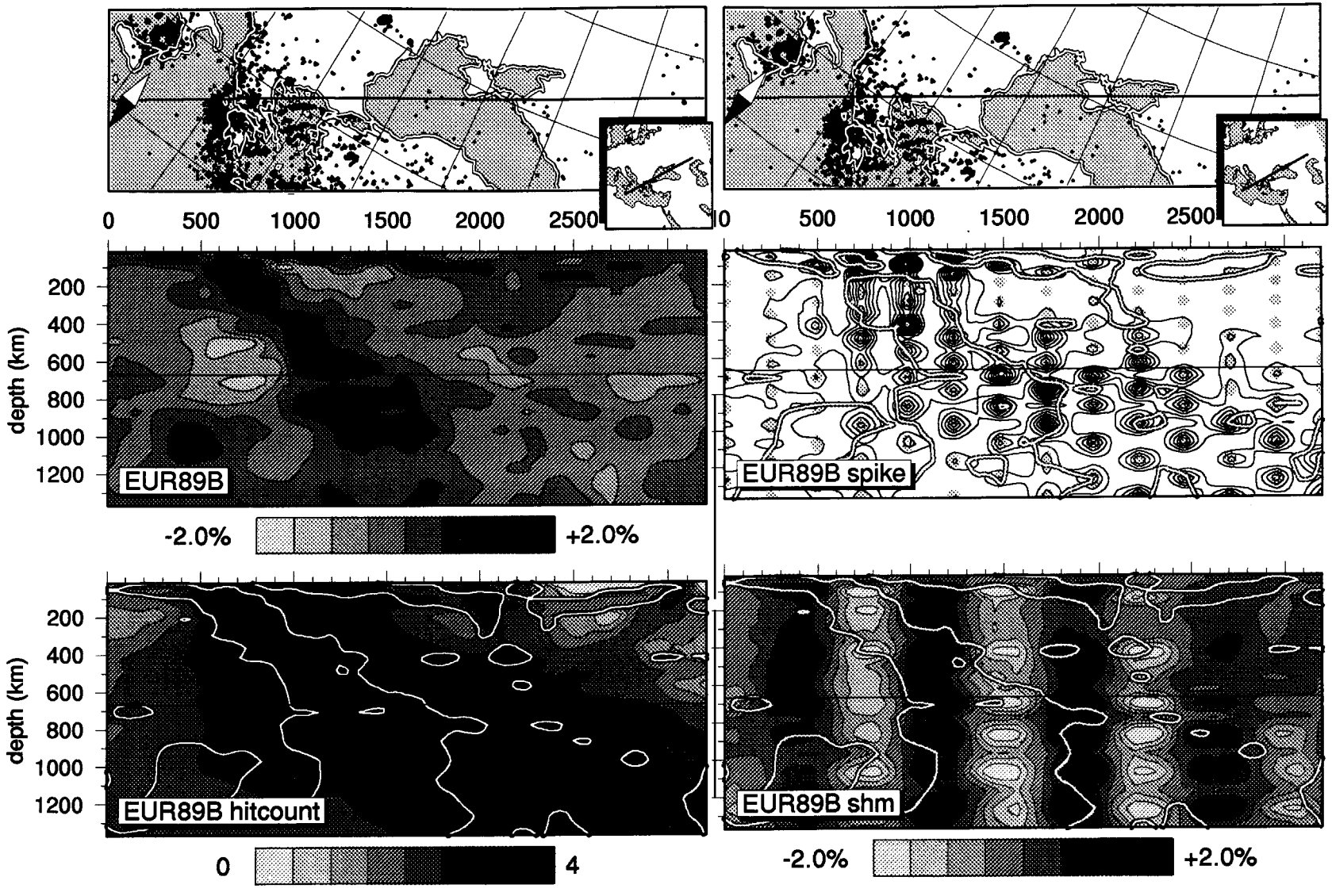

Appendix B: (continued). Fig. B8.

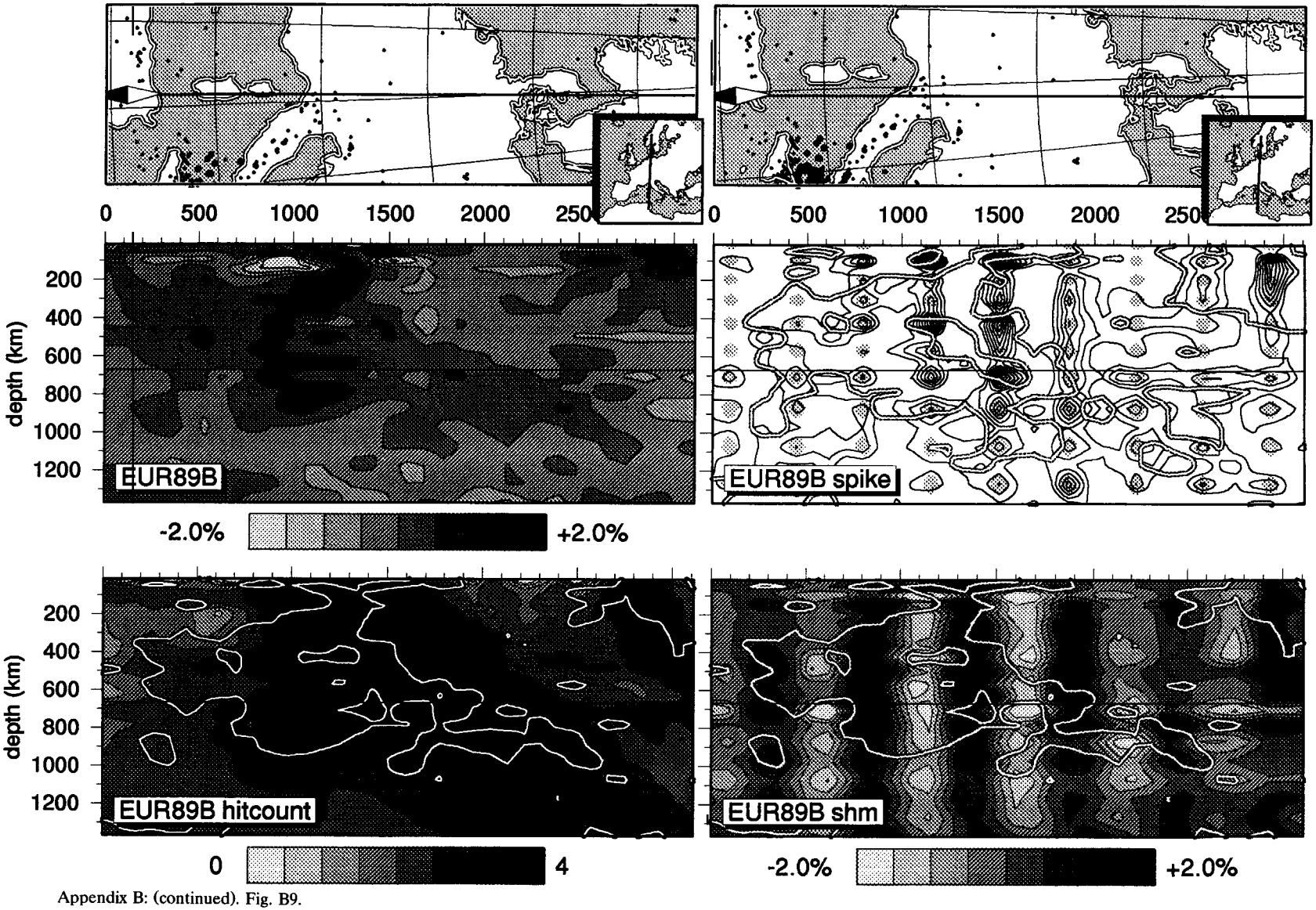

Appendix B: (continued). Fig. B9.

References

Aki, K., Christoffersson, A. and Husebye, E.S., 1977. Determination of the three-dimensional seismic structure of the lithosphere. Geophys. J.R. Astron. Soc., 82 (2): 277–296.

Amato, A., Alessandrini, B. and Cimini, G.B., 1993. Teleseismic wave tomography of Italy. In: H.M. Iyer and K. Hirahara (Editors), Seismic Tomography: Theory and Practice. Chapman and Hall, London, pp. 361–396.

Babuska, V., Plomerova, J. and Sileny, J., 1984. Spatial variations of P residuals and deep structure of the European lithosphere. Geophys. J.R. Astron. Soc., 79: 363–383.

Babuska, V., Plomerova, J. and Granet, M., 1990. The deep lithosphere in the Alps: a model inferred from P residuals. Tectonophysics, 176: 137–165.

Blanco, M.J. and Spakman, W., 1993. The P-wave velocity structure of the mantle below the Iberian Peninsula: evidence for subducted lithosphere below southern Spain. Tectonophysics, 221: 13–34.

Blundell, D., Freeman, R. and Mueller, S., 1992. A Continent Revealed: The European Geotraverse. Cambridge University Press, Cambridge, 274 pp.

Buforn, E., Udias, A. and Madariaga, R., 1991a, Intermediate and deep earthquakes in Spain. PAGEOPH, 4: 375–393.

Buforn, E., Udias, A., Mezcua, J. and Madariaga, R., 1991b, A deep earthquake under south Spain. Bull. Seismol. Soc. Am., 81: 1403–1407.

Calcagnile, G. and Panza, G.F., 1981. The main characteristics of the lithosphere–asthenosphere system in Italy and surrounding regions. Pure Appl. Geophys., 119: 865–879.

Calcagnile, G., D'Ingeo, F., Farrugia, P. and Panza, G.F., 1982. The lithosphere in the central–eastern Mediterranean area. Pure Appl. Geophys., 120: 389–406.

Chung, W.-Y. and Kanamori, H., 1976. Source process and tectonic implications of the Spanish deep-focus earthquake of March 29, 1954. Phys. Earth. Planet. Inter., 13: 85–96.

De Jonge, M.R., Wortel, M.J.R. and Spakman, W., 1993. Regional scale tectonic evolution and the seismic velocity structure of the lithosphere and upper mantle: the Mediterranean region. J. Geophys. Res., submitted.

Dercourt, J., Zonenshain, L.P. et al., 1986. Geological evolution of the Tethys belt from the Atlantic to the Pamirs since the Lias. Tectonophysics, 123: 241–315.

Dewey, J.F., Helman, M.L., Turco, E., Hutton, D.H.W. and Knott, S.D., 1989. Kinematics of the Western Mediterranean. Geol. Soc. Spec. Publ., 45: 265–283.

Dost, B., 1987. The NARS array; a seismic experiment in Western Europe, Ph.D. Thesis, University of Utrecht, Utrecht, 117 pp.

Dziewonski, A.M. and Gilbert, F., 1976. The effect of small, aspherical perturbations on travel times and a re-examination of the corrections for ellipticity. Geophys. J.R. Astron. Soc., 4: 7–17.

Elsasser, W.M., 1971. Seafloor spreading as thermal convection. J. Geophys. Res., 76: 1101–1112.

Engdahl, E.R. and van der Hilst, R.D. 1991. Reprocessing of ISC phase data for northwest Pacific earthquakes. EOS Trans. Am. Geophys. Union, 72: 191.

Granet, M. and Trampert, J., 1989. Large-scale P-velocity structures in the Euro-Mediterranean area. Geophys. J. Int., 99: 583–594.

Humphreys, E. and Clayton, R.W., 1988. Adaptation of back-projection tomography to seismic travel time problems. J. Geophys. Res., 93: 1073–1085.

Inoue, H., Fukao, Y., Tanabe, K. and Ogata, Y., 1990. Whole mantle P-wave travel time tomography, Phys. Earth Planet Inter., 59: 294–328.

Jeffreys, H., 1970. The Earth Cambridge University Press, Cambridge, 525 pp.

Kennett, B.L.N. and Engdahl, E.R., 1991. Travel times for global earthquake location and phase identification, Geophys. J. Int., 105: 429–466.

Kissling, E., 1988. Geotomography with local earthquake data. Rev. Geophys., 26(4): 659–698.

Lee, W.H.K. and Stewart, S.W., 1981. Principles and Applications of Microearthquake Networks, Academic Press, New York, 293 pp.

Leveque, J.-J., Rivera, L. and Wittlinger, G., 1993. On the use of the checker-board test to assess the resolution of tomographic inversions. Geophys. J. Int., in press.

Mueller, S. and Panza, G.F., 1984. The lithosphere–asthenosphere system in Europe. In: D.A. Galson and S. Mueller (Editors), First EGT Workshop—the Northern Segment. European Science Foundation, Strasbourg, pp. 93–112.

Nolet, G., 1985. Solving or resolving inadequate and noisy tomographic systems. J. Comput. Phys., 61: 463–482.

Nolet, G., 1990. Partitioned waveform inversion and two-dimensional structure under the Network of Autonomously Recording Seismographs. J. Geophys. Res., 95: 8499–8512.

Nolet, G. and Vlaar, N.J., 1982. The NARS project: probing the Earth with a large seismic antenna. Terra Cognita, 2: 17–25.

Paige, C.C. and Saunders, M.A., 1982. LSQR: an algorithm for sparse linear equations and sparse least squares. ACM Trans. Math. Soft., 8: 43–71.

Panza, G.F., 1984. The deep structure of the Mediterranean–Alpine region and large shallow earthquakes. Mem. Soc. Geol. Ital., 29: 5–13.

Panza, G.F. and Mueller, S., 1979, The plate boundary between Eurasia and Africa in the Alpine area. Mem. Sci. Geol. (Padova), 33: 43–50.

Panza, G.F. and Suhadolc, P., 1990. Properties of the lithosphere in collisional belts in the Mediterranean—a review. Tectonophysics., 182: 39–46.

Panza, G.F., Mueller, S. and Calcagnile, G., 1980. The gross features of the lithosphere–asthenosphere system in Europe from seismic surface waves and body waves. Pure Appl. Geophys., 118: 1209–1213.

Paulssen, H., 1987. Lateral heterogeneity of Europe's upper mantle as inferred from modeling of broad-band body waves. Geophys. J.R. Astron. Soc., 91: 171–199.

Platt, J.P. and Vissers, R.L.M., 1989. Extensional collapse of thickened continental lithosphere: a working hypothesis for the Alboran Sea and Gibraltar arc. Geology, 17: 540–543.

Remkes, M. and Spakman, W., 1993. Joint inversion of regional geoid and seismic delay time data for the European mantle structure. Terra Abstr., 5: 124.

Selvaggi, G. and Amato, A., 1992. Subcrustal earthquakes in the northern Apennines (Italy): evidence for still active subduction? Geophys. Res. Lett., 19(21): 2127–2130.

Snieder, R., 1988. Large scale waveform inversions of surface waves for lateral heterogeneity—II: Application to surface waves in Europe and the Mediterranean. J. Geophys. Res., 93: 12067–12080.

Spakman, W., 1986. Subduction beneath Eurasia in connection with the Mesozoic Tethys. Geol. Mijnbouw, 65: 145–153.

Spakman, W., 1988. Upper mantle delay time tomography. Ph.D. Thesis, University of Utrecht, Utrecht, 200 pp.

Spakman, W., 1990. Images of the upper mantle of central Europe and the Mediterranean. Terra Nova, 2: 542–553.

Spakman, W., 1991. Delay-time tomography of the upper mantle below Europe, the Mediterranean, and Asia Minor. Geophys. J. Int., 107: 309–332.

Spakman, W., 1993. Iterative strategies for nonlinear traveltime tomography using global earthquake data. In: H.M. Iyer and K. Hirahara (Editors), Seismic Tomography: Theory and Practice. Chapman and Hall, London, pp. 190–226.

Spakman, W. and Nolet, G., 1988. Imaging algorithms, accuracy and resolution in delay time tomography, In: N.J. Vlaar, N. Nolet, M.J.R. Wortel and S.A.P.L. Cloetingh (Editors), Mathematical Geophysics: A Survey of Recent Developments in Seismology and Geodynamics. Reidel, Dordrecht, pp. 155–188.

Spakman, W., Wortel, M.J.R. and Vlaar, N.J., 1988. The Hellenic subduction zone: a tomographic image and its geodynamic implications. Geophys. Res. Lett., 15: 60–63.

Spakman, W., Stein, S. van der Hilst, R.D. and Wortel, M.J.R., 1989. Resolution experiments for NW Pacific Subduction Zone Tomography. Geophys. Res. Lett., 16: 1097–1100.

Trampert, J. and Leveque, J.-J., 1990. Simultaneous Iterative Reconstruction Technique: physical interpretation based on the generalized least squares solution. J. Geophys. Res., 95: 12553–12559.

VanDecar, J.C., 1991. Upper-mantle structure of the Cascadia subduction zone from non-linear teleseismic travel-time inversion. Ph.D. Thesis, University of Washington, 165 pp.

Van der Hilst, R.D., 1990. Tomography with P, PP and pP delay-time data and the three-dimensional mantle structure below the Caribbean region. Ph.D. Thesis, University of Utrecht, Utrecht, 250 pp.

Van der Hilst, R.D. and Engdahl, E.R., 1992. Step-wise relocation of ISC earthquake hypocenters for linearized tomographic imaging of slab structure. Phys. Earth Planet. Inter., 75: 39–53.

Van der Hilst, R.D. and Spakman, W., 1989. Importance of the reference model in linearized tomographic inversions: images of subduction below the Caribbean plate. Geophys. Res. Lett., 16: 1093–1097.

Van der Hilst, R.D., Engdahl, E.R., Spakman, W. and Nolet, G., 1991. Tomographic imaging of subducted lithosphere below northwest Pacific island arcs. Nature, 353: 37–43.

Van der Hilst, R.D., Engdahl, E.R. and Spakman W., 1993. Tomographic inversion of P and pP data for aspherical mantle structure below the northwest Pacific region. Geophys. J. Int., in press.

Van der Sluis, A. and van der Vorst, H.A., 1987. Numerical solution of large, sparse linear systems arising from tomographic problems, In: G. Nolet (Editor), Seismic Tomography. Reidel, Dordrecht, pp. 53–87.

Wortel, M.J.R. and Spakman, W., 1990. Structure and dynamics of subducted lithosphere, arc migration and the evolution of the Mediterranean region. EOS Trans. Am. Geophys. Union, 71: 1633.

Wortel, M.J.R. and Spakman, W., 1992. Structure and dynamics of subducted lithosphere in the Mediterranean region. Proc. K. Ned. Akad. Wet., 95: 325–347.

Wortel, M.J.R. and Spakman, W., 1993. The dynamic evolution of the Apenninic–Calabrian, Hellenic and Carpathian arcs: a unifying approach. Terra Abstr., 5: 97.

Wortel, M.J.R., Goes, S.D.B. and Spakman, W., 1990. Structure and seismicity of the Aegean subduction zone. Terra Nova, 2: 554–562.

Zielhuis, A., 1992. S-Wave velocity below Europe from delay-time and waveform inversions. Ph.D. Thesis, University of Utrecht, Utrecht, 148 pp.

Zielhuis, A., Spakman, W. and Nolet, G., 1989. A reference model for tomographic imaging of the upper mantle shear velocity structure beneath Europe. In: R. Cassinis, G.F. Panza and G. Nolet (Editors), Digital Seismology and Modeling of the Lithosphere. Plenum, London, pp. 333–340.